This electronic thesis or dissertation has been downloaded from the King's Research Portal at https://kclpure.kcl.ac.uk/portal/

Hybrid plasmonic nanorod metamaterial structures and their applications

Jiang, Yunlu

Awarding institution:
King's College London

The copyright of this thesis rests with the author and no quotation from it or information derived from it may be published without proper acknowledgement.

END USER LICENCE AGREEMENT

Unless another licence is stated on the immediately following page this work is licensed under a Creative Commons Attribution-NonCommercial-NoDerivatives 4.0 International licence. https://creativecommons.org/licenses/by-nc-nd/4.0/

You are free to copy, distribute and transmit the work

Under the following conditions:

- Attribution: You must attribute the work in the manner specified by the author (but not in any way that suggests that they endorse you or your use of the work).
- Non Commercial: You may not use this work for commercial purposes.
- No Derivative Works - You may not alter, transform, or build upon this work.

Any of these conditions can be waived if you receive permission from the author. Your fair dealings and other rights are in no way affected by the above.

Take down policy

If you believe that this document breaches copyright please contact librarypure@kcl.ac.uk providing details, and we will remove access to the work immediately and investigate your claim.

Download date: 26. Dec. 2024

Hybrid plasmonic nanorod metamaterial structures and their applications

Yunlu Jiang

Supervisor: Prof. Anatoly Zayats

Department of Physics
King's College London

This dissertation is submitted for the fulfilment of
Doctor of Philosophy

King's College London May 2023

Declaration

I confirm that the work presented in this thesis is my own. Where information has been derived from other sources, I confirm that this has been indicated in the thesis.

Yunlu Jiang
May 2023

Acknowledgements

I sincerely thank my supervisor, Prof. Anatoly Zayats, for allowing me to work with his group. Thank you for your continuous guidance and support throughout my PhD. I am also thankful to Prof. Pan Wang and Dr. Alexey Krasavin for their advice during the Monday Discussions and their assistance with many experiments and simulations. Many thanks go to all my colleagues in the group, from whom I've learned much at work and in life. I would also like to thank the technical and administrative staff at King's College London, particularly Bill, Jenny, and Meghan. None of the work would have been done without your support.

My sincere appreciation goes to my family and friends in China. Unfortunately, the pandemic has made it so that I couldn't see them for the last 3.5 years, making me feel even more grateful that I can write the acknowledgement now from home in China.

Undoubtedly, my PhD has been a special trip I will never forget easily. But there are some hidden blessings I would especially love to appreciate to remind myself of the trace of existence whenever I look back. A big thanks to the places where I've spent countless unforgettable days: The Offices, The Labs, The Music and Seminar Rooms, The Parks, The Terraces, The Benches, The Cafes, etc. A big thanks to all the beautiful moments that encouraged and will keep encouraging me to carry on: Sunrise, Sunset, Raindrops, Rainbows, Snowy Mornings and Full-moon Nights, etc. Lastly, I am incredibly thankful to my friends for their unlimited support and sometimes lovely distractions, from which I see the truth of life.

See you in the purple rain.

Abstract

Plasmonic metamaterials typically consist of plasmonic nanostructures that are arranged in arrays at a size smaller than the wavelength of interest, and they are known for their unique optical properties that can be precisely controlled with the accurate nanostructure design at a sub-wavelength scale. By exploiting their advantages in localizing and enhancing the electromagnetic field, plasmonic metamaterials have been used in various applications such as optical sensing, plasmon-enhanced spectroscopy and plasmon-assisted chemistry. Recently, hybrid plasmonic nanostructures that combine the plasmonic fields with functional materials have been developed to achieve enhanced optical properties and thus expand the range of possible applications ranging from photo-catalysis and biomedical sensors to optical modulation. In this context, we aim to explore hybrid plasmonic-molecular nanostructures to achieve passive and active functionalities of metamaterials. In this thesis, a hybrid plasmonic nanostructure has been realized by self-assembling a nanoscale layer of poly-L-histidine on gold nanorods forming the metamaterial.

On the one hand, the hybrid nanostructure is used to investigate the effect of environmental humidity on the optical response of nanorods metamaterial. Due to the high refractive index sensitivity, a significant change in the transmission is observed with $\Delta T/T$ reaching values of more than 5% when the relative humidity is changed from 11% to 75%. The experimental and simulated results demonstrate that the mechanism behind the phenomenon is associated with the roughness-assisted nanoscale condensation of water on the nanorod surface. Such results further reveal the importance of protecting plasmonic nanostructures from relative humidity variations in many practical applications that work in the ambient environment and also gas sensing applications such as hydrogen and oxygen. The hybrid structure can be used for the development of high-sensitivity relative humidity and dew condensation sensors.

On the other hand, light-emitting plasmonic tunnelling junctions have been successfully built on this hybrid nanostructure where the gold nanorod metamaterial is capped with a monolayer of poly-L-histidine working as the tunnel barrier. The compact electrical excitation of surface plasmons and generation of light emission by inelastically tunnelled electrons has been demonstrated, exhibiting a broadband tunability of the emitted light controlled by the metamaterial and the junction geometry. Besides, the voltage bias-dependent emission performance has been discussed, and typical tunnelling electrical properties have been analysed using current-voltage curves and current mapping. Additionally, by defining the tunnelling junction area, a type of microscale plasmonic tunnelling junction that allows a fast modulation of the tunnelling-excited light emission has been further achieved, which is attractive for the building of ultrafast electrically-driven light sources. Overall, these results demonstrate the advantages of such hybrid plasmonic nanostructures, highlighting their potential for developing optical humidity sensors and nanoscale light sources.

Table of contents

List of figures

Chapter 1

Introduction

1.1 Backgrounds

Photonics and electronics technologies stand at the brink where we look at merging them in computer chips as optical interconnects [1] or active nanophotonic circuits [2]. The resulting increase in computational efficiency and speed will change the world. Another critical area is photovoltaic devices, where there is a need for highly efficient ways of absorbing solar power to minimize the volume of active material required for the process. This will help reduce costs and introduce alternative materials that have been otherwise ignored for their lower efficiency [3].

However, there is a spatial limit to which light can be typically constrained using standard optical elements (lenses, mirrors, etc.). This limit arises from the diffraction of light by any standard optical aperture and is approximately equal to half the wavelength of the light wave. The good news is that we can surpass this limit and confine light into much smaller dimensions by manipulating its interaction with matter, particularly at a metal-dielectric interface. This is because, at a metal-dielectric interface or metallic nanostructures, light is coupled to coherent plasma oscillations, creating evanescent electromagnetic waves in the form of surface plasmon polaritons.

Surface plasmons are collective oscillations of free charge carriers (conduction elections in the case of metal) which, at specific frequencies, can resonate with the incident electromagnetic field to create localised sub-wavelength distributions of optical energy in subwavelength range structures. Depending on the spatial geometry of the nanostructure, this effect can be manifested in different forms as surface plasmon polaritons (SPPs) or as localised surface plasmons (LSPs). SPPs can be mathematically defined as eigenmodes of electromagnetic waves at an interface between a dielectric and metal, i.e., they can be obtained as solutions of Maxwell's equations [4]. They are planar surface waves, transverse magnetic polarised, travelling along the interface between a dielectric and a metal.

Surface plasmons are propagating waves only if one of the dimensions of the structure is close to or longer than the wavelength. For the case where all the dimensions are much smaller than the wavelength, like in a typical nanoparticle, surface plasmons no longer propagate but collectively oscillate throughout the nanostructure surface. They are then termed localised surface plasmons. The enhanced absorption and scattering of optical energy are observed due to the localised surface plasmon resonance of the nanoparticle. This effect has many uses in photothermal therapy, heat-assisted magnetic recording, etc.

Surface plasmons are well known to be highly sensitive to the refractive index change of adjacent dielectric medium within the penetration depth of their near field. This remarkable property has been exploited in label-free plasmonic sensors to detect and investigate target chemicals. Mainly based on SPPs, existing surface plasmonic resonance biosensors have shown their advantages in sensing with an extremely low detection limit to $>10^5$ refractive index unit (RIU). However, its limitation, such as the relatively low sensitivity of small analytes and difficulties in meeting more modern requirements of biotechnology, is hindering its further development in the commercial market. In contrast, LSPs-based sensors seem much more promising in compatibility with modern biotechnology development such as nanoscale design, manipulation, and selectivity of (bio)chemicals. Besides, LSPs are considered excellent sensing platforms because of their high tunability on the spectrum and substantial enhancement of the local electric field. Despite all these advantages, compared with SPPs, LSPs still suffer from limitations in the relatively low sensing response to refractive index change and small probe depth. All these problems have presented an unavoidable challenge to the current plasmonic sensors, and to face the challenge, we would like to search for solutions from new types of plasmonic metamaterials which can combine the benefits of both SPPs and LSPs, thus widening the application of plasmonic sensors. An important example is gold nanorod arrays, forming a metamaterial. The gold nanorod metamaterials have been developed to exploit nonlinear optical properties and control spontaneous emission. To further use their potential for practical applications, the hybrid plasmonic nanorod metamaterial structures and their properties must be studied, which may provide additional functionalities to those achievable with bare nanorods.

1.2 Motivation

In this work, gold nanorod metamaterials are combined with polymer poly-L-Histidine, and this hybrid nanostructure is applied for two potential applications. As we all know, the optical properties of plasmonic nanorod metamaterials are very sensitive to any environmental change, including gas and relative humidity. Measurements conducted in the ambient environment and gas sensing applications like H_2 and O_2 may also be affected by relative humidity. Considering this, studying the optical change of plasmonic metamaterials caused by the environmental relative humidity is crucial. In this work, freestanding gold nanorod arrays are used as samples. Their relative transmission changes in various relative humidity are observed, which might be associated with the nanorods' surface roughness and modification (e.g., polymer coating). Corresponding numerical simulations are also used to understand humidity-induced optical change.

On the other hand, the PLH-gold nanorod hybrid nanostructures are made into plasmonic tunnelling junctions for light emission. Specifically, the working principle is that inelastic tunnelling electrons can excite surface plasmon of nanorod metamaterials, which would then radiate as photons and generate light emission. Since the optical spectrum of metamaterials is highly dependent on the structural parameters of metamaterials, we can easily get a tuneable nanoscale light source by adjusting the geometry of nanorods metamaterials. Furthermore, this helps realise device miniaturisation because the surface plasmon polaritons could be excited by inelastic tunnelling electrons, thus eliminating the need for bulky light sources. Besides, due to the ultrafast electron tunnelling ($< 10\ fs$), plasmonic tunnelling junction provides an exciting possibility to achieve ultrafast response time. Here we aim to achieve a fast modulation speed of the optical switch by reducing the RC time delay with a defined tunnelling junction area.

1.3 Outline

Chapter 1 addresses the aim and objectives of this thesis. After briefly introducing light-metal interactions, in Chapter 2, we first overview the theoretical background of surface plasmon polaritons and plasmonic metamaterials. The design, optical properties, fabrication techniques, and relevant applications of plasmonic metamaterials are also described. Then, the fabrication techniques and the structural and optical characterisation specific to plasmonic nanorod metamaterials are discussed in detail in Chapter 3. Chapter 4 highlights a humidity-induced direct modification of the optical response of plasmonic metamaterials, which is vital for plasmonic devices operating in the ambient environment, particularly for gas sensing. Nanorods-based plasmonic tunnel junctions and their potential for nanoscale light sources are discussed in Chapter 5. Their structural characterisation, electric and optical properties investigation, and emission properties are presented. Finally, conclusions and future work are outlined at the end of this thesis in Chapter 6.

Chapter 2

Fundamentals

This chapter first introduces fundamental optical parameters to understand the interaction between light and materials at optical frequencies. And basic concepts such as surface plasmon polaritons and localised surface plasmon resonances are then presented to lay a solid theoretical background for plasmonic metamaterials. Furthermore, hyperbolic metamaterials as a subclass of plasmonic metamaterials are highlighted, and the effective medium theory is discussed to interpret the optical properties of metamaterials. In addition, some typical nano-fabrication techniques of plasmonic metamaterials are introduced. Lastly, a wide range of applications of plasmonic metamaterials is covered, including optical sensing, surface-enhanced spectroscopy, photo-chemistry/catalysis, etc.

2.1 Interaction of Light with Metals

Since the primordial explosion, which started the expansion of the universe and released the photons to freely travel forth, the one physical property that has stayed constant is light. Using dielectric lenses and metallic mirrors, we have managed to exploit its interaction with matter to observe this universe, right from the division of a cell to the birth of a star. In the modern world, we strive to manipulate light in various ways, not just for imaging. It is crucial to understand the light-matter interaction at optical frequencies to design materials that can precisely govern light absorption, reflection and refraction at the scale of (sub)wavelength and realise a wide range of practical applications.

Maxwell's equations describe the interaction of electromagnetic radiation with matter. In the case of vacuum, deriving the plane wave equation from Maxwell's equations, one possible plane wave solution for the electric field is

$$\mathbf{E}(r,t) = \mathbf{E}_0 e^{i(\mathbf{k}\cdot\mathbf{r}-\omega t)} \tag{2.1}$$

where $\mathbf{r}$ is the propagation direction, $\mathbf{k}$ is the wavevector, and $\omega = 2\pi f$ is the angular frequency. In vacuum, for the wavenumber k (the modulus of the wavevector $\mathbf{k}$), its relationship with light can be expressed as $k_0 = \omega/c_0$ and $k_0 = 2\pi/\lambda_0$, where c_0 is the speed of light in vacuum and λ_0 is the wavelength of light in vacuum.

Different from travelling in the free space, when propagating in materials, an electromagnetic wave is often described in three different forms: transmission (T), reflection (R) and absorption (A). And the overall energy balance follows the equation $1 = T + R + A$. And the ability of materials to affect electromagnetic wave propagation is usually characterised by the optical properties of materials, which are mainly described in terms of their complex refractive index and dielectric permittivity.

The complex refractive index $n = n' + in''$, where the real part n' is responsible for the change of the light speed in the material, while the imaginary part n'' is more related to the light absorption in the material and also called as extinction coefficient. For equation (2.1), if we consider its time-independent form, the plane wave solution would be expressed as follows:

$$\mathbf{E}(r) = \mathbf{E}_0 e^{i\mathbf{k}\cdot\mathbf{r}} \tag{2.2}$$

Here the complex wavenumber $k = nk_0 = k' + ik''$, and light wavelength in the material hence become $\lambda = \lambda_0/n$ since $\lambda_0 = 2\pi/k_0$.

The dielectric constant $\varepsilon = \varepsilon' + i\varepsilon''$ is another term often used to describe the optical properties of materials. Here, the relation between the complex refraction index and the dielectric constant can be expressed as follows: $\varepsilon' = n'^2 - n''^2$ and $\varepsilon'' = 2n'n''$.

According to the Beer-Lambert law, the intensity of an electromagnetic wave decays exponentially from the surface after travelling a certain distance in a lossy material, as

$$I(r) = I_0 e^{-\alpha r} \tag{2.3}$$

where the intensity/power of a wave is modulus squared of the electromagnetic field $I = |E|^2$, and α denotes the absorption coefficient. When the electromagnetic field decays to $1/e$ of its original value, this particular travelling distance is termed the skin depth δ, and its relationship between the complex refractive index and wavenumber follows these equations: $\delta = 1/nk'' = 1/n''k_0$. Besides, from equation (2.2) and (2.3), we can also obtain the relation between the skin depth and the absorption $\delta = 2/\alpha$ [5].

Based on the energy band theory, materials, according to their different electronic band structures, can be roughly divided into three classes: conductors, semiconductors and insulators. Fundamentally, metals, as a kind of conductors, are characterised by the overlapping of the valence band (VB) and the conduction band (CB), meaning that electrons can freely transport at room temperature under an externally applied electric field. In other words, metals have a high density of free electrons, around $10^{28} - 10^{29}$ e/m^3 [6]. Semiconductors, however, are characterised by having the VB and the CB separated by a small forbidden energy band gap, and the movement of electrons from the VB to the CB is achievable when the external energy is higher than the forbidden energy gap. If the forbidden energy gap is so large that electrons can't move to the CB, it is called an insulator.

To understand their optical properties, metals are often considered as a collection of free electron gas moving around relatively immobile positively charged ions. And the optical response of metals under an external electromagnetic field can be well described by the Drude model, where free electrons go through damped oscillations due to electron-ion collisions. Because of this, the Drude model is also called the free electron model. Applying Newton's law to the motion of free electrons and writing in the differential form, we obtain the following motion equation:

$$m_e \frac{\partial^2 \mathbf{r}}{\partial t^2} + m_e \gamma \frac{\partial \mathbf{r}}{\partial t} = -e\mathbf{E} \tag{2.4}$$

Where m_e is the effective mass of free electrons, $-e$ is the charge of free electrons, $\mathbf{r}$ is the electron displacement, $\mathbf{E}$ is the external driven electric field, and $\gamma = 1/\tau$ is average collision frequency, where τ is the average collision time. Here, τ is related to the average collision distance l (mean free path) and the average thermal velocity of classical particles v_{th} by $l = \tau v_{th}$.

An approach to solve the above equation is assuming the external driven electric field is the harmonic time dependence $\mathbf{E}(t) = \mathbf{E}_0 e^{-i\omega t}$, and therefore the electron displacement becomes $\mathbf{r}(t) = \mathbf{r}_0 e^{-i\omega t}$. After a simple algebra operation for equation (2.4), we can get:

$$\mathbf{r} = \frac{e}{m_e(\omega^2 + i\gamma\omega)} \mathbf{E} \tag{2.5}$$

Since each free electron can produce a dipole moment $\mathbf{p} = -e\mathbf{r}$, for metals with electron density N (the averaged number of electrons per unit volume), its polarisation density vector (the averaged density of dipole moment per unit volume) can be described as

$$\mathbf{P} = N\mathbf{p} = -Ne\mathbf{r} \tag{2.6}$$

Considering its relationship with the driven electric field and electric displacement field:

$$\mathbf{D} = \varepsilon_0\varepsilon\mathbf{E} = \varepsilon_0\mathbf{E} + \mathbf{P} \tag{2.7}$$

where ε_0 is the vacuum permittivity, and ε is the relative permittivity of metals. Combining the equations (2.5), (2.6) and (2.7), we finally arrive at a complex, frequency-dependent dielectric constant (permittivity) for metals:

$$\begin{aligned}\varepsilon(\omega) &= \varepsilon'(\omega) + i\varepsilon''(\omega) \\ &= (1 - \frac{\omega_p^2}{\gamma^2 + \omega^2}) + i(\frac{\omega_p^2}{\gamma^2 + \omega^2} \cdot \frac{\gamma}{\omega})\end{aligned} \tag{2.8}$$

with

$$\omega_p^2 = \frac{Ne^2}{\varepsilon_0 m_e} \tag{2.9}$$

ω_p is known as the bulk plasma frequency, and it is an important parameter in showing the metallic behaviours of metals. If the collision frequency γ is far smaller than the bulk plasma frequency ω_p, then the equation (2.8) can be simplified as

$$\varepsilon(\omega) = (1 - \frac{\omega_p^2}{\omega^2}) + i\frac{\omega_p^2\gamma}{\omega^3} \tag{2.10}$$

And thus the real part of the metal permittivity $\varepsilon'(\omega)$ is expressed as follows:

$$\varepsilon'(\omega) = 1 - \frac{\omega_p^2}{\omega^2} \tag{2.11}$$

Its value is negative in the frequency range below the bulk plasma frequency $\gamma < \omega < \omega_p$. The physical meaning is that the free electrons inside of metal would oscillate in phase with the external electric field and then reradiate the same field back. This is because of the high reflectivity and small skin depths of metals. And this frequency regime is called the relaxation regime. The reflection of metals decreases significantly at the bulk plasma frequency, and the $\varepsilon'(\omega)$ becomes positive for ω exceeding the plasma frequency $\omega > \omega_p$. At this spectral region, the electrons lag behind the applied electric field, penetrating the materials, making the metal look transparent [7].

Based on a lot of assumptions, e.g., using the Kinetic theory of gases, focusing only on the collisions and ignoring electron-electron and electron-ion interaction, the Drude model correctly predicts and explains the optical proprieties for most metals at low frequencies. However, it doesn't apply successfully to the high-frequency regime where the electrons' inter-band transitions dominate. Therefore, for noble metals, such as gold and silver, which have high electron density in the conduction band and their plasma frequency in the ultraviolet range, it is necessary to consider the inter-band transition effect when describing their optical properties at a lower frequency, e.g., in the visible and infrared spectrum. Hendrik Antoon Lorentz later developed the Drude model, which included an additional restoring force term into the electron motion equation. Afterwards, Arnold Sommerfeld combined the resulting Drude-Lorentz model with Fermi-Dirac statistics, leading to the Drude-Sommerfeld model. More details related are outside the scope of the current thesis and will not be discussed further.

2.2 Surface Plasmon Polaritons

Plasmons are regarded as collective oscillations of the free electrons in the media. Suppose the plasmons are confined to the surfaces between a metal and a dielectric medium and strongly interact with an external electromagnetic field. In that case, it is called surface plasmon polaritons or surface plasmon resonance. Mathematically, SPPs can be defined as eigenmodes of an interface between a dielectric and metal, i.e., the theoretical model for SPPs can be obtained as solutions of Maxwell's equations in the absence of an incident electromagnetic field [4]. In practice, we assume all materials are linear, isotropic and homogeneous for the sake of simplicity. The SPPs phenomenon then can be viewed as a simplified case where a plane wave propagates along the interface between two semi-infinite half-space materials with different dielectric constants. By satisfying boundary conditions of the continuity of tangential components of electromagnetic wave, both electric field **E** and magnetic field **H**, and also considering the normal component of the electric displacement field **D** across the metal-dielectric interface, we can describe the fundamental physical properties of SPPs.

To make things easier, we assume the geometry and the electromagnetic fields are invariant along one direction (i.e., y-direction). By doing so, we turn the three-dimensional plane wave equation problem (x-y-z coordinate system) into a two-dimensional problem (x-z plane) which is easier to solve. In this case, the corresponding two-dimensional solutions can be written as a superposition of two independent self-consistent terms: transverse magnetic modes (TM modes, also called p-polarised modes) and transverse electric modes (TE modes, also called s-polarised modes). For TM-polarised mode, the magnetic field $\mathbf{H}$ is transverse to the propagation direction and parallel to the material surface ($\mathbf{H}_y$), while the electric field $\mathbf{E}$ has components both transverse and longitudinal to the propagation direction ($\mathbf{E}_x$ and $\mathbf{E}_z$). TE-polarised mode has $\mathbf{H}_x$, $\mathbf{H}_z$, and $\mathbf{E}_y$. And, thus the total electric field can be expressed in the form as: $\mathbf{E}(\mathbf{r}) = \mathbf{E}^{TM}(\mathbf{r}) + \mathbf{E}^{TE}(\mathbf{r})$.

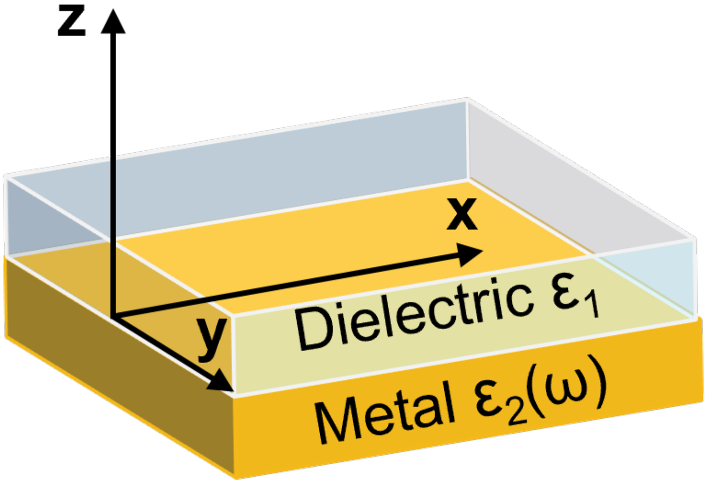

Fig. 2.1 The schematic of the metal-dielectric interface.

Figure 2.1 shows a classic schematic of a surface wave travelling at the planar interface ($z = 0$) between two different materials. The material 1 is at the region $z > 0$ with the dielectric constant ε_1, while the material 2 is at the region $z < 0$ with the dielectric constant ε_2. Assuming there are no external driving charges or current densities, two sets of plane solutions can be derived from the Maxwell equations for this system in TM modes and TE modes, respectively. However, here we only discuss the case of TM-polarised modes for the excitation of SPPs, because the SPPs excited via TE modes don't exist at optical frequencies unless the permeability of materials is negative, which is not the case for metals.

By solving the wave equation solution for TM-polarised waves, we obtain the following equations:

$$\frac{k_{z1}}{k_{z2}} = -\frac{\varepsilon_1}{\varepsilon_2} \tag{2.12}$$

$$k_{z1}^2 + k_x^2 = \varepsilon_1 k_0^2 \tag{2.13}$$

$$k_{z2}^2 + k_x^2 = \varepsilon_2 k_0^2 \tag{2.14}$$

where k_x is the component of the wavevector along the x-direction, k_{z1} and k_{z2} are the normal components of the interface for each material, and k_0 is the wavevector at vacuum.

Replacing the k_{z1} and k_{z2} in the equation (2.12) with the equations (2.13) and (2.14), the dispersion relation of SPPs at the metal-dielectric interface can be expressed as the following:

$$k_x = k_0\sqrt{\frac{\varepsilon_1\varepsilon_2}{\varepsilon_1+\varepsilon_2}} = \sqrt{\varepsilon_1}k_0\sqrt{\frac{\varepsilon_2}{\varepsilon_1+\varepsilon_2}} \tag{2.15}$$

And the expression for the normal wavevector components can also be obtained:

$$k_{z1} = k_0\sqrt{\frac{\varepsilon_1^2}{\varepsilon_1+\varepsilon_2}} \tag{2.16}$$

$$k_{z2} = k_0\sqrt{\frac{\varepsilon_2^2}{\varepsilon_1+\varepsilon_2}} \tag{2.17}$$

To make the SPPs propagate along the interface, k_x is required to be a real value while the normal components k_{z1} and k_{z2} both are imaginary. From the above equations (2.15)-(2.17), we know that this can only be achieved when the sum and product of dielectric constants are both negative, that is, $\varepsilon_1 + \varepsilon_2 < 0$ and $\varepsilon_1\varepsilon_2 < 0$. Assuming the dielectric constant of material 1 is real-valued, and thus, the real part of the material 2, ε_2', needs to be negative and also $|\varepsilon_2'| > \varepsilon_1$. In a word, SPPs can only exist at the interface between a metal ($\varepsilon < 0$) and a dielectric material ($\varepsilon > 0$).

As an SPPs propagates along the x-direction, energy is dissipated to the metal due to absorption. This decay can be described with an SPPs propagation length l_{spp} by which the intensity of SPPs decays by a factor of $1/e$. Since the relation between the electric field intensity and wave propagating length x is $I = |E|^2 \propto e^{-2k_x''x} \propto e^{-2n''k_0x}$, the SPPs propagation length l_{SPP} thus can be expressed as

$$l_{SPP} = \frac{1}{2k_x''} = \frac{1}{2n''k_0} \tag{2.18}$$

Equation (2.18) indicates that the decay of energy origins from the imaginary part of the permittivity of materials. As a relatively absorbing material, aluminium's propagation length is only 2 μm at 500 nm. However, for a metal with a lower imaginary permittivity at the same wavelength, such as silver, the propagation length increases to 20 μm [8]. Furthermore, it should be noted that this equation is for an ideal smooth surface. However, in practice, there are more energy losses due to the surface roughness, which makes it an unavoidable challenge in the practical application of plasmonics.

Likewise, the electric field decays exponentially perpendicular to the metal-dielectric interface (z-direction). For the dielectric medium, the decay length of the field is typically on the order of half the wavelength of the electromagnetic field involved ($\lambda_0/2n_d$), while the decay length for the metallic layer is determined by the skin depth, which can be expressed as

$$l_m = k_0 \frac{\varepsilon_m}{\sqrt{\varepsilon_d + \varepsilon_m}} \tag{2.19}$$

where l_m defines the confinement depth normal to the metal-dielectric interface, k_0 is the optical wavevector in a vacuum, and ε is the optical permittivity of the metallic layer (m).

Equation (2.19) shows how the skin depth indicates the confinement of the evanescent wave to the metal-dielectric interface. For an Ag/Air interface at 633 nm, the decay depth in the dielectric is 210 nm, while in the metal, we have confinement depth l_m as 11 nm. Thus we see that for higher values of permittivity, one can have extreme sub-wavelength confinement of optical energy.

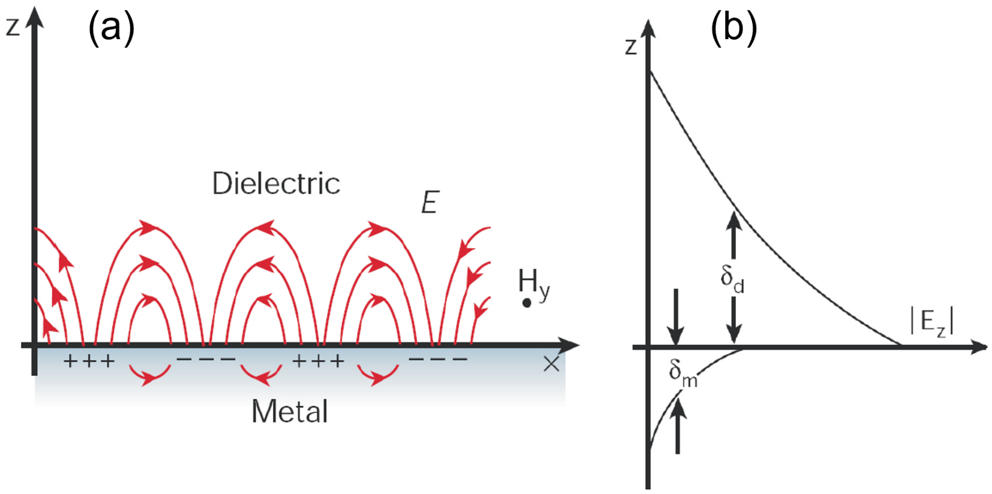

Fig. 2.2 (a) SPPs propagation at the interface between metal and dielectric. (b) The evanescent field that decays exponentially into the two half space [8].

Altogether, Figure 2.2 shows the decaying evanescent characters of the electromagnetic wave at the metal-dielectric interface both at x and z directions [8].

we can derive the SPP dispersion relation for a metal based on the mathematical results we have obtained. Take the lossless Drude metal in the air, for example. In this case, only the real part of the metal permittivity $\varepsilon'(\omega)$ is considered, and the dielectric constant of air is 1 ($\varepsilon_1 = 1$). By substituting Drude's lossless permittivity equation (2.11) into the dispersion relation equation (2.15), SPP dispersion curves for the lossless Drude metal in the air are obtained [9], as the grey curves given in Figure 2.3.

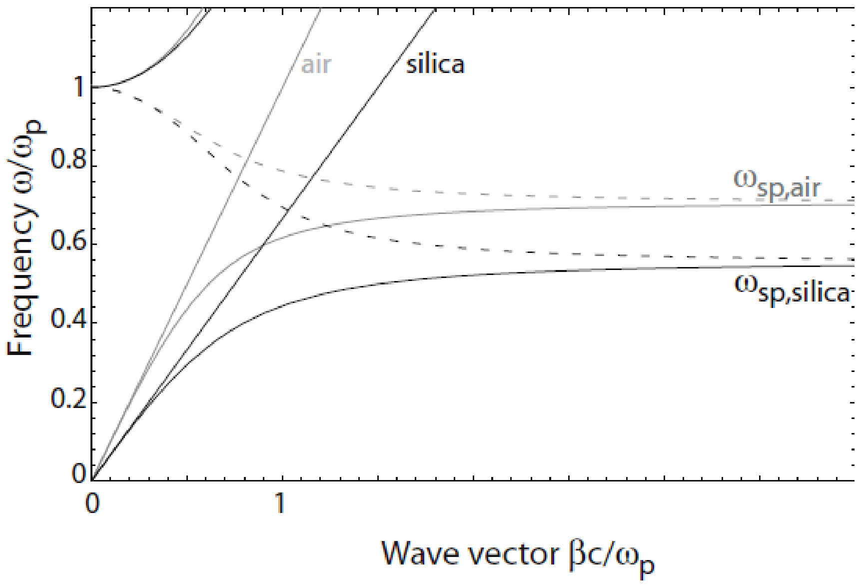

Fig. 2.3 Dispersion relation of SPPs at the interface between a lossless Drude metal and air (grey curves) and silica (black curves) [9].

The straight grey line presents the light line in the air ($k_x = \omega/c_0$). The SPPs dispersion is mainly composed of two branches according to the value of angular frequencies ($\omega > \omega_p$: high-frequency branch, and $\omega < \omega_{sp}$: low-frequency branch), between which dash curves denote a frequency gap. k_x is purely imaginary valued in this frequency gap, which means the evanescent wave decays in the x direction and hence there is no SPP propagation. In the high-frequency branch for ($\omega > \omega_p$), the normal component wavevector k_z is not purely imaginary anymore, meaning there is electron oscillation inside the metal and thus results in bulk plasmon. On the other hand, in the low-frequency branch for ($\omega < \omega_{sp}$), k_x has a valid real part component while k_z is purely imaginary, which altogether fulfils the wavevector conditions for SPPs mode to exist. It's noted that ω_{sp} is the limit of ω when $k_x \to \infty$ (that is, when $\varepsilon_2 \to -\varepsilon_1 = -1$), with the inverse derivation of the equations (2.11) and (2.15), we finally get the angular frequency for SPPs of lossless Drude metal in the air:

$$\omega_{SPP} = \frac{\omega_p}{\sqrt{1+\varepsilon_1}} = \frac{\omega_p}{\sqrt{2}} \tag{2.20}$$

It is worth noting that, in this dispersion relation, a field can be confined extremely along the z direction and no energy loss because $k_z \to \infty$ and no imaginary k_x exists when $k_x \to \infty$. However, in reality, ε_2 is a complex number as the equation (2.10) shows, which means that the imaginary part of k_x exists at all frequencies and therefore results in the energy losses.

We can also notice that the dispersion relation of SPPs for lossless Drude mode (the low-frequency branch) lies outside of the light line in the air ε_1. And this phenomenon always exists even when changing air to other different dielectrics, e.g., $\varepsilon_{silica} = 1.5$ (black lines and curves in Figure 2.3). This is due to the momentum mismatch between SPPs and free space photons (at the same frequency, the k_x of SPPs is always greater than that of free space), which means that it is impossible to excite SPPs with the incident light in the dielectrics directly.

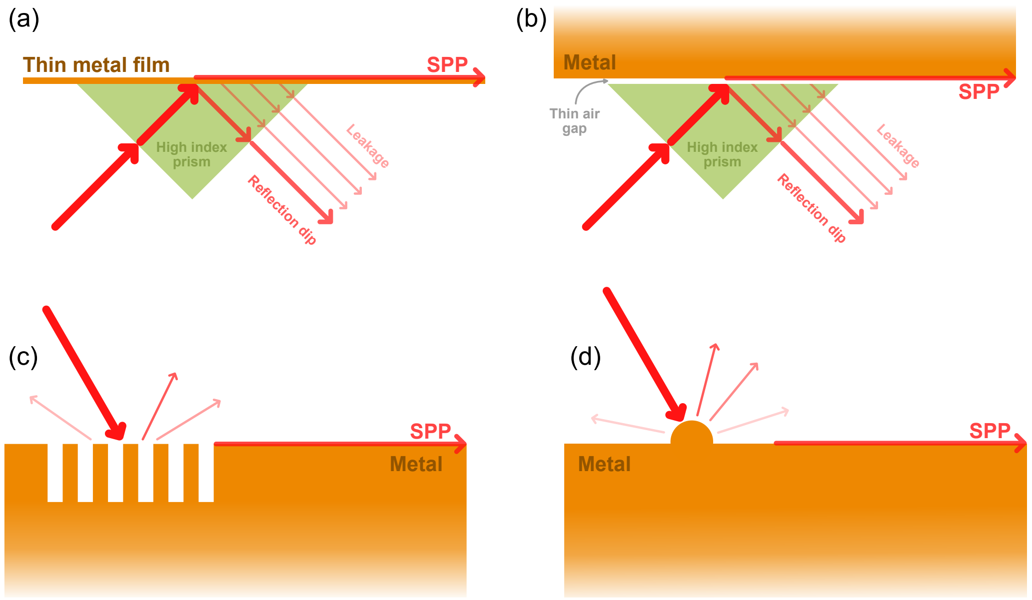

Fig. 2.4 Schematic diagrams of different SPP excitation configures. Prism coupling with (a) Kretschmann, (b) Otto configuration. Other exciting SPPs with (c) a periodic grating and (d) surface features scattering.

To overcome the momentum mismatch, many techniques have been invented after decades of effort. Figure 2.4 shows several schematic diagrams of different SPP excitation configures. Prism excitation is the simplest way to excite SPPs. The principle of such a method is to increase the wave vector of incident light by adding a high-refractive index medium, such as prism/glass. The incident field from the prism can either decay to the evanescent field between the prism-metal interface and then couple to the metal-air interface on the other side (Kretchsman configuration), or it can first decay between the prism-air interface and then couple at the metal-air interface to excite SPPs (Otto configuration). Other techniques are based on the idea of introducing new wave vectors, including grating excitation [10], surface defects excitation and near field source excitation [11], etc.

2.3 Localized Surface Plasmon Resonances

When all the structure dimensions are much smaller than the wavelength, like in a typical nanoparticle, the distinction between bulk and surface plasmon disappears, and surface plasmons no longer propagate but collectively oscillate throughout the nanostructure surface. They are then termed localized surface plasmon resonances. Most of the LSPRs resonance frequency lies in the visible-near infrared region. Because of the high spatial confinement of the particles, the excitation of LSPRs can be achieved via direct incident light without considering the momentum mismatch difficulty. The resonant frequency of the plasmon is highly sensitive to the local environment of the nanoparticle so nanoparticles can be used as highly efficient sensors. Also, the highly enhanced absorption of optical energy due to LSPRs can significantly help to harvest energy at the interface between the particle and its neighbouring dielectric medium. This property has many uses, like photovoltaics, photothermal therapy, heat-assisted magnetic recording, etc.

Most physical effects of LSPRs can be explained with a simple mode, a spherical metal nanoparticle. Assuming a metal sphere in the radius of R in an isotropic and non-absorbing dielectric medium, the dielectric constants of the medium and sphere are ε_1 and ε_2, respectively. Under a uniform time-harmonic electric field $\mathbf{E}_0$, the conduction electrons would first shift relatively away from the nuclei due to the electric field driving force and then move back towards the nuclei under a restoring force caused by Coulomb attraction. Together these shifted electrons would experience a resonant oscillation at a certain frequency (ω_{LSPRs}). Figure 2.5 shows the LSPRs on spherical particles under an external electric field. Since the size of the sphere is far smaller than the wavelength of the external field, the scattered electric field outside the sphere can be quasi-statically approximated as a dipole field, which induces

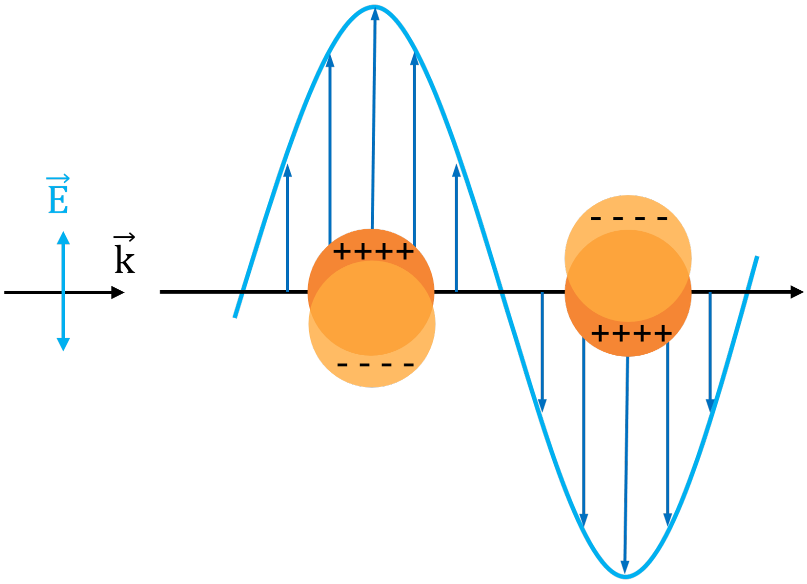

Fig. 2.5 Schematic diagram of LSPRs of metallic spheres.

a dipole moment $\mathbf{P}$. And the relation between the external field and the dipole moment is given by $\mathbf{P} = \alpha\varepsilon_1\mathbf{E}_0$. Here, α is defined as the polarizability of a spherical particle, which represents the resonance behaviour and is greatly determined by the particle's shape, size and material, and also the material of the surrounding dielectric medium. For a spherical particle, α can be mathematically expressed as follows:

$$\alpha = 4\pi R^3 \frac{\varepsilon_2 - \varepsilon_1}{\varepsilon_2 + 2\varepsilon_1} \tag{2.21}$$

We see that to satisfy the surface plasmon resonance condition, it requires $\varepsilon'(\omega) = \varepsilon_2 = -2\varepsilon_1$. Submitting this equation to a lossless Drude metal in the air (equation (2.11)), we easily obtain the associated LSPRs frequency for the metal sphere:

$$\omega_{LSPRs} = \frac{\omega_p}{\sqrt{3}} \tag{2.22}$$

Likewise, the polarizability of other shapes of metallic particles, such as ellipsoids, can be obtained based on the same theory. The only difference is that the polarizability along each direction should be treated separately as it varies with the geometric parameters of nanoparticles.

A good example of LSPRs properties is plasmonic nanoparticles, whose optical resonance is mainly determined by their size and shape. Silver nanoparticles, for example, can show different LSPRs with different geometries ranging from spheres and triangles to

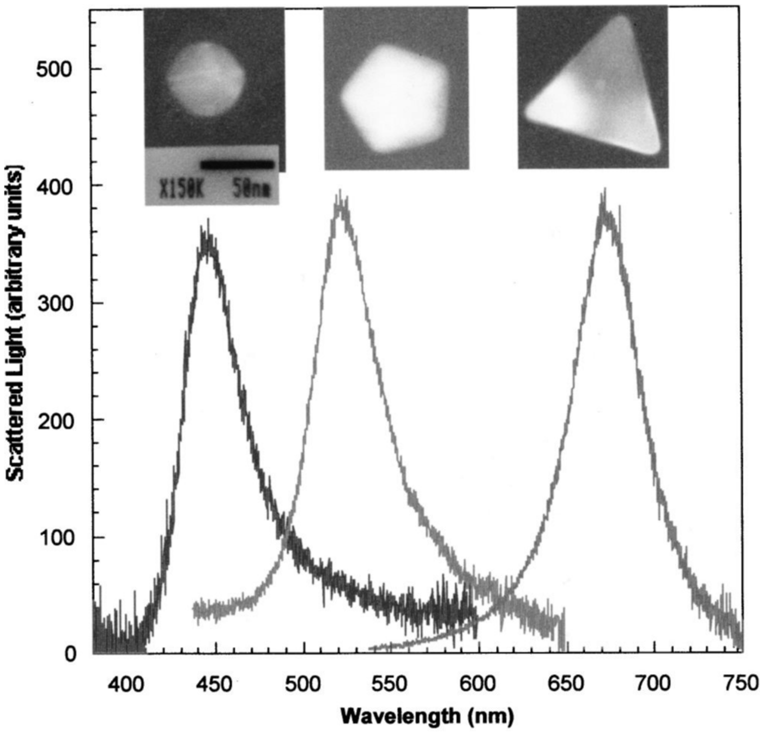

Fig. 2.6 Typical optical spectra and the corresponding TEM images of individual silver nanoparticles [12].

pentagons [12, 13], as shown in the Figure 2.6. And gold nanoparticles, as another example, also exhibit different enhancement and localization of the electromagnetic field with different geometrical designs [14]. With the development of nano-fabrication techniques, more complex geometries such as Au-SiO_2 core-shell nanoparticles have emerged to achieve precise control over the plasmonic enhancement. Au-SiO_2 nanoparticles consist of alternating shells of silica and gold layers and have optical properties which can be tuned with careful control over the shell thicknesses and the number of layers. This gives a route to define the supported plasmonic modes and therefore engineer the optical spectrum of the nanostructure. Besides, for plasmonic nanoparticles, the plasmonic interaction between them is highly sensitive to their separation and the surrounding dielectric materials, making them great use as optical sensors. Other applications based on the strong electromagnetic field enhancement and localization have also been explored, such as molecular rulers [15] and cancer imaging and photo-thermal therapy [16].

2.4 Metamaterials

2.4.1 Plasmonic Metamaterials

With the support of SPPs/LSPRs, nano-structured metallic (metallic-dielectric) objects can show desired optical characteristics that conventional materials usually don't possess. And their fundamental optical properties are not only determined by their atomic structure but also by their artificial nanostructures that much smaller than the wavelength of the electromagnetic field. These unique nanostructures are termed "metamaterials", where the "meta" derives from the Greek $\mu\varepsilon\tau\acute{\alpha}$ meaning "beyond". And the nano-sized bulking blocks that govern their matter-light interactions (resonance) are usually called "meta-atoms". Correspondingly, the two-dimensional versions of bulk metamaterials produced by a careful arrangement of meta-atoms are often called "meta surfaces".

While it was more than two decades ago that the term "metamaterial" was introduced for the first time [17] , the definition of metamaterials has varied since then due to its rapid development and increasing applications. According to the structural characteristics and their relationship with the optical properties, W.Cai and V. Shalaev first proposed that [18]: "*A metamaterial is an artificially structured material which attains its properties from the unit structure rather than the constituent materials. A metamaterial has an inhomogeneity scale much smaller than the wavelength of interest, and its electromagnetic response is expressed in terms of homogenized material parameters.*" While this classic definition has been widely recognized, the meaning of metamaterials can extend widely to include the diffraction-related (photonic crystal) effects [19] and also, it can restrict itself to a region with a certain application (e.g., a sub-wavelength control of phase) [20].

With the intentional design of metamaterials, ranging from the materials, size, and shape to the orientation and arrangement of meta-atoms, one can precisely control the optical response of the metamaterials over a broad range of wavelengths, particularly in the visible and near-infrared spectral region where is most commonly studied due to the plethora of nanoscale applications. Thanks to the advance of fabrication nanotechnology, a large number of metamaterials with different geometries have been structured at the nanoscale, such as fishnets [21], split-rings resonators [22], metallo-dielectric multi-layers [23], nanostars [24, 25], nano-flowers [26] and nanorod assemblies [27, 28]. Owing to the strong enhanced optical resonances supported by SPR and/or LSPR, a multitude of applications are enabled, including surface-enhanced sensors [29–32], light absorbers [33–36], light propagation controller [37], sub-diffraction imaging and nano-lithography [38], etc.

2.4.2 Hyperbolic Metamaterials

For any material, its effective dielectric permittivity tensor can be diagonalized as follows

$$\varepsilon_{eff} = \begin{pmatrix} \varepsilon_{xx} & 0 & 0 \\ 0 & \varepsilon_{yy} & 0 \\ 0 & 0 & \varepsilon_{zz} \end{pmatrix} \tag{2.23}$$

where the ε_{xx}, ε_{yy} and ε_{zz} are respectively the x, y and z components of the dielectric permittivity.

For simplicity's sake, all the components of the effective magnetic tensor are assumed to be positive and will not be discussed further in this thesis. The z-axis is selected as the optical axis, so the out-of-plane component which is in parallel with the optical axis, can be represented with the component along z-axis $\varepsilon_{||} = \varepsilon_{zz}$, while the in-plane components $\varepsilon_{\perp}$ consists of ε_{xx} and ε_{yy}. A general expression of the dispersion relation of a material can be presented as equation 2.24.

$$\frac{k_x^2 + k_y^2}{\varepsilon_{||}} + \frac{k_z^2}{\varepsilon_{\perp}} = \frac{\omega^2}{c^2} \tag{2.24}$$

where k_x, k_y and k_z are the components of the electromagnetic wavevector along the x, y and z optical axis, respectively, ω is the angular frequency, and c is the speed of light in vacuum.

In the case of TM-polarized electromagnetic wave, the dispersion relation for materials can be divided into several different cases according to the sign of dielectric permittivities along the three optical axes:

The isotropic media. The dielectric permittivity is the same along all optical axes $\varepsilon_{||} = \varepsilon_{\perp}$, so that the propagation of the electromagnetic wave is independent with the propagation direction, representing a closed spherical isofrequency surface.

The anisotropic media with positive components. The in-plane dielectric permittivities are equal to each other $\varepsilon_{||} = \varepsilon_{xx} = \varepsilon_{yy}$ but not to the out-of-plane component $\varepsilon_{\perp} = \varepsilon_{zz} \neq \varepsilon_{||}$, which means the propagation constant depends on the propagation direction. In this case, the wave vectors present a closed elliptical shown in Figure 2.7a.

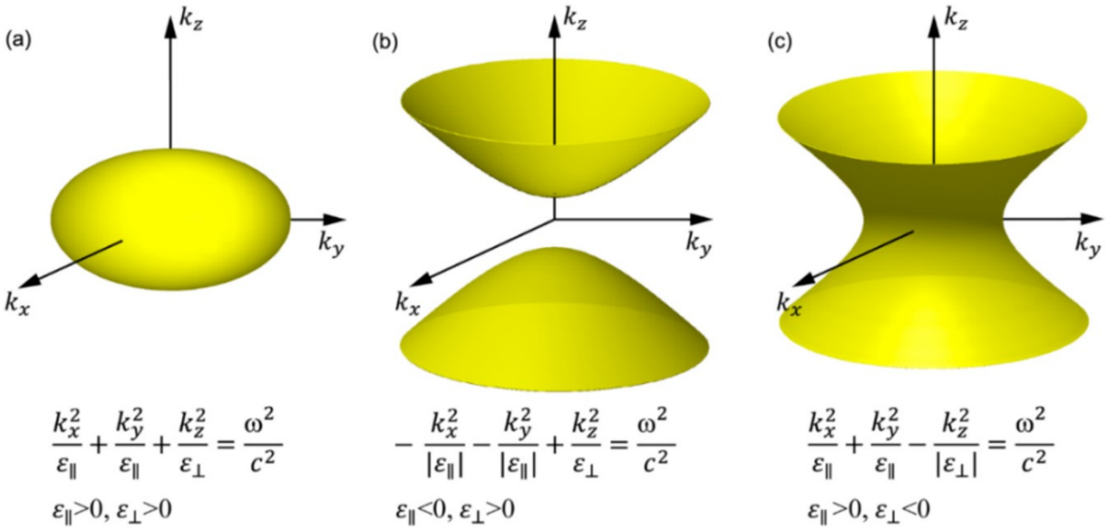

Fig. 2.7 Isofrequency surfaces for different types of media [39]: (a) a closed elliptical for a uniaxial material with $\varepsilon_\parallel \neq \varepsilon_\perp$, $\varepsilon_\parallel > 0$ and $\varepsilon_\perp > 0$, (b) opened hyperbolic for a uniaxial material of type I ($\varepsilon_\parallel < 0$, $\varepsilon_\perp > 0$), (c) opened hyperbolic for a uniaxial material of type II ($\varepsilon_\parallel > 0$, $\varepsilon_\perp < 0$).

The anisotropic media with positive and negative components is then classified as hyperbolic metamaterials, whose name comes from its hyperboloid-shaped isofrequency surface. There are two types of hyperbolic metamaterials. The type I is characterized with $\varepsilon_\perp > 0$ and $\varepsilon_\parallel < 0$, as depicted in Figure 2.7b, while the type II is characterized with $\varepsilon_\perp < 0$ and $\varepsilon_\parallel > 0$, as depicted in Figure 2.7c. The hyperbolic dispersion implies the existence of high wave vectors and strong local optical density in the region of the hyperboloid cones, which are usually beyond the optical properties of conventional materials.

From the dispersion relation of hyperbolic metamaterials, we know that, to realize hyperbolic metamaterials in practice, metallo-dielectric building blocks (meta atoms) are required to get the real part of $\varepsilon_\parallel$ and $\varepsilon_\perp$ having opposite signs of the effective dielectric permittivity. The dielectric media provides the positive dielectric permittivity in one direction, while the reflective metals provide the negative dielectric permittivity in the perpendicular direction, altogether leading to strong anisotropic optical properties. Regarding nanostructure design, two examples use metallo-dielectric building blocks to obtain hyperbolic metamaterials. One is a multilayered metamaterial consisting of alternating metallic and dielectric layers with a sub-wavelength thickness (typically $10-30$ *nm*). Thin-layer deposition techniques can achieve this type of multilayered nanostructure. The other one is a nanorod metamaterial. It's produced by an array of vertically oriented metallic nanowires/nanorods embedded in a dielectric matrix, and it is usually fabricated via anodization and electrodeposition. Figure 2.8 presents these two nanostructures.

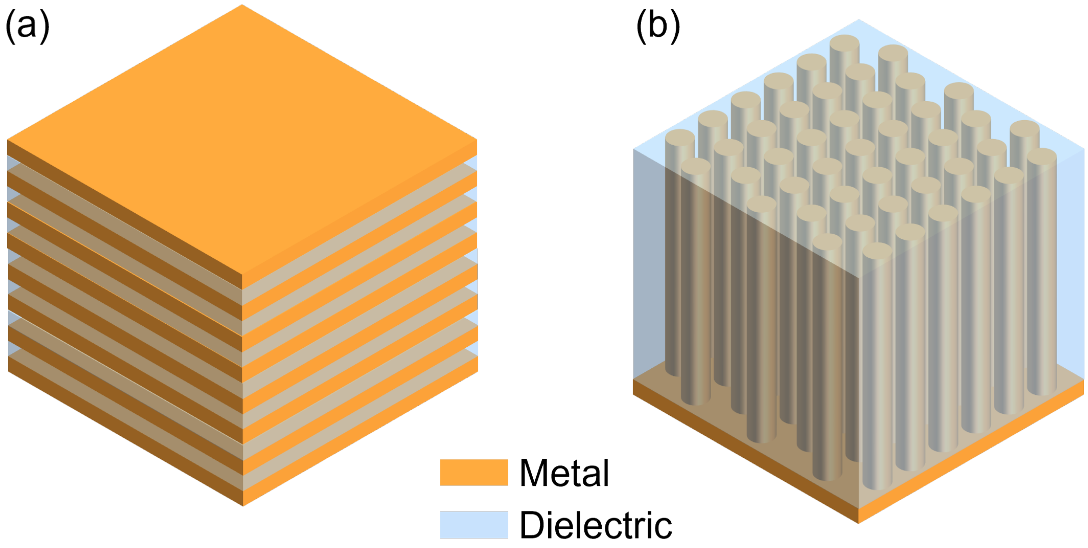

Fig. 2.8 Two different designs of nanostructure for hyperbolic metamaterials: (a) subwavelength metallic-dielectric multilayers, (b) dielectric matrix surrounded nanorods array.

The optical properties of these hyperbolic metamaterials are highly associated with the design of nanostructures. For instance, to have good metallic properties and simultaneously make energy loss as low as possible, a suitable metal must have a big real part and a small imaginary part in its effective permittivity. Noble materials such as gold and silver are often considered the most commonly used metal for showing excellent optical response in the visible spectral range. At the same time, aluminium is more useful in the ultraviolet spectral range. Apart from the choice of material, the geometric parameters of nanostructures also play a crucial role in the optical response. Taking a gold nanorod array, for example, its extinction spectra can be precisely tuned from visible to the near-infrared range with control over the length, diameter and inter-rods separation of the nanorods.

2.4.3 Effective Medium Theory

We can interpret metamaterials with theoretical approaches, such as Effective Medium Theory (EMT), often used to describe the optical properties of metamaterials and metasurface. From this perspective, P. Wan and A. Krasavin [39], etc. believe that "*An optical metamaterial is an artificially structured medium, whose optical properties can be described by an effective medium theory (EMT) providing an effective permittivity and permeability; in case of the* *metasurface, one can speak about an effective surface impedance.*". Using the EMT, one can derive the effective permittivities of hyperbolic metamaterials, including nanorod and multilayer metamaterials. For the nanorod metamaterials, the in-plane and out-of-plane components of the effective permittivity are given by [40, 41]

$$\begin{aligned} \varepsilon_{eff,\parallel} &= f\varepsilon_m + (1-f)\varepsilon_d \\ \varepsilon_{eff,\perp} &= \varepsilon_d \frac{(1+p)\varepsilon_m + (1-p)\varepsilon_d}{(1-p)\varepsilon_m + (1+p)\varepsilon_d} \end{aligned} \tag{2.25}$$

where ε_m and ε_d are the permittivities of the metal and dielectric media, respectively, while $f = \pi d^2/(2\sqrt{3}p^2)$ is the filling factor of the metal in the case of a hexagonal dielectric array, d is the nanorod diameter, and p is the periodicity of the nanorod array.

For the multilayer hyperbolic metamaterials, EMT gives

$$\begin{aligned} \varepsilon_{eff,\parallel} &= \frac{\varepsilon_d \varepsilon_m}{(1-f)\varepsilon_m + f\varepsilon_d} \\ \varepsilon_{eff,\perp} &= f\varepsilon_m + (1-f)\varepsilon_d \end{aligned} \tag{2.26}$$

where $f = t_m/(t_m + t_d)$ is the filling factor of metal for the alternating metal-dielectric multilayer, t_m and t_d are the thicknesses of the metal and dielectric layers, respectively [42].

Combined with the transfer matrix method, this EMT model can be used to derive the dispersion relations and describe well all the major optical properties of the hyperbolic metamaterials, such as the transmission, reflection and absorption spectra [43]. However, the local EMT presented above is based on the metamaterial homogenization approach and certain assumptions. For instance, the size of the nanostructure is required to be subwavelength because the valid wave vectors of metamaterial modes (k are expected to be smaller than the inverse of the size of structural elements ~$1/a$, a is the period of the nanostructure. Furthermore, this theory considers an ideal lossless case, but in reality, losses are unavoidable. Overall, these lead to the theory's limitation on the spectral and wave vector ranges [44]. For the detailed characterization of hyperbolic metamaterials, the non-local response of the composite is taken into consideration [45–48]. This non-locality (spatial dispersion) originates from the metamaterial nanostructures, which differs from the one from the plasmonic material response related to the complex free electron dynamics [49].

2.5 Fabrication of Plasmonic Metamaterials

The nanostructures design plays a crucial role in the government of the optical properties of plasmonic metamaterials, which requires state-of-the-art fabrication processes with nanometer-scale resolution. When selecting an ideal technique for realizing plasmonic nanostructures, many aspects must be considered. The spatial resolution is important for controlling and tuning the resonances in the desired spectral range, while the scalability is emphasized for industrial applications. Besides, materials quality is crucial because it affects the optical properties directly, and it might also be a concern if the final nanostructure has the potential for realizing functional devices with further treatment. Last but not least, equipment costs and the requirement for clean-room facilities must also be taken into account. Lithographic techniques are often used to make nanoscale patterns, which can then make desired nanostructures when combined with other techniques, such as thin film deposition and chemical etching. In general, lithography techniques, as a top-down technique, are suitable for sculpturing nanostructures with ultrahigh-resolution. However, they are limited by their scalability because they require individual direct writing for each pattern and thus are time-consuming. On the contrary, bottom-up approaches, such as self-assembly, provide a new opportunity for large-scale production because it is affordable and can offer a high possibility for realizing various structures. In this section, we introduce the most commonly used fabrication techniques for the geometrical design of plasmonic metamaterials.

2.5.1 Electron Beam Lithography

Electron beam lithography (EBL) is widely used to fabricate plasmonic metamaterials due to its ability to enable high spatial resolution (down to around 10 *nm*). A typical EBL fabrication procedure is illustrated in Figure 2.9. At first, the substrate is covered by a thin layer of electron-beam resist, which would go through a chemical reaction and alter its solubility/stability under the exposure of the electron beam. Relying upon the type of resist used, the exposed area either is dissolved (positive resist) or remains (negative resist) after washing in a chemical developer solution, thus forming a resist with the predesigned pattern. A thin layer of desired metal material can be deposited onto the substrate using film deposition techniques, such as chemical- or physical-vapour deposition. Thus, the metamaterial with the desired nanostructure is finally obtained after dissolving the residual resist (called the lift-off process). Optionally, additional steps such as reactive ion etching (RIE) and wet etching can be further performed to remove the undeposited region and the unwanted metal based on the aimed nanostructures. On the other hand, the desired thin film

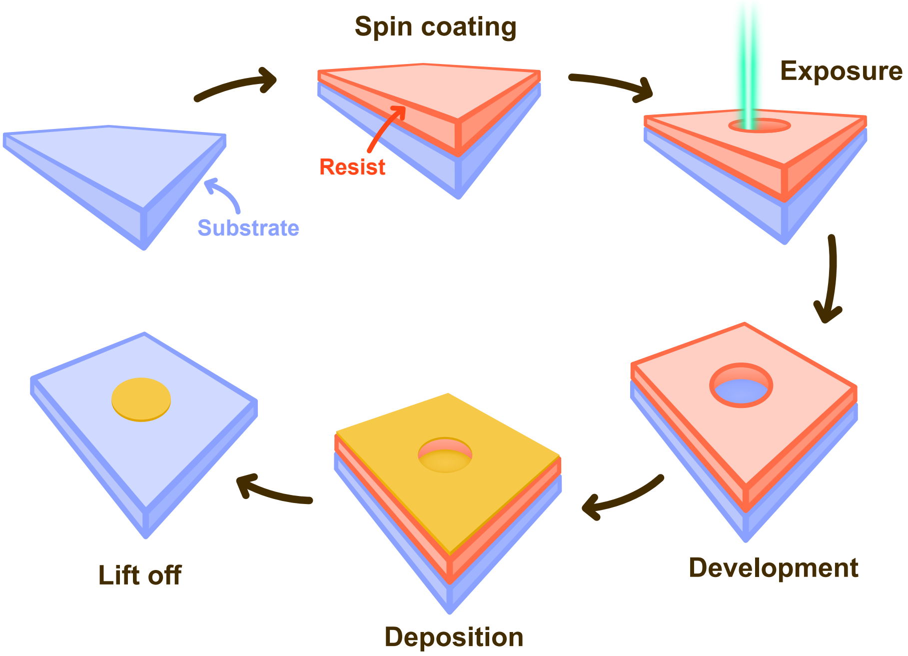

Fig. 2.9 Schematic showing the fabrication principle of EBL.

can be deposited on the substrate before the EBL is processed, in which case, the patterned resist acts as a hard mask that protects the underlayer film from subsequent etching and thus reveals the desired metasurface [14].

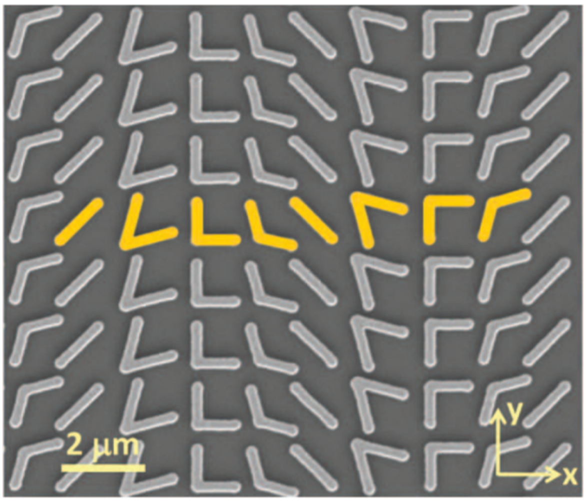

Fig. 2.10 SEM image of a gold V-shaped nano-antenna array fabricated via EBL [50]. The thickness and width of antennas are 50 *nm* and ~220 *nm*, respectively.

Figure 2.10 shows a scanning electron microscope (SEM) image of a gold V-shaped nano-antenna array fabricated by EBL [50]. The highly compact meta atoms of uniform shape and size at the nanoscale exhibit the excellent high resolution of EBL. Apart from two-dimensional metasurfaces, three-dimensional structures, such as multilayered metal-dielectric metamaterials, can also be realized if alternating metal and dielectric layers instead of the single metal film are deposited onto the patterned substrate [51, 52]. Despite the ultrahigh spatial resolution it can achieve, EBL suffers from its limited throughput and scalability, which results from the slow speed of point-by-point writing of focused electron beams.

2.5.2 Focused Ion Beam

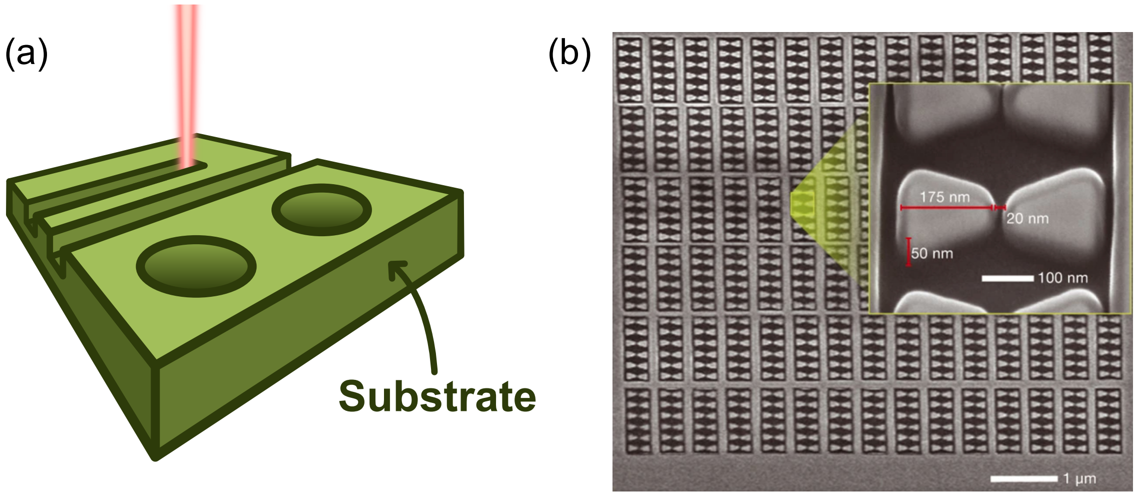

Fig. 2.11 (a) Schematic illustration of the direct ion milling of FIB. (b) SEM images of an array of gold bow-tie nanostructure fabricated via FIB. The inter-tie separation is 20 *nm* [53]

Focused ion beam (FIB) milling is a type of lithography technique where the desired nanostructures can be directly created on the substrate by the bombardment of the focused ion beam. Figure 2.11a illustrates the fabrication process of FIB schematically. Similarly to the EBL case, FIB allows an ultrahigh spatial resolution ($5-20$ *nm*) due to the use of nanoscale ion beams [54]. An array of gold bow-tie nano-antennas with 20 *nm* gap fabricated via FIB is presented in Figure 2.11b, showing the precise control of FIB on the nanostructures' dimension [53]. The fabrication speed of FIB is higher than EBL since it is free from a few time-consuming process steps. However, for such a mask-less technique that requires individual directing-writing, throughput and scalability remain inevitable challenges for the large-area fabrication of metamaterials with FIB.

2.5.3 Self-Assembly

Self-assembly is a process where individual components automatically build an organized structure once triggered by local mutual interactions, such as Van der Waals forces, molecular binding forces, electrostatic forces and capillary forces. Compared with other lithography techniques, self-assembly avoids the need for expensive instruments and cleanroom facilities, which makes it an affordable technique that can be widely used. Apart from the low cost, techniques based on self-assembly have also emerged as promising approaches to fabricating metamaterials because of their advantages in both high throughput and precise control of architecture designs.

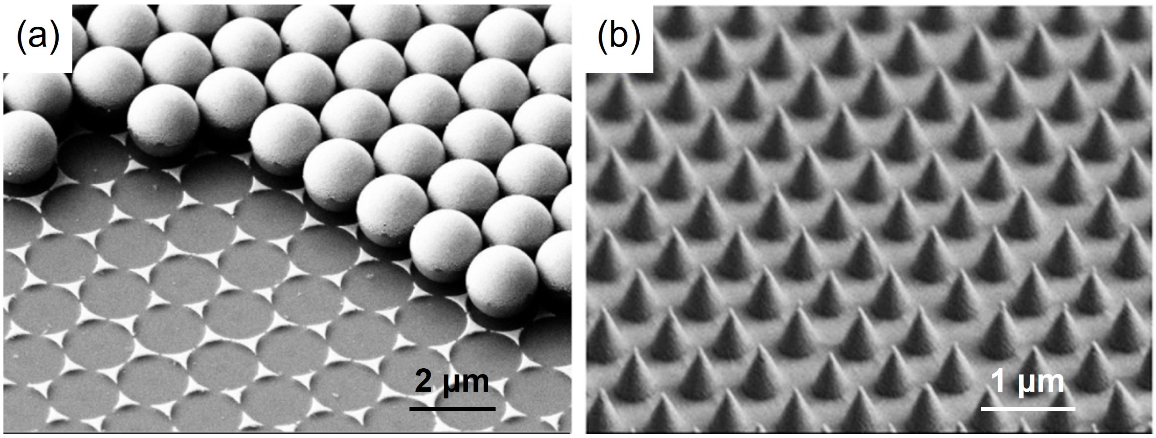

Fig. 2.12 SEM images of (a) gold nanotriangles and (b) sliver nanocones fabricated via template-assisted self-assembly techniques [55, 56].

There are two methods mainly based on self-assembly. One is the directed self-assembly processes, from which ordered metal nanoparticles array can be directly fabricated from colloidal solutions, leading to the formation of close-packed nanostructures with various shapes [57–59], such as nano-spheres, nanocubes, octahedra. Their optical properties, which are dependent on the interparticle gap and packing density, can be finely tuned by the length of polymer chains on the metal nanoparticles and the particle concentration, respectively, and therefore provides a lot of flexibility for various nanostructures construction [13, 58]. The other one is called the template-assisted self-assembly technique or colloidal nano-lithography. In this method, the highly ordered monolayers formed via self-assembly, which is often made of spherical polymer particles such as polystyrene, can be used as templates for fabricating plasmonic metamaterial in combination with other nanofabrication, such as thin-film deposition and etching techniques [60]. Several metamaterials with various shapes have been obtained using this method, including nano-triangles [13, 55] , nanoholes [61] and nanowires [62]. Figure 2.12 shows two representative nanostructures obtained via the self-assembly method combined with thin film deposition [55] and reactive ion etching [56], respectively.

2.6 Applications of Plasmonic Metamaterials

Supported by SPP and/or LSPs, plasmonic metamaterials have manifested their excellent ability to control local electromagnetic field intensity and field polarization and localize the field on sub-wavelength scales, which has provided new possibilities for the enhancement and government of light-matter interactions. Benefiting from the outstanding advantages, plasmonic metamaterials have been exploited in various applications, including ultrasensitive optical sensing, plasmon-enhanced spectroscopy, plasmon-assisted chemistry and catalysis. In this section, a brief overview of the applications of plasmonic metamaterials is provided.

2.6.1 Optical Sensing

Sensing has been deemed an important area in many industries where a high sensitivity and fast response are highly required (e.g., food safety, electronics, health and environment monitoring. Compared with the conventional electric sensors used predominantly, the optical sensors have been appreciated as a great sensing platform because of their advantages such as high sensitivity, fast response, immunity to electromagnetic noise and various signal retrievals. As mentioned before, due to the strong near-field electromagnetic confinement and enhancement, surface plasmons are extremely sensitive to tiny changes in the local surrounding medium, making optical sensing one of the most representative applications of plasmonic. The earliest reports can be traced back to more than 40 years ago when a probe of electrochemical interface [63] and detection of gas was demonstrated [64].

Biochemical Sensors

Plasmonic metamaterials are used for biochemical sensing based on their high sensitivity to the refractive index variations in the surrounding medium. Metal film-based SPP biochemical sensor has manifested its superior sensing ability with an extremely low LOD (~10^{-7} *RIU* [65, 66]). However, in terms of sensing small molecules, its performance is limited due to its relatively weak electromagnetic confinement that comes with the relatively smooth film surface, which is exactly the opposite case for the LSP-based sensors, which are more suitable for small molecule sensing but suffering from its relatively lower overall RI sensitivity [67, 68]. Benefiting from their flexibility in nanostructure engineering and optical responses, plasmonic metamaterials have offered a powerful platform for biochemical sensing compared to smooth metal films and individual nanostructures. A multitude of plasmonic metamaterials with various geometries have been reported in the past decades, such as nano-hole arrays [69, 70], split-ring resonator [71, 72] and nanorod array [73, 28]. Among all, hyperbolic metamaterials have drawn significant attention and exhibited a record-performances in the field of biochemical sensing [74–76].

Hyperbolic nanorod metamaterials, for instance, their optical response depends on the plasmonic response of the individual nanorod and the coupling between them. And the related optical modes for their outstanding sensing performance can be explained with the local EMT theory (see section 2.4.3). Gold nanorods array-based sensors have shown an ultra-high RI sensitivity (3.2×10^4 nm/RIU) for the label-free biochemical sensing, which is around two orders of magnitude higher than the sensitivity of LSP-based sensors [28, 67, 68]. This type of sensor also reached a higher value of FOM_λ compared with those of SPP- and LSP-based sensors [28, 65, 67, 68]. This sensing performance can be improved furthermore to a bulk RI sensitivity of 4.16×10^4 nm/RIU and FOM_λ of 416 if improving the uniformity of nanorods array using electron beam lithography technique [77].

Apart from nanorod metamaterials which require ATR-based or oblique illumination with TM-polarised light, there are more nanostructure designs, such as nanotube and coaxial rod-in-a-tube metamaterials. These metamaterials can be excited directly at normal incidence but have a relatively smaller RI sensitivity (< 300 nm/RIU) [78, 79]. In addition to the substrate-supported metamaterials, hyperbolic metamaterials in the colloidal form, meta-particles, can also be used for optical sensing applications because of their strong local-field enhancement and highly tunable spectral resonance range [80].

Besides increasing sensitivities, reducing the fwhm of metamaterials resonances and increasing the FOM values is also important to improve the overall sensing performance. This can be achieved by coupling a broad plasmonic resonance with Fano resonance mode with narrow line widths, thus leading to high sensitivity in detecting mono-/bilayers proteinc [81].

Gas Sensors

Based on the high sensitivity to environmental change, plasmonic metamaterials have also been applied for various gas sensings, such as hydrogen, relative humidity, carbon monoxide/dioxide, and volatile organic compounds [34, 82–84]. We here take plasmonic hydrogen sensing, for example, to show the variety and development of plasmonic gas sensors.

Compared with their electric counterpart, plasmonic hydrogen sensors are attractive for safe use in harsh environments because they are free from the risk of electromagnetic interference and electric spark generation [85]. Typical hydrogen sensors are based on the chemical/physical transformation of the metamaterials, thus leading to a significant change of RI that can be eventually reflected in the optical response change of the plasmonic metamaterials. As a typical transition metal for hydrogen sensing, palladium would go through both volume expansion and phase transition (forming hydride) once exposed to H_2. A range of plasmonic nanostructures have been designed for hydrogen sensors, such as nanowire arrays [86, 87], dendritic arrays [88] and nanohole arrays [70]. For Pd nanorods in a porous alumina template, the hydrogen sensing efficiency can be further improved via dissolving the AAO template, which would increase the high specific surface area of palladium nanorods to hydrogen and thus increase the chance of palladium interacting with hydrogen atoms [29]. However, due to the limitation of pure Pd-based hydrogen sensors (e.g., hysteretic behaviour and long response time), more and more effort has been made to find more suitable hybrid structures, including using palladium-alloy, combining with polymer layers and adapting core-shell nanostructures [89–92].

2.6.2 Surface-Enhanced Spectroscopy

Another important application of surface plasmons is surface-enhanced spectroscopy, which uses the local field enhancement of scattering of emitters near metal nanostructures.

One example is surface-enhanced Raman scattering (SERS). Raman effect is the inelastic scattering of photons by matter, which is induced by the energy exchange of the incident photons interacting with materials. And because this effect is associated with the vibration, rotation and other states of chemical bonds and can be denoted with specific spectral shifts, it has been widely used to probe the composition of materials. Exploiting the local field enhancement of surface plasmons, SERS has been developed to amplify Raman signals by placing the molecule within the near-field of a plasmonic metamaterial. The cross-section of typical Raman scattering is quite small, which is around 10^{-31}-10^{-29} $cm^2/molecule$. However, by using SERS, the detection sensitivity has been pushed down to signal-molecule level, and the small cross-section has been modified [93–95]. Furthermore, to overcome the limitation that comes with conventional SERS substrates, plasmonic metamaterials have been considered a better alternative for SERS spectroscopy since they can support uniform and reproducible SERS signals due to their controllable and reproducible fabrication [96, 97].

The other example of surface-enhanced spectroscopy is surface-enhanced infrared absorption (SEIRA). Like SERS, infrared absorption spectroscopy is also a technique for chemical identification, whose IR absorption can be significantly enhanced with the help of surface plasmon-enhanced light-material interactions and, therefore, have a high detection sensitivity of molecules. A multitude of metal-based plasmonic metamaterials has been developed as the substrate of SEIRA with high reproducibility and strong signal enhancement [98–100]. In addition, by integrating metamaterial with a stretchable substrate, such as polydimethylsiloxane (PDMS), the operating frequencies of plasmonic metamaterials for SEIRA can be tuned precisely with external mechanical force, which as a result, broadens the detection range of vibrational modes of analytes [101]. Furthermore, other materials, including graphene, doped semiconductor and metal oxide, have also shown desired optical response in the infrared spectral range, which allows consideration of new materials for the plasmonic enhancement of SEIRA spectroscopy [102–104].

Fluorescence Enhancement is another important application of surface plasmons. The fluorescence emission of molecules can be enhanced by placing them near a metallic surface or metallic nanostructures where the local electromagnetic field is enhanced. The presence of plasmonic metamaterials can provide desirable effects such as increased quantum yield, decreased lifetime and better fluorophore photo-stability, further promoting the practical use of fluorescence enhancement in bioimaging applications [105–107].

2.6.3 Other Applications

Besides the above applications, there are also applications based on the principle of photon-electron energy conversion, such as photovoltaics and photodetectors.

The efficient conversion of photon energy into electricity is playing an increasingly important part in satisfying global energy demand and long-term environmental sustainability. There are several general requirements to consider for these fields, including light absorption, charge carrier transport and separation. From a material perspective, plasmonic metamaterials, in this case, can enhance light absorption by the engineering of the local optical density and also by using diverse light trapping techniques (Fabry–Pérot resonances, guided modes, refractive index gradients and diffraction, etc.). And therefore, this can decrease the cost of materials and fabrication and increase the range of material choices. The tunable resonances of metamaterials offer a convenient way to achieve the precise control of light absorption and photo-current enhancement by engineering the size and arrangement of individual meta atoms [108, 109]. Once charge carriers are generated by the nonradiative decay of surface plasmons, they are expected to be efficiently separated and transported to be collected before they recombine and consequently lose energy as heat. In this regard, plasmonic metamaterials are employed to reduce the recombination losses of hot carriers by providing small charge carrier diffusion lengths due to their nanosized individual building blocks [110]. The tunability of the optical properties via geometric engineering also offers hot-electron-based photodetectors a lot of flexibility in the control of spectral range and polarization dependence.

Furthermore, these highly energetic charge carriers that caused by the high energy transferred from the incident light excitation become extremely hot/active for a brief period and can be extracted and used to drive photochemical reactions such as H_2 dissociation and water splitting [111–114]. On the one hand, plasmonic metamaterials can offer a platform for photonic engineering because of their tunable broadband spectral resonance range via direct architecture adjustments, thus leading to enhanced light harvesting with the increase of the solar light absorption capacity and the consequent hot carriers generation. Furthermore, compared with flat bulk materials, metamaterials possessing large-surface-area nanostructures play a significant part in the photocatalytic efficiencies enhancement as they provide plentiful catalytic active sites at the interface or surface of materials for chemical reactions to occur [115–117].

Other than solar water splitting, plasmon-assisted photochemistry and photocatalysis have also been applied to other fields, including solar-driven organic synthesis [118–120], organic compounds degradation, and CO_2 reduction [121, 122]. More advanced functionalities and a wider range of chemical reactions are expected to be further exploited and studied in the future with the benefit of nanophotonics and plasmonic metamaterials.

More recently, with the increasing demand for comprehensive development, exploiting hybrid systems has been considered an attractive way to fulfil the potential of plasmonic metamaterials in more complex applications. Despite many promising properties, certain desirable properties are required for some practical applications that are beyond the reach of solo plasmonic components. In this case, an additional component with new functional properties to the current architecture, either in materials, nanostructures or approaches, is needed to build a hybrid system with combined advantages.

Taking photocatalysis for example, while the plasmonic component can enhance light harvesting and transfer energy via charge carriers, heat or EM field, the second material can aid the hybrid system in terms of the catalytic activity, the charge carriers' lifetime and the overall system stability, etc. Various forms of the hybrid plasmonic system have been demonstrated from the perspective of materials, including metal-metal, metal-semiconductor, metal-2D materials, metal-MOF, metal-polymer, etc. Different hybrid nanostructures of colloidal plasmonic metamaterials such as core-shell and core-satellite have also been widely used to obtain improved performances [123, 124].

In addition, hybrid approaches have also been taken on other complex platforms where multiple fields combine at the nanoscale, such as chemistry, electronics and photonics. A good example is a reactive plasmonic tunnel junction where a plasmonic gold nanorod array combines with metal-polymer-metal tunnel junctions [125]. Once applied external voltage bias is present, electrons generate from one electrode and tunnel through the ultrathin polymer gap to the gold nanorod side. During this process, hot electrons form mainly through elastic tunnel electrons and the nonradiative relaxation of plasmonic mode that is excited by inelastic tunnel electrons. Additionally, the surface plasmons in the metamaterial can radiatively decay into photons, leading to measurable light emission. The efficient formation of hot electrons makes the tunnel junctions highly confined catalytic spots for precise chemical reactions, which can be further detected by the light emission intensity and tunnelling current simultaneously due to their strong dependence on the change in the tunnelling junction. For this hybrid system, hot-electron-activated nanoscale reactors and highly compact optical sensors have been realized on this hybrid device, which opens up opportunities for studying fundamental physical processes at the nanoscale and constructing lab-on-chip devices.

The use of hybrid components in combination with plasmonic metamaterials has already exhibited the huge advantages of hybrid plasmonic metamaterials. And it may lead to a new route towards the realization of versatile metamaterials for a wider range of applications.

Chapter 3

Plasmonic Nanorod Metamaterials

This chapter highlights the fabrication process of plasmonic gold nanorod metamaterials, including metallic film sputtering, template anodization and electrodeposition. The general characterisation techniques used to study the geometrical characteristics are presented, and a home-built setup used for optical properties measurement is finally described.

3.1 Optical Properties of Nanorod Metamaterials

The effective permittivity of the nanorod metamaterial can be calculated with the local effective medium theory described in section 2.4.3. As we can see from Figure 3.1, the real parts of the dielectric permittivity perpendicular to the optical axis $Re(\varepsilon_{eff,\perp})$ are always positive, while the component along the optical axis $Re(\varepsilon_{eff,\parallel})$ changes sign at the wavelength around 515 *nm*, and thus divides the optical response of the nanorod metamaterials into three regions: the elliptical (short wavelength) region, where $Re(\varepsilon_{eff,\parallel})$ is positive and dielectric characteristics dominate the metamaterials; the hyperbolic (long wavelength) region, where $Re(\varepsilon_{eff,\parallel})$ is negative and the metamaterial exhibits a metal-like behaviour; between them is the epsilon-near-zero (ENZ) region, where $Re(\varepsilon_{eff,\parallel})$ is around zero. In the ENZ region, the optical properties are extremely sensitive to the change of refractive index of the surrounding media, which has been used for applications such as ultrafast all-optical switching [126, 127] and polarisation control [128].

The strong nonlocality (spatial dispersion) in the ENZ region results in the appearance of three different optical modes: one is TE-polarized, and the other two are TM-polarized. As seen in Figure 3.2, two distinctive peaks can be observed from the extinction spectrum of a nanorod metamaterial [129]. The short-wavelength peak is related to $Re(\varepsilon_{eff,\perp})$ and can be observed for both TE- and TM-polarized waves. In contrast, the long-wavelength peak is

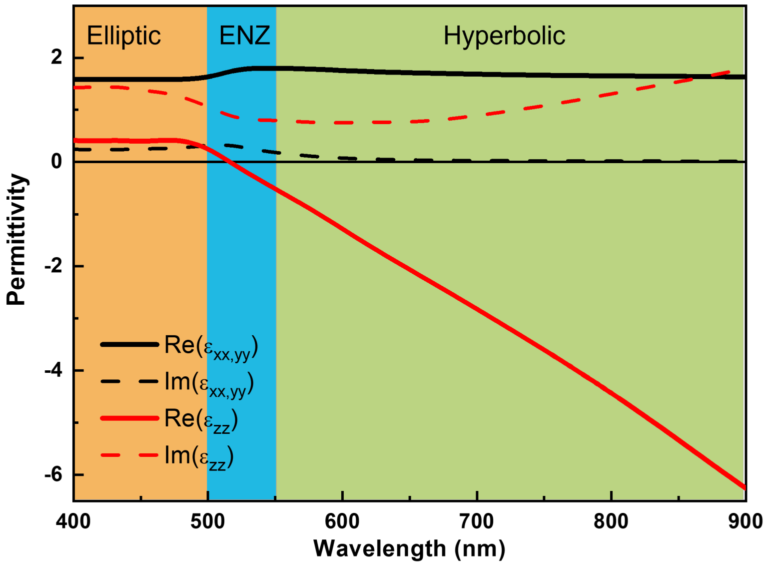

Fig. 3.1 Real and imaginary parts of the effective permittivity of a nanorod metamaterial in an alumina matrix. The parameters of the nanorods are nanorod diameter 50 *nm*, nanorod length 230 *nm* and inter-rod separation 100 *nm*.

related to $Re(\varepsilon_{eff,\parallel})$ and only appears for TM-polarized wave, which has a parallel electric field component to the optical axis.

From a microscopic perspective, the origin of these extinction peaks can be understood by the two dipolar LSP resonance of individual nanorods. The short-wavelength peak originates from a transverse plasmonic mode (T-mode), often located in the visible spectra range and associated with the free electron excitation perpendicular to the nanorod axis. This peak is corresponding to the peak in the imaginary part of the effective permittivity $Im(\varepsilon_{eff,\perp})$, indicating the absorption of the metamaterials. On the other hand, the long-wavelength peak originates from a longitudinal plasmonic mode (L-mode) in the near-infrared spectral range, which is related to the electron motion in the direction of along the nanorod. However, when placing these nanorods closely in a matrix, the cylindrical surface plasmons start to interact and thus generate a collective plasmonic resonance, arising novel optical phenomena [41]. Compared with the longitudinal dipolar resonance of individual nanorods, this collective plasmonic resonance causes a remarkable spectral shift towards the shorter wavelength accompanied by an enhanced local electromagnetic field in the nanoscale hotspots. The plasmonic resonances of the nanorod metamaterials can be tuned in the visible and near-

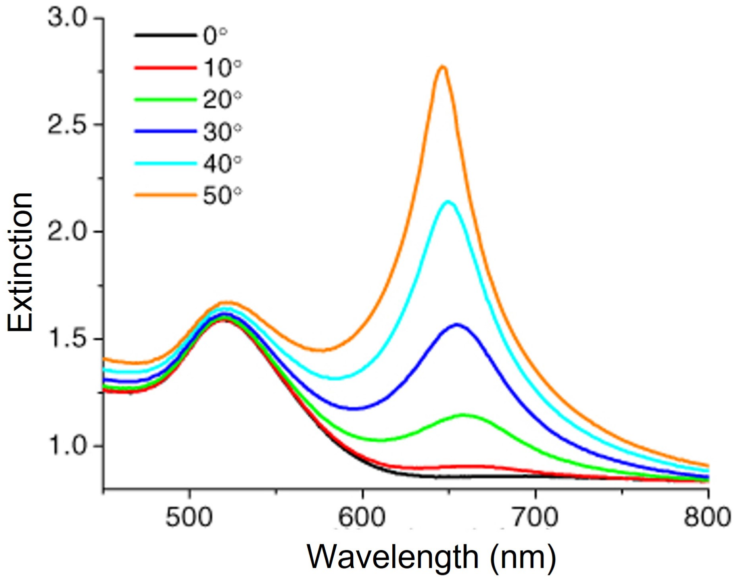

Fig. 3.2 Extinction spectra of a nanorod metamaterial in an alumina matrix [129]. Extinction here is expressed with transmission T as $-\ln T$.

infrared spectral region by tailoring the aspect ratio of the nanorods (ratio between length and diameter), inter-rod separation and the constituting media. Apart from these dipolar resonances, more modes, such as slab waveguided modes and Fabry-Perot modes, can also be supported by the hyperbolic metamaterials and observed from the associated spectral features [129, 130].

3.2 Standard Fabrication of Nanorod Metamaterials

Plasmonic nanorod metamaterial, which consists of a periodic array of metallic nanorods on a substrate, is mainly used as experimental samples in the following chapters. Anodic aluminium oxide (AAO) template-based pattering is used to fabricate a general gold nanorods-based sample and will be described in detail. The whole standard fabrication procedure of the nanorod-based metamaterials is shown in Figure 3.3.

3.2.1 Sputtering of Bottom Layer

The first step is to prepare a multilayered substrate for the porous templates the nanorods will subsequently embed. This is achieved by the magnetron sputtering coating of physical vapour deposition (PVD). The main principle of deposition is that atoms are ejected from a solid source (target materials) by the bombardment of high-energy ions in a high vacuum and are

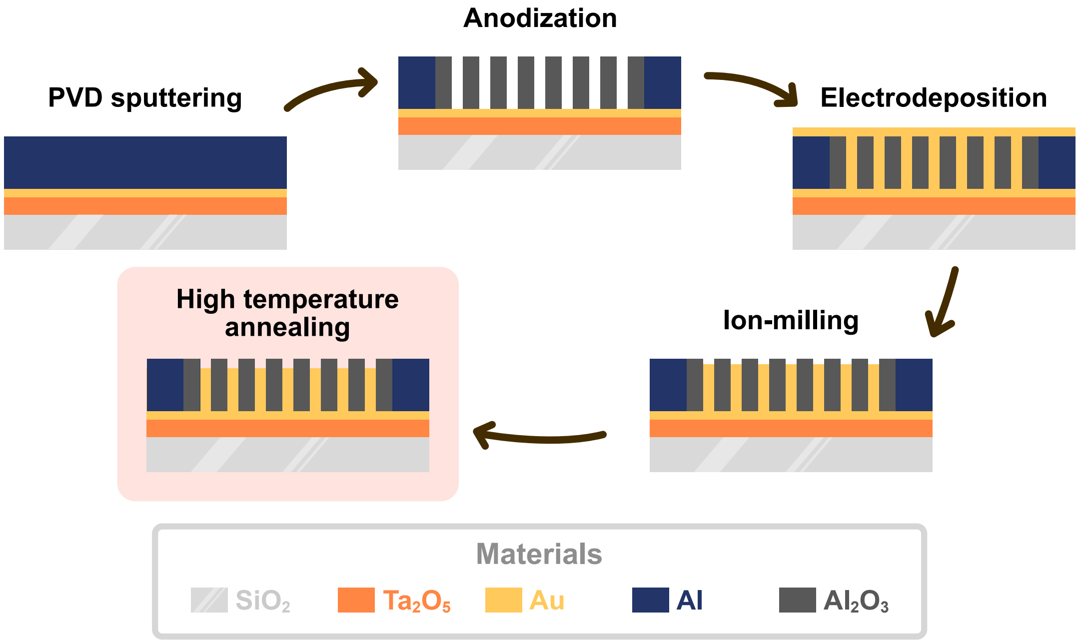

Fig. 3.3 Schematic diagram showing the standard fabrication steps of the nanorod-based metamaterials.

then deposited on the substrate forming a metallic film [131]. In our case, the multilayered substrate is formed by the sequential deposition of a ~10 *nm* tantalum pentoxide (Ta_2O_5) layer, a ~8 *nm* thick gold film and an aluminium layer on a 1 *mm* thick glass slide. The Ta_2O_5 layer acts as an adhesive layer between the glass substrate and Au layer, while the Au bottom layer works as an electrode for the subsequent electrochemical reaction. The Al layer is used to produce the porous AAO template. By controlling the Al layer's thickness, the AAO template's thickness and, thus, the maximum length of gold nanorods can be determined.

3.2.2 Anodization of Aluminium Layer

The AAO template, which consists of a quasi-periodic array of nanopores, is subsequently generated by the anodization of the aluminium layer. The geometric parameters of the AAO template, such as nanopore diameters and separation, can be regulated by the anodization conditions, including the applied bias, the concentration and the type of electrolyte solution. Typically, using voltages ranging from 20 V to 60 V in the oxalic acids or sulfuric acids, high-density nanopores with diameters of $12-60$ *nm* and separations of $50-150$ *nm* can be readily obtained. Because the nanopores form randomly at the beginning of the electrochemical reaction and only get gradually ordered after long-time anodization, it is necessary to carefully remove the random nanopores on the aluminium surface and make space for the

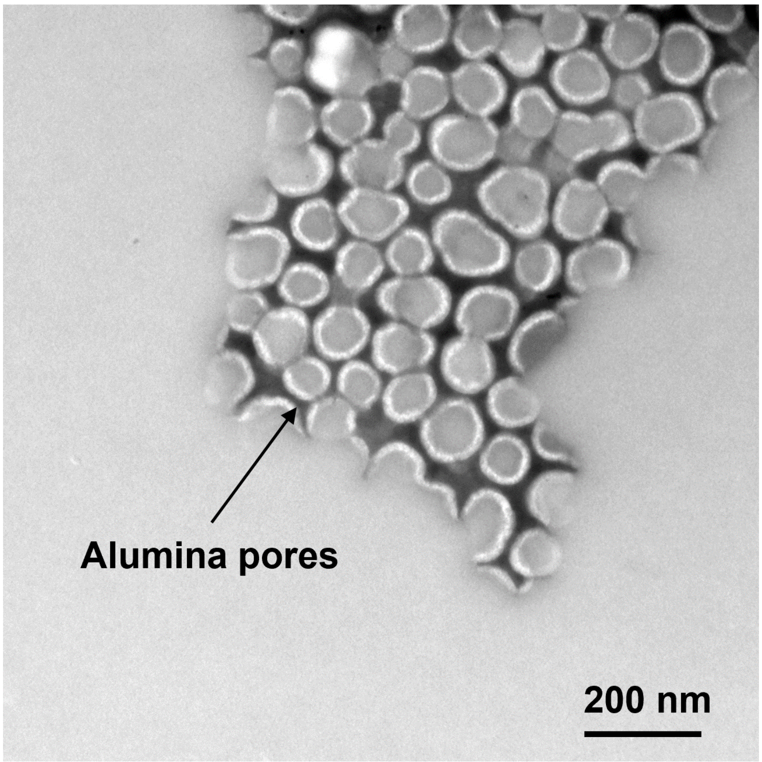

Fig. 3.4 TEM image of AAO template peeled from the glass substrate.

highly ordered nanopores guiding the succeeding electrodeposition of nanorods. This process is called the two-step anodization. Specifically, a certain thickness of an aluminium layer is firstly anodized into an AAO layer, which is then etched away in a solution of phosphoric acid (H_3PO_4) and chromic acid (H_2CrO_4), leaving an ordered array of dents on the surface of rest aluminium layer for the second anodization. Lastly, an additional etching process in the sodium hydroxide (NaOH) solution is used to dissolve the possible barrier layer between the bottom of nanopores and the gold layer, thus preventing the insulation of the gold electrode and widening the diameter of nanopores. Figure 3.4 depicts a TEM image of a part of an AAO template peeled from the substrate, from which a periodic array of alumina nanopores can be observed.

3.2.3 Electrodeposition of Gold Nanorods in Alumina Template

Au nanorods are finally prepared by the electrodeposition of gold into the porous AAO templates from a gold chloride-based solution. The length of Au nanorods in the assembly can be changed by simply altering the deposition time, while, as mentioned before, the upper bound of length is set by the thickness of the AAO template. Alternatively, Au nanorods are intentionally overgrown to fully fill the AAO nanopores until a uniform Au layer is formed

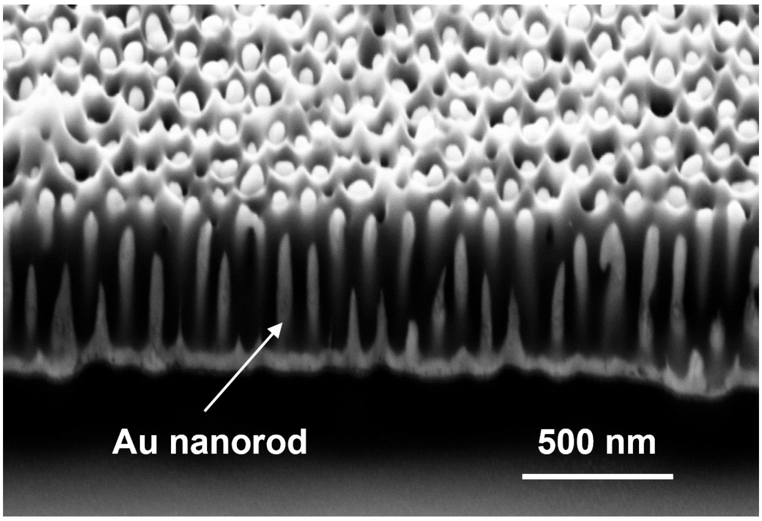

Fig. 3.5 Cross-section view of a nanorod metamaterial showing gold nanorods embedded in a porous AAO template with the nanorod length of around 420 *nm*.

on the top of the AAO template, and the samples are then chipped to the desired length using the ion-milling process described in the next subsection. Figure 3.5 shows a cross-section SEM image of the nanorod metamaterial where gold nanorods are uniformly embedded inside the AAO template after electrodeposition.

3.2.4 Ion Milling of Plasmonic Nanorod Metamaterials

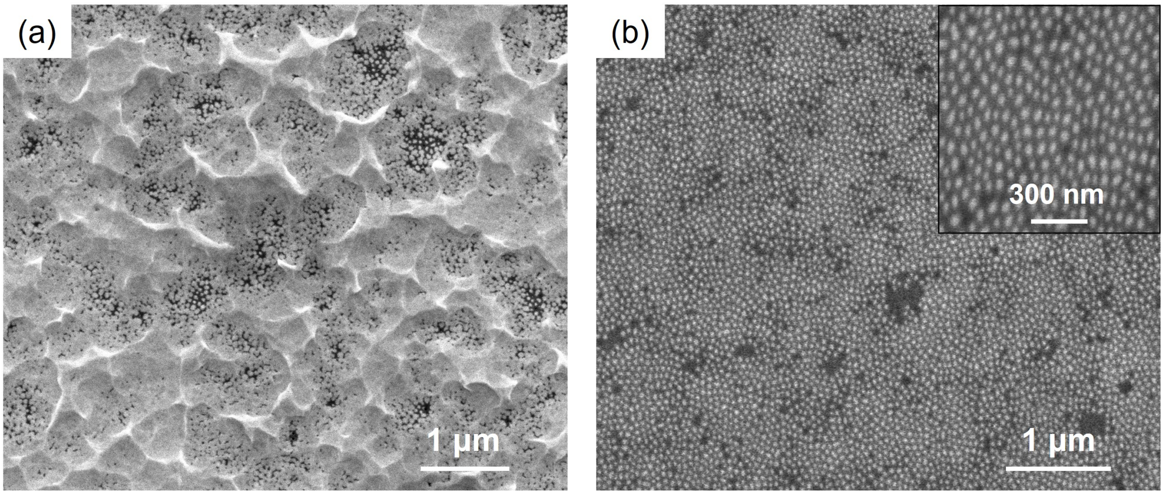

Fig. 3.6 SEM views of a nanorod metamaterial (a) before and (b) after ion milling, respectively. The magnified SEM image inserted shows the average nanorod diameter is ~56 *nm*, and the average inter-rod spacing is ~70 *nm*.

To remove the redundant Au layer and make the Au nanorods, the as-fabricated nanorod metamaterials are often further ion-milled (V6000 mill and sputter system, Scientific Vacuum Systems). The milling process is operated with the following parameters: a base pressure of 2×10^{-6} $mBar$, an acceleration voltage of 1000 V, a beam voltage of 500 V, a beam current of 23 mA, a sample holder rotation speed of 58 RPM. The milling oblique angle to the sample surface is set at 15°, and the milling time ranges from 20 to 50 minutes to obtain the desired length of gold nanorods. Due to the difference in the material hardness, the milling rate of AAO is about one order of magnitude lower than that of Au under the same condition [132], which also means the hard AAO matrix acts as a block to protect the embedded soft gold nanorods from being milled away too quickly (shadowing effect), thus consequently leading to the Au nanorods being several nanometers lower than the surrounding AAO template. After ion milling, the nanorod metamaterials are stored in ethanol in case of any contamination in the air. Figure 3.6 presents the surface morphology change of a plasmonic nanorod metamaterial before and after ion milling, respectively. It can be seen that the overgrown gold layers have been completely removed after milling, thus revealing the uniform gold nanorod array. The diameter and separation of nanorods can be easily measured from the SEM images inserted.

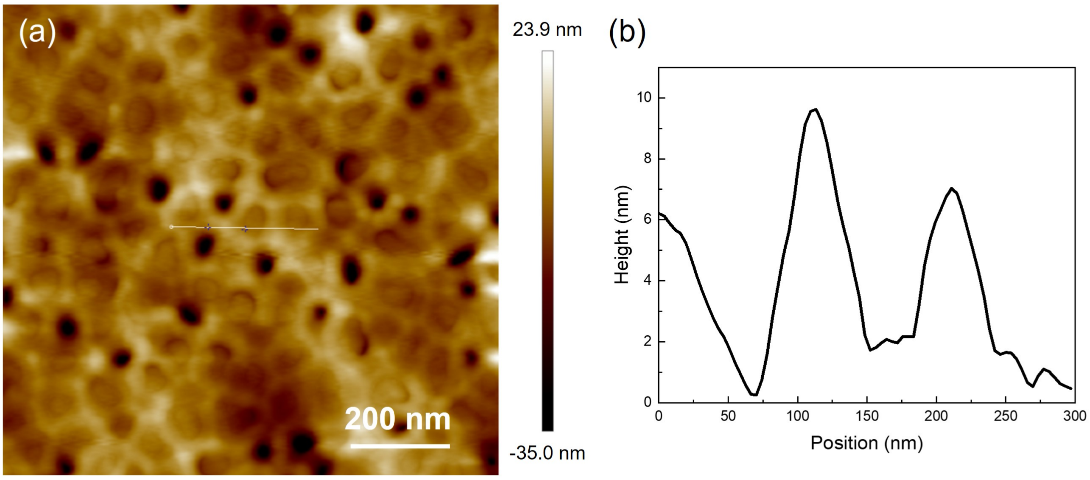

Fig. 3.7 (a) AFM topography of a nanorod metamaterial after ion milling. (b) Height contour across the line in (a).

Figure 3.7 shows the surface topography of a nanorod metamaterial after ion milling using AFM, from which the height difference between gold nanorods and AAO matrix can be observed. In this image, the AAO matrix is 5-10 nm higher than the embedded gold nanorods, confirming that the AAO can act as a shield for gold nanorods when milled at a very small milling angle.

3.2.5 High Temperature Annealing

The optical properties of gold nanorods can be strongly affected by the quality of nanorods (e.g. size of the gold crystalline grain, defects on gold nanorods). We used heat treatments to improve the quality of nanorods and thus the optical properties towards the theoretical limits of current bulk gold materials. This is done with high-temperature annealing at around 300 °C for two hours in the air, after which the gold nanorods would get more compact with a longer mean free path [133]. The length of gold nanorods would decrease slightly after annealing due to the resulting higher density. Thus, the gold nanorod metamaterial embedded in the alumina matrix is obtained after this standard fabrication procedure.

3.3 Construction of Hybrid Structures

Sometimes, additional treatments are used to modify the structures of general gold nanorods-based metamaterials for different applications. More details about each step can be found below.

3.3.1 Wet Chemical Etching of Alumina Template

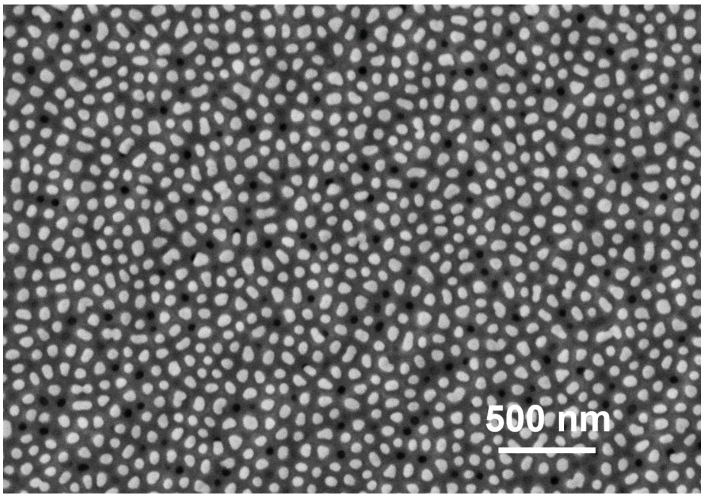

Fig. 3.8 SEM planar view of the nanorod metamaterial after wet chemical etching.

For fabrication of a plasmonic tunnelling junction, the usual steps as described before were followed to obtain gold nanorods array, in which case, the gold nanorods are 5-10 *nm* lower than the surrounding AAO matrix in the nanorod metamaterials after high-temperature annealing. However, to expose the nanorod tips for the subsequent tunnelling junction construction, the alumina surrounding must be several nanometers lower than the gold nanorods, which can be achieved using the wet etching method.

Briefly, the nanorod metamaterial stored in ethanol was firstly dried under N_2 and then put into 5 *mL* H_3PO_4 (3.5%) at 35°C for 10 *min* to remove about 20 *nm* surrounding AAO matrix. The etching depth can be controlled by the etching conditions, such as solution concentration, etching time and temperature. After etching, the metamaterial was rinsed several times with deionized water (18.2 $M\Omega$) to remove residual chemicals on the surface and then kept in DI water for future use.

Figure 3.8 shows the surface morphology of a plasmonic nanorod metamaterial after the wet etching using SEM. The sample surface is relatively smooth, and the uniform distribution of bright spots indicates that the nanorods are uniformly embedded in the surrounding AAO matrix. The average diameter of a nanorod is 50 *nm*, while the centre-to-centre separation between the nanorods is around 100 *nm*.

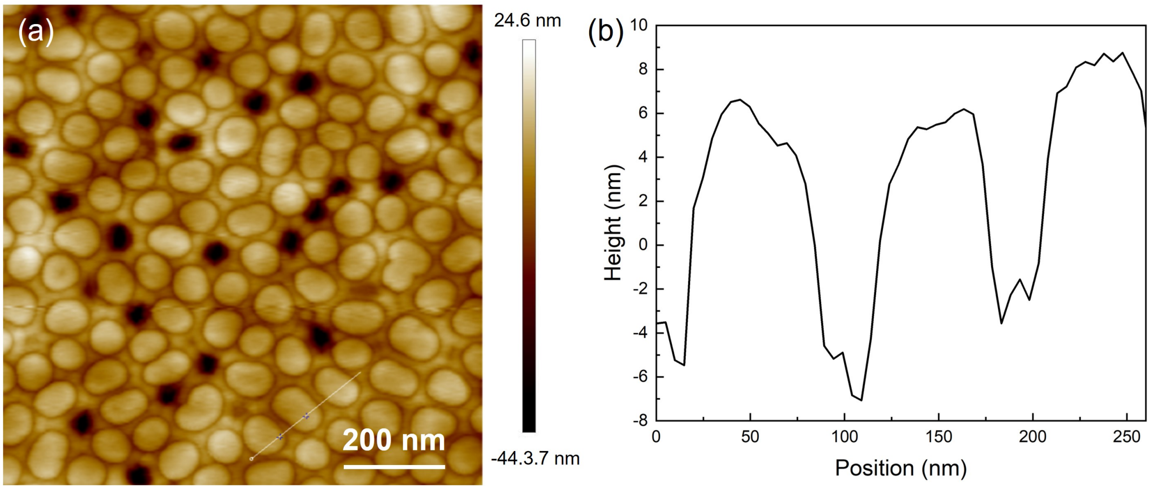

Fig. 3.9 (a) AFM topography of the plasmonic nanorod metamaterial after the wet chemical etching. (b) Topographical cross-section along the line in (a).

Figure 3.9 shows an AFM image of the nanorod sample surface and the line profile of nanorods inside the matrix. It can be seen that the nanorod tips are about 10 *nm* higher than the surrounding AAO matrix, which is good for the following polymer attachment and, eventually, the development of plasmonic tunnelling junctions (PTJs). In addition, the average periodicity of around 100 *nm* can be confirmed by measuring the inter-rod separation multiple times. As Figure 3.9b shown, two periods were measured along the line in Figure 3.9a.

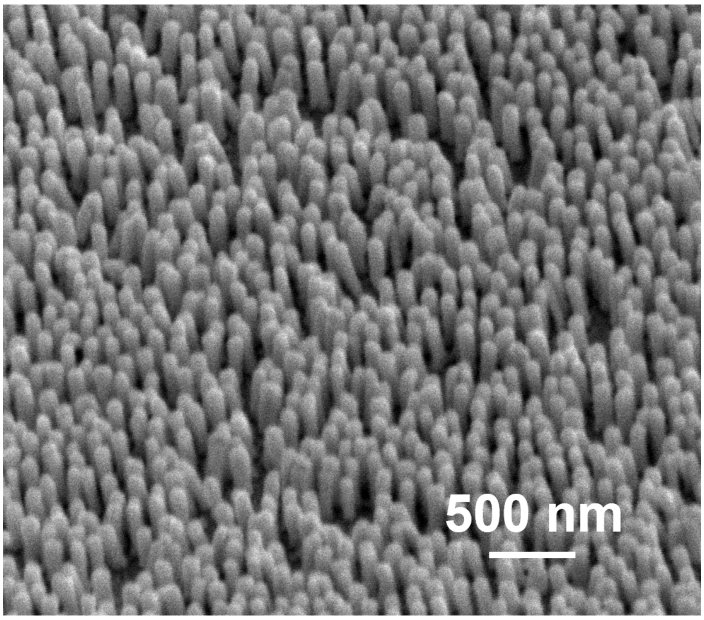

Fig. 3.10 SEM image of the bare gold nanorod metamaterial [134].

On the other hand, to fully expose the nanorod for sensing applications, the alumina matrix was completely removed using wet etching to get a freestanding gold nanorod array (in the following, it is addressed as a bare nanorod array). Figure 3.10 shows a typical scanning electron microscopy image of the bare gold nanorod metamaterial, in which high-density freestanding gold nanorods on a substrate can be observed. The average diameter, length and separation of the nanorods in the assembly we measured to be approximately 50, 230 and 100 *nm*, respectively.

3.3.2 Self-assembly of Polymer Monolayer on Nanorods

A PLH-coated gold nanorod array was further obtained via a molecular self-assembly approach [125]. In brief, a PLH solution was first prepared by dissolving ~5 *mg* of a PLH powder into 5 *mL* of deionized water with its pH adjusted to 5–6 using 0.1 *M* HCl. A bare gold nanorod array was then immersed into the PLH solution for ~30 *min*. Due to the high affinity of the functional groups of PLH to gold, a monolayer of the PLH layer was self-assembled on the gold nanorod surface. After rinsing with deionized water and drying under a N_2 flow, the PLH-coated nanorod array was obtained.

Self-assembly monolayers (SAMs) were used to functionalize the surface of the gold nanorods with a polymer monolayer. Firstly, 5 *mg* poly-L-histidine (PLH, M_w 5,000-25,000, Sigma-Aldrich) powder was dissolved into 5 *mL* DI water and ~0.2 *mL* HCl (0.1 *M*) was

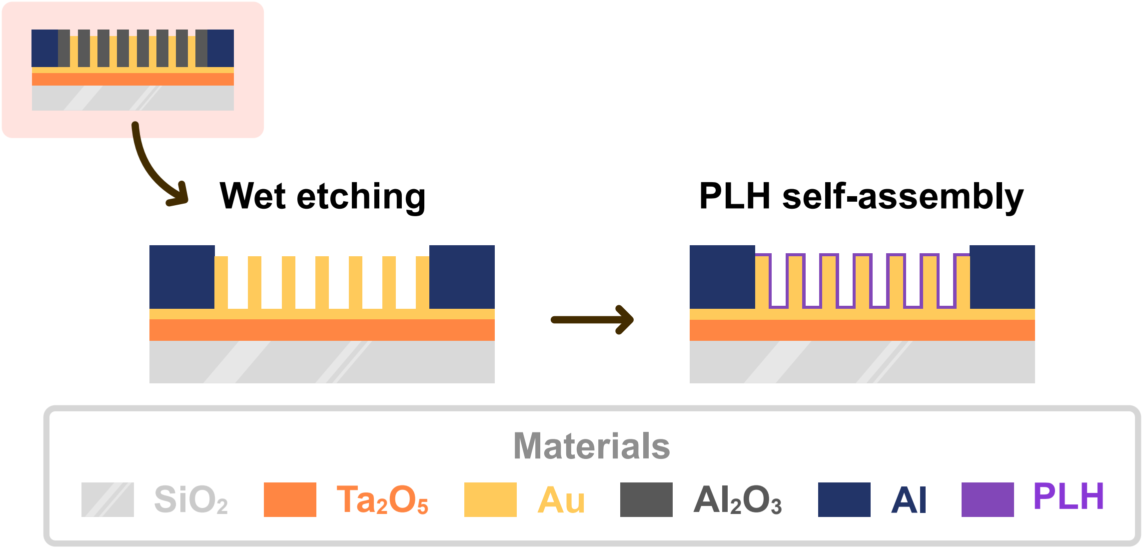

Fig. 3.11 Schematic diagram showing the fabrication of polymer-covering freestanding gold nanorod array.

added to adjust the pH between 5 and 6. Then, the gold nanorod metamaterial was put into the PLH solution and incubated for 0.5 *h*. PLH molecules are expected to be self-assembled on the gold surface due to positive charges, and its imidazole and amino groups have a high affinity to gold. Finally, the metamaterial was rinsed several times with DI water to remove redundant PLH and dried under N_2 for further use.

For the plasmonic tunnelling junction application, this PLH nanoscale spacer works as a tunnel barrier to separate the EGaIn droplet and the gold nanorods and therefore avoid direct contact of these two electrodes that might short-circuit the device. And for the sensing application, this sample is named a PLH-coated gold nanorod array, and this hydrophilic functional layer is expected to improve the sensing performance of gold nanorod metamaterials. The whole treatment to obtain a freestanding gold nanorod array for relative humidity detection is shown in Figure 3.11.

3.3.3 Eutectic Gallium Indium Contact

Figure 3.12 presents a photograph of plasmonic nanorod metamaterials. In this device, the gold nanorod array embedded in the AAO porous matrix is located at the central area of the sample marked with a dashed yellow circle. In contrast, the rest grey area denotes an aluminium layer that is electrically connected to the gold nanorods through the bottom gold substrate and works as the bottom electrode. Considering that the top electrode should be

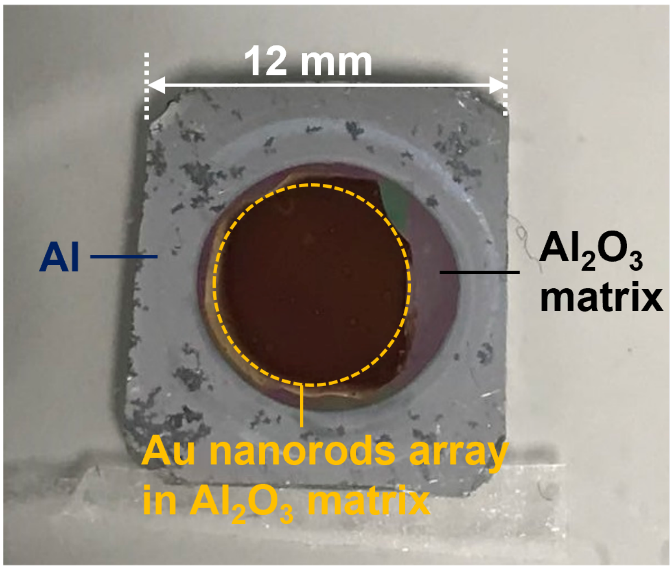

Fig. 3.12 Photograph of a plasmonic nanorod sample.

electrically conductive and at the same time soft enough to avoid destroying the thin tunnel gap, a soft liquid eutectic gallium indium (EGaIn) droplet on the tip of the nanorod is used as the other electrode. While the size of the substrate is around $12 \times 12\ mm^2$, the whole size of the plasmonic tunnel junction directly depends on the contact area of the EGaIn droplet with the gold nanorods, which usually is as large as several square millimetres.

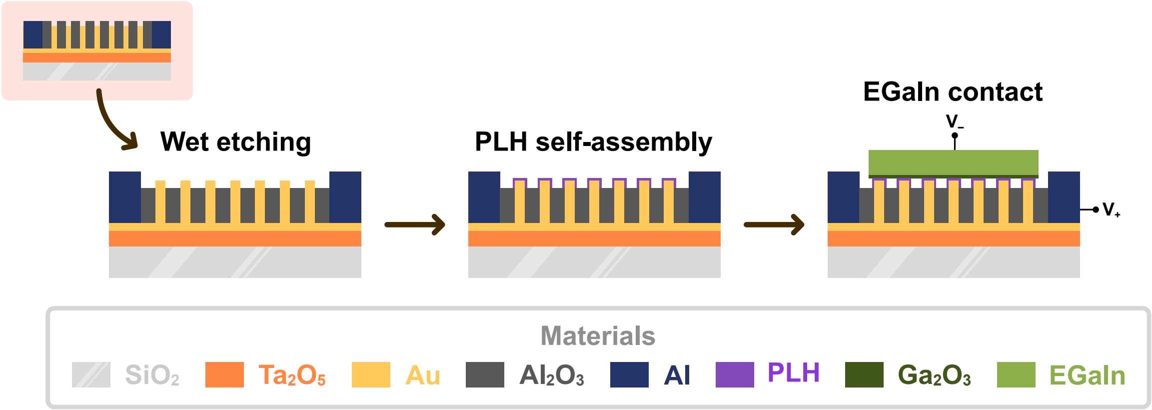

Fig. 3.13 Schematic diagram showing the construction of a nanorod-based plasmonic tunnelling junction.

Figure 3.13 presents the schematic diagram of constructing plasmonic tunnelling junctions. The plasmonic tunnelling junction is based on the gold nanorod array, and a thin layer of polymer works as the tunnel barrier. Liquid metal EGaIn and the bottom gold layer work as two conductive electrodes, respectively. When a bias voltage is applied, electrons tunnel through the thin PLH barriers from the occupied states of EGaIn to unoccupied states in gold nanorod tips, thus forming a basic tunnel junction device.

3.3.4 Formation of Restricted Contact Area

Although the general nanorods-based PTJs have demonstrated their potential as a light source, applying them to practical, real-life usage is challenging. Specifically, considering the huge number of nanorods in this typical PTJs ($\sim 10^{10}\ cm^{-2}$), each nanorod PTJ, as an individual emitting spot, may not respond to the applied bias voltage simultaneously, which could cause the whole device going through a significant time delay when operated at high frequencies. Given the same areal density, the smaller size of the tunnel junction is, the smaller number of nanorods involved, which means the less possibility of delay would be. Hence, it is feasible to address the switch delay problem by reducing the size of the tunnelling junction used for light emission. In addition, to eventually develop the PTJs-based light source with good on/off switch control, as mentioned before, it is of great importance to investigate the optical properties of the whole PTJs-based device at the microscopic scale, which also requires micro-size PTJs.

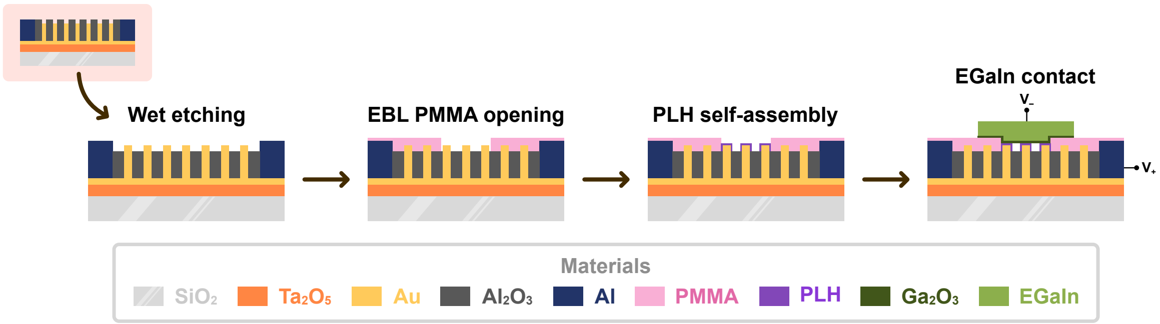

Fig. 3.14 Schematic diagram of micro-scale plasmonic tunnelling junctions with a restricted contact area of EGaIn with gold nanorod metamaterials.

As mentioned in section 3.3.3, the size of PTJs is determined by the contact area between EGaIn and PLH monolayer (thus, gold nanorods), and, for this reason, the micro-scale plasmonic tunnelling junctions (mPTJs) can be easily achieved by designing a micro-scale opening on the metamaterial surface as the only EGaIn-PLH contact area. Figure 3.14 depicts a schematic diagram of a designed nanorod-based mPTJ with a restricted contact area of gold nanorods with EGaIn. In this design, most of the sample surface is covered by insulated poly(methylmethacrylate) (PMMA) layer. At the same time, only a small area of nanorod metamaterials is left uncovered for the subsequent contact of EGaIn. In this way, the size of PTJs is precisely controlled by the size of the uncovered PMMA opening.

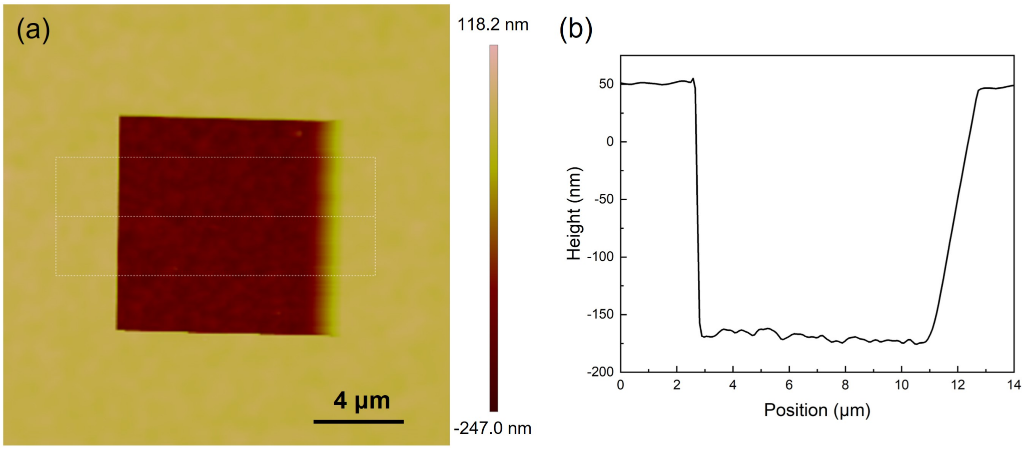

Fig. 3.15 (a) AFM image showing the surface topography of PMMA opening on the plasmonic nanorod metamaterial fabricated using EBL. (b) Cross-section analysis displaying the height profile of PMMA opening.

The fabrication of mPTJs is similar to the construction of PTJs; however, a micrometre-scale open window of PMMA is designed on the freshly wet-etched nanorod metamaterials surface via electron beam lithography before the subsequent construction of tunnelling junctions.

Detailed fabrication steps are as follows: once a gold nanorod array metamaterial is obtained after wet etching (see section 3.3.1), it is then spin-coated with a uniform layer of PMMA solution and subsequently baked at 160°C for 10 *mins* to solidify PMMA. Next, the designed square area is exposed to electron beams and then dissolved in the development solution (Methyl isobutyl ketone (MIBK) and IPA at the ratio of 1:3). Rinsed with IPA and dried with N_2 again, the metamaterial sample with a micro-scale PMMA open window is obtained. The self-assembly of monolayer polymer (section 3.3.2) and the contact of eutectic gallium indium (section 3.3.3) are used to construct a tunnelling junction device.

The geometry of the designed micro-scale PMMA opening can be confirmed with AFM. As shown in Figure 3.15a, the AFM topography displays that a square opening of ($10 \times 10\ \mu m^2$) is successfully formed on the surface of the metamaterial using EBL. And the average thickness of PMMA is measured to be around 200 *nm* as the height analysis shown in Figure 3.15b.

3.4 Characterisation Methods

3.4.1 Experimental Setup for Optical Properties

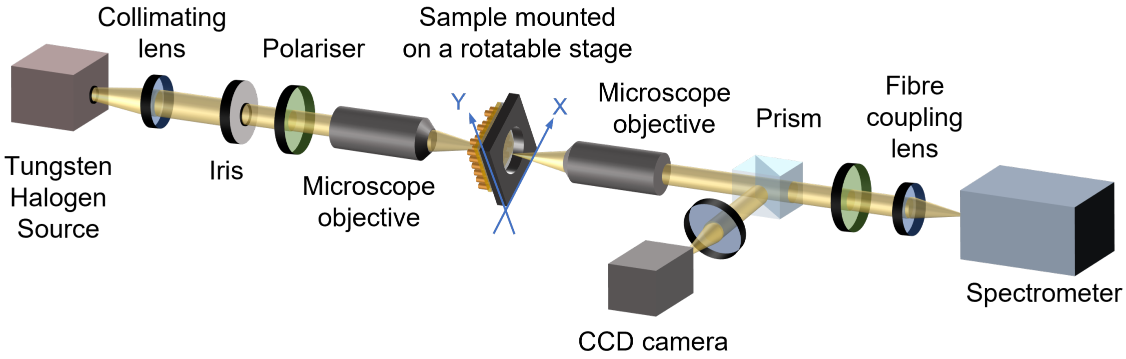

Fig. 3.16 Schematic diagram of the typical optical characterisation setup.

The sample's optical properties are mainly characterised by transmission or extinction spectroscopy. Figure 3.16 depicts the customised setup for the visible transmission spectrum measurements. In this setup, the white incident light generated from a tungsten-halogen lamp is collimated, focused on the sample through a lens, and then collected by a 20× objective lens. The light can be subsequently split by a prism, one part goes to a charge-coupled device (CCD) camera, and the other is directed to a spectrometer (QE Pro, Ocean Optics) via a multi-mode optical fibre. Polarisers and a rotatable sample stage are used to change the polarisation and incident angle of transmission light in the optical path.

Transmission and extinction spectra of a gold nanorod metamaterial for various incident angles were obtained as shown in Figure 3.17. The extinction spectra show a typical mode structure of an array of gold nanorods embedded in an AAO matrix. At normal incidence, one peak at around 550 *nm* wavelength is shown and associated with transverse plasmonic excitation. With the increase of angle incidence, the longitudinal plasmonic excitation gradually becomes more pronounced and overlaps with the transverse mode. The angle-dependent extinction spectra reflect the strong anisotropic structure of nanorods metamaterial.

Notably, thanks to the modularity of the setup, more functions can be flexibly added for the desired measurement purpose. To study the effect of environmental humidity on the optical response of gold nanorod metamaterials, the metamaterials (bare and PLH-functionalized nanorod arrays) were placed in a custom-designed airtight chamber with transparent windows

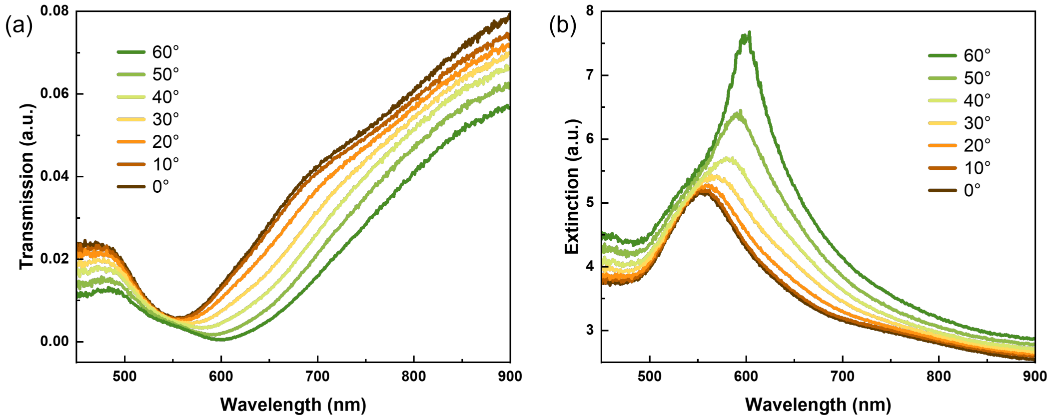

Fig. 3.17 (a) Experimental transmission and (b) extinction spectra of the gold nanorod metamaterial measured with TM-polarised light for different angles of incidence. Extinction here is expressed with transmission T as $-\ln T$.

(Figure 3.18). A nitrogen gas of different humidity (controlled by varying the amount of humid and dry nitrogen in their mixture, monitored by a commercial hygrometer) was introduced into the chamber at a flow rate of about 1 L/min. Collimated transverse magnetic (TM) polarized white light from a tungsten-halogen lamp illuminated the metamaterial at an angle of incidence of 30°, and the transmission was monitored with a spectrometer. All measurements were conducted at room temperature and atmospheric pressure.

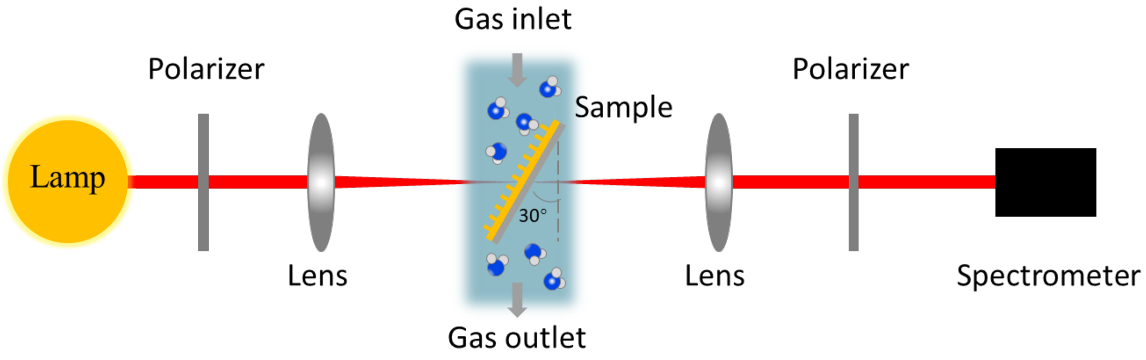

Fig. 3.18 Simplified experimental apparatus used for studying the effect of environmental humidity on the optical response of the gold nanorod metamaterials [134].

Instead, if equipped with an electric source and a detector, this setup can also be adapted to simultaneously study emission spectra and electrical properties of plasmonic tunnelling junctions device.

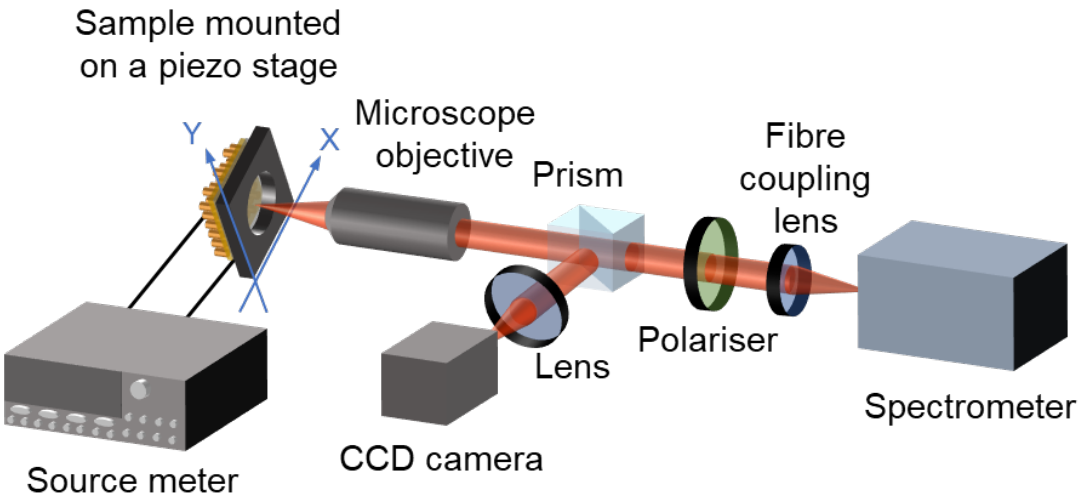

Fig. 3.19 Schematic diagram of the home-built setup for the characterisation of both electrical and optical properties.

Figure 3.19 shows a diagram of the experimental setup. At the beginning of measurements, the optical image of the sample surface is focused on a CCD camera. Once the sample is applied with voltage bias via a source meter, SPP emission is emitted from the glass substrate side of the sample and then passes through an objective and is split into two parts via a prism. A part of the signal goes to a CCD camera to visualise the light emission, while the other part is guided into a spectrometer for visible spectroscopy, thus achieving the simultaneous measurements of both optical imaging and emission spectra. In addition, the prism can be removed or replaced with a mirror to maximise the emission signal for each measurement.

The electrical characterisation of the PTJs is performed via a source meter (Keithley 2611B), and the current-voltage curve measurements are operated by Kickstart IVC software provided by the Rapid Electronics website. Voltage bias is manually varied to record the emission image/video and spectra. To avoid any possible electrical breakdown, the voltage bias is capped at 2.6 V. Besides, a pulse voltage with a period of 20 ms is used to avoid the overheating of the junction.

The optical characterisation for PTJs is based on the optical images/videos and emission spectra. SPPs emission emitted from the glass substrate when the PTJs are biased and is collected by objectives. All the optical images/videos are recorded with a CCD camera with an integration time of 3 s. Regarding spectral measurement, the generated light signal is directed to a multimode optical fibre and finally reaches a spectrometer.

3.4.2 PeakForce TUNA for Current Mapping

Scanning probe microscopy (SPM) is a collection of techniques that produce images by scanning the surface of a sample with a physical probe. Atomic Force Microscopy, as an important member of the SPM family since it was invented in the 1980s, has been widely used in the development of nanoscience for its power in the *in situ* characterisation of topological structures and local physical properties under different operation modes [135]. To understand the electrical properties of the molecule involved surface that traditional conductive AFM can easily damage, Peak-force Tunnelling Atomic Force Microscopy (PeakForce-TUNA) based on PeakForce tapping mode is proposed [136]. Using this technique, the morphology and electrical property of samples can be obtained at the same time [137]. In our experiment, PeakForce-TUNA is used to assess the quality of the fabricated nanorod metamaterials at the nanoscale, where the metallic AFM probe is used for both the topography imaging of as-fabricated structure as well as the measurement of local electrical properties as the top conducting end of PTJs. This section is dedicated to the working principle of PeakForce TUNA.

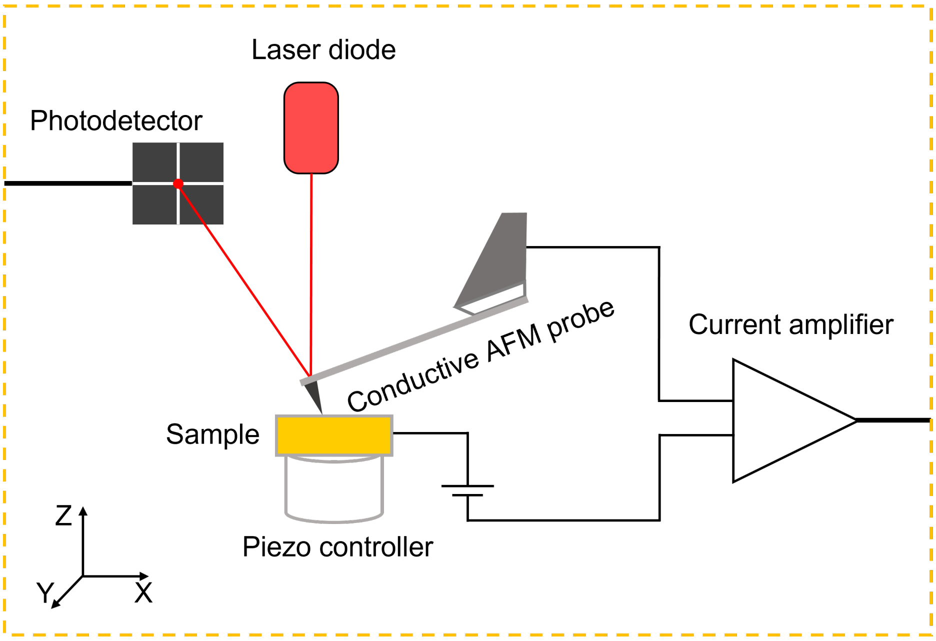

Fig. 3.20 Diagram of PeakForce AFM setup for simultaneous topography, electrical and other property mappings.

A general AFM imaging mode relies on a few basic principles (Figure 3.20). A sharp probe is mounted on a reflective cantilever and scans over the sample surface in a raster pattern. A photodiode beam is focused on the cantilever and reflected onto a four-quadrant photodetector. When the tip moves across the sample surface along the x-y plane, the cantilever deflects first and results in a movement of the beam onto the photodetector. Once receiving the signal change, the feedback controller would adjust the tip position along the z direction to keep tip-sample distance or cantilever deflection constant. This way, a topography image is finally obtained by monitoring the relative change of the cantilever/probe displacement [138]. With the increasing need for property measurements, such as electrical conductivity and surface mechanical properties, the AFM operation modes have been significantly expanded with various additional features.

PeakForce Tapping mode operates similarly to Tapping mode in that it avoids the issue of high lateral forces between the cantilever and surface by contacting the sample intermittently during imaging, and hence shows big advantages in eliminating tip wear and sample damage [136]. However, PeakForce tapping mode differs from tapping mode, for its probe oscillates in a non-resonant mode. Specifically, PeakForce tapping operates at frequencies far below the cantilever resonance range, which allows the control algorithm to respond directly to the probe-sample force interaction. In this way, each probe-sample contact is treated as an independent force spectroscopy experiment, meaning that each force curve can be acquired, analyzed and controlled precisely in real-time during the imaging process.

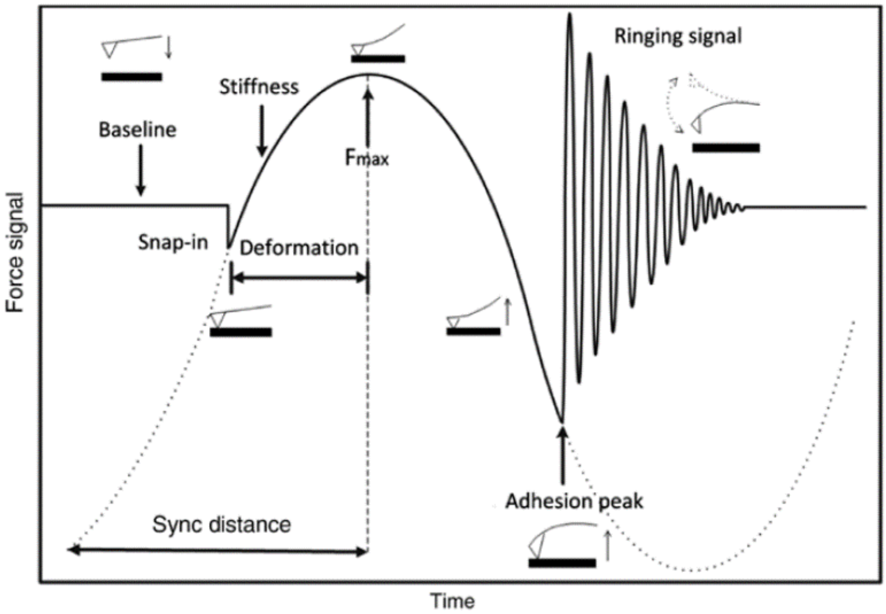

Fig. 3.21 Force curve as a function of time during one PeakForce Tapping cycle [139].

Figure 3.21 illustrates how the force changes when the PeakForce Tapping probe interacts with the surface over time. As the probe approaches the sample surface, it is firstly attracted by long-range force such as Van der Waals force and then suddenly comes into contact with the sample when the attractive force overcomes the cantilever stiffness. After the contact, the short-range repulsive forces dominate the interaction, eventually leading to the peak force. Once the probe starts to withdraw, it experiences an adhesive capillary force until the force reaches the adhesion peak and the tip comes off the surface finally.

Traditional electrical modes operated in other modes, such as tunnelling AFM (TUNA), can get performances significantly improved by combining with PeakForce Tapping. Generally, if working in a tapping mode (>50 kHz), the TUNA module needs to collect current signal very quickly in each cycle to obtain high-resolution current imaging, which theoretically requires an impossibly high modulation bandwidth (~MHz) for the current engineering technology. However, this requiring bandwidth is much lower and hence becomes possible if in combination with PeakForce tapping mode, whose speed is relatively "slow" (1-2 kHz) [140]. Electronic with an attainable high bandwidth (i.e.~15 kHz) is employed in PeakForce TUNA, which efficiently reduces electronic delays for fast data acquisition.

To summarise, PeakForce TUNA mode exhibits superior performance in quantitative mapping and high-resolution current mapping, benefiting from direct real-time force control and avoidance of damaging lateral forces. With the well-controlled and extremely light force during imaging, PeakForce TUNA is capable of providing an unmatched high-resolution current mapping for soft and delicate samples, especially for sensitive self-assembly polymers [141].

Three different currents can be deduced from PeakForce TUNA mode. The peak current is the instantaneous current obtained at peak force, and the contact current is the average current only when the probe is in contact with the sample surface. In contrast, the total current is time-averaged over the full tapping cycle. The contact current is presented in this thesis as the metal coating AFM probe is expected to contact the sample surface to construct a metal-molecule-metal tunnelling junction.

More specifically, this measurement is based on the following assumption: As a constant voltage bias is applied, charged carriers would keep accumulating at the two opposite ends of the metallic probe and the gold nanorod, respectively. When the probe is in contact with the sample surface, the dielectric spacer reaches its minimum thickness. It consists of only the monolayer of PLH, thus forming a pure metal-molecule-metal junction. In this way,

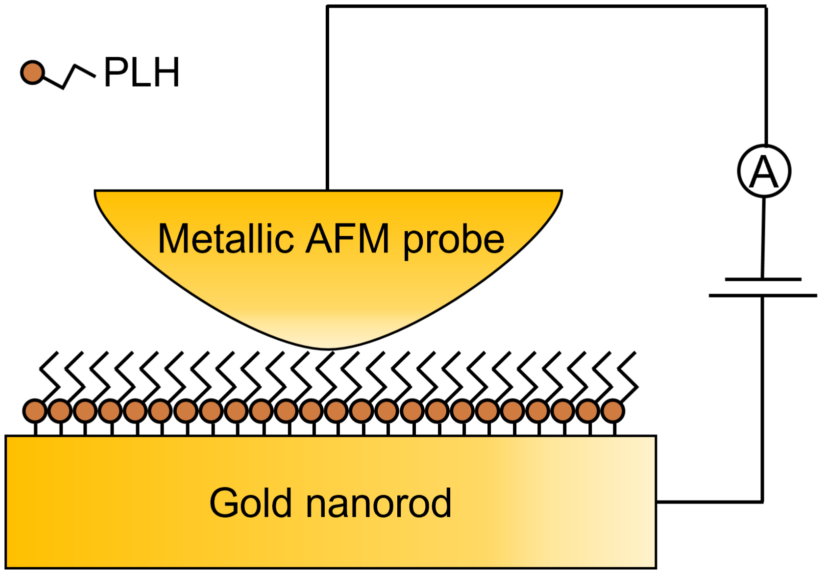

Fig. 3.22 Illustration of the metal-molecule-metal junction using metallic AFM probe as a conducting end.

while mapping the topography of the sample surface, the local current can be simultaneously obtained if electrons tunnel through the junction barrier. The schematic diagram of this junction is illustrated in Figure 3.22.

This measurement was done on a Bruker Dimension Icon atomic force microscope in the ambient condition. The PeakForce TUNA measurement used an SCM-PIT probe (platinum-iridium coating, spring constant ~4 N/m). All images were analysed using the NanoScope Analysis software.

3.5 Numerical Simulations

To study the effect of environmental humidity on the optical response of gold nanorod metamaterials, numerical simulations were performed using the finite element method (COMSOL Multiphysics software). A hexagonal array of gold nanorods was simulated. Using the system's symmetry, a unit cell of the array was modelled with Floquet boundary conditions implementing the appropriate phase shift for the parallel pairs of the side boundaries. The top boundary of the air domain above the metamaterial and the bottom boundary of the substrate domain below the metamaterial was set to have scattering boundary conditions, with the top boundary acting as the source boundary of the incident plane electromagnetic wave. Perfectly matched layers were implemented at the top and bottom of the overall simulation domain to avoid back-reflection. Below the nanorods, 10 *nm* Ta_2O_5 and 7 *nm* Au layers were introduced to represent the structure of the experimental sample. Figure 3.23 shows an example of the structural setting of a unit cell where nanorods are coated with a water layer. The nanorods were modelled as ideal cylinders, with a water layer of thickness from 0 to 0.7 *nm* uniformly covering them and the top of the gold layer below.

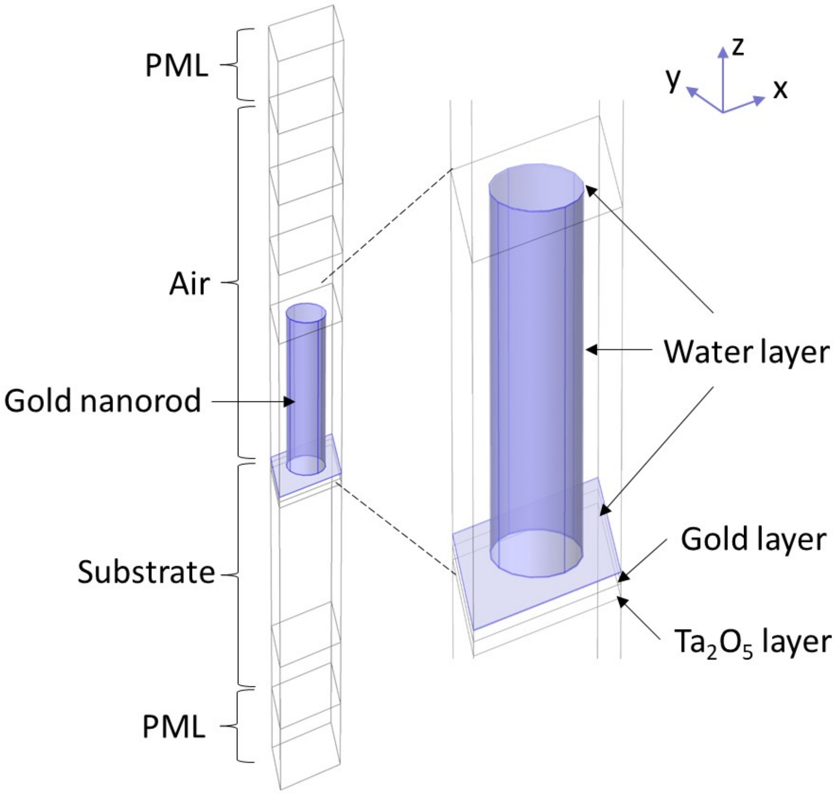

Fig. 3.23 Schematic diagram showing the materials setting of a unit cell of nanorod array coated with a layer of water.

The optical properties of the materials were taken from literature: Au [142], Ta_2O_5 [143], SiO_2 [144]. Additionally, the permittivity of Au in the nanorods was modified to implement a restricted mean free path of the electrons of 3 *nm*, reflecting smaller grain sizes obtained in the electro-deposition fabrication process [145, 45]. The optical properties of nanoscale water have recently been intensively investigated [146]. Theoretical estimations of the optical response of molecular layers of water require first-principle simulations of a particular system in particular conditions. However, continuous refractive index models have also been successfully applied. Following the recent approach [147], a bulk non-dispersive refractive index was used for the water layer, equal to 1.33.

3.6 Conclusions

To summarise, this chapter has focused on the anodic aluminium oxide templates-based patterning technique for the standard fabrication of gold nanorod array metamaterials, and each step has been described in detail. Besides, additional treatments to construct hybrid structures for different applications have also been included. Furthermore, relevant characterisation techniques and numerical simulations for the optical properties of nanorod metamaterials have been presented.

Chapter 4

Humidity-induced Direct Modification of Optical Response of Plasmonic Nanorod Metamaterials

4.1 Introduction

In the past decades, plasmonic metamaterials, artificial optical materials consisting of periodically or randomly arranged plasmonic nanostructures, have been widely investigated since they offer a unique means to engineer optical properties beyond those occurring in nature to achieve exotic optical phenomena, such as magnetism at high frequencies [148] and negative refraction [149, 150]. They have opened up opportunities for numerous applications in nanophotonics, e.g. superlensing [151, 152], optical cloaking [153, 154], gas sensing [155, 156] and nonlinear optics [156, 126]. Among them, plasmonic nanorod metamaterials consisting of arrays of strongly interacting, aligned plasmonic nanorods are particularly interesting. They have been successfully employed for a variety of applications, ranging from imaging beyond the diffraction limit [157], enhancement of optical nonlinearities [158], spontaneous emission control and lasing [130, 159, 160] to biochemical sensing [28, 161], nanoscale optomechanics [162] and tunnelling-based plasmon excitation [125, 163, 164]. Particularly because the optical properties (e.g., extinction, transmission, and reflection spectra) of a plasmonic nanorod metamaterial are determined not only by the plasmonic response of the individual nanorods in the metamaterial but also by the electromagnetic coupling between them, they are extremely sensitive to the refractive index changes in the surrounding dielectric environment. A record-high refractive index sensitivity of ~4×10^4 nm/RIU [28, 165] reveals the nanorod metamaterials as an attractive platform for the development of high-sensitivity optical sensors.

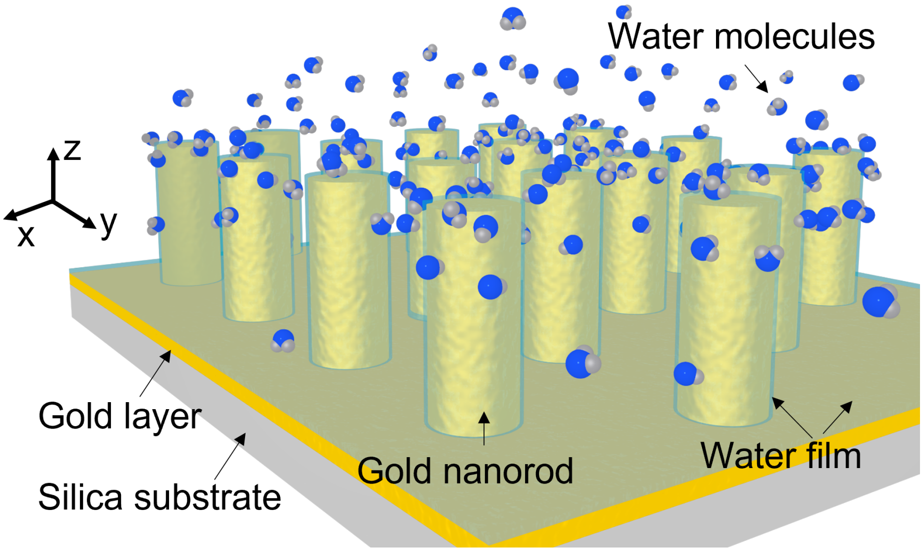

Fig. 4.1 Schematic diagram showing condensation of water molecules onto the surface of freestanding gold nanorods in the metamaterial [134].

In many applications (e.g., gas sensing, linear and nonlinear photonics), nanorods of the metamaterials (bare or functionalized) are directly exposed to an ambient environment, which *a priori* has certain relative humidity (RH). Due to the extremely high sensitivity of nanorod metamaterials to the refractive index of their surroundings, a change in the RH of the environment may cause a direct change in the optical response of the metamaterials and subsequently affect their application performance. Therefore, it is important to reveal the effect of RH of the environment on the optical properties of the nanorod metamaterials, which we demonstrate in this work. We show that a fractional change of up to 5.3% in transmission occurs for a bare gold nanorod metamaterial when it is exposed to an environment with the RH changing from 11% to 75%, which is attributed to the condensation of water molecules on a rough surface of the nanorods (Figure 4.1). This change can get almost doubled if a monolayer of a hydrophilic polymer, such as poly-L-histidine (PLH), is coated onto the nanorods (Figure 4.8), providing an opportunity to develop metamaterial-based humidity sensors.

4.2 Numerical Results of Polymer-coated Gold Nanorod Metamaterials

Simulations have also been done to study the effect of a humid environment on the optical properties of PLH-coated gold nanorods hybrid metamaterial. In this case, instead of forming a water layer, water molecules are assumed to fill the gap between polymer molecules and thus lead to the change of refractive index of PLH from the initial status of 1.565 to 1.7. In addition, the effect of PLH layer thickness and the position of PLH attached to gold nanorods are also investigated.

To study the optical response change of the hybrid PLH-coated gold nanorod with various structures, different positions of PLH attaching on gold nanorods are simulated, including at $1/4$, $1/2$ and $3/4$ top of gold nanorods and also the case where PLH attaching onto the whole nanorod. Figure 4.2a shows the schematic diagrams of different hybrid structures.

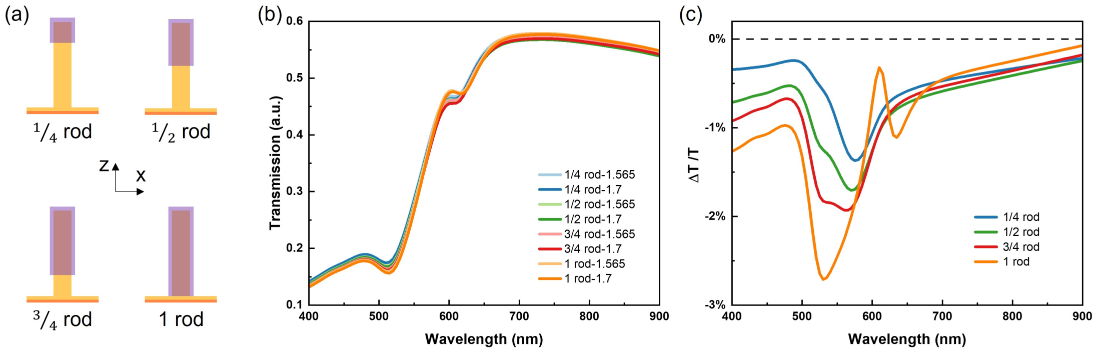

Fig. 4.2 For 1.7 *nm* PLH-coated gold nanorod metamaterial: (a) Schematic diagrams of PLH-coated gold nanorods in various structures. (b) Transmission spectra and (c) the corresponding relative intensity change $\Delta T/T$ when the RI of PLH changes from 1.565 to 1.7.

An average thickness of 1.7 *nm* is used for simulating the monolayer of PLH. Figure 4.2b shows the transmission spectra of corresponding hybrid structures, from which two dips located at two wavelength ranges of $490-530$ *nm* and $590-620$ *nm* are observed, respectively. For the relative change $\Delta T/T$, an overall drop can be observed for all types of structures when the RI of PLH increases from 1.565 to 1.7 (Figure 4.2c). Furthermore, the maximum drop of each transmission spectrum varies as PLH coats more parts of the gold nanorod. When the PLH coats only a quarter top of the nanorod, there is only one main dip of ~1.4% locating at ~575 *nm* as the blue curve shows. With the increasing coverage of PLH on nanorod, the dip goes through both an increase of absolute value and a blue-shit of spectral position, while another dip at a shorter wavelength of 530 *nm* starts to appear and become increasingly obvious. Finally, the two dips merge when PLH coats the whole nanorod, reaching the biggest relative change of ~2.7 at 530 *nm* (orange curve in Figure 4.2c). It is worth noting that the third dip at 635 *nm*, though as small as 1%, appears when the whole nanorod is coated with PLH.

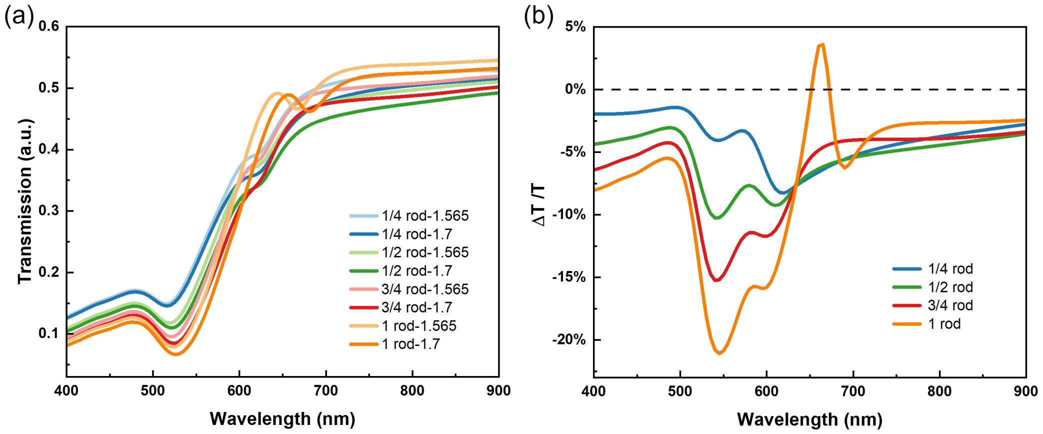

Fig. 4.3 For 10 *nm* PLH-coated gold nanorod metamaterial, (a) Transmission spectra and (b) the corresponding relative intensity change $\Delta T/T$ when the RI of PLH changes from 1.565 to 1.7.

Simulation results show a similar trend of optical properties change When increasing the PLH thickness from 1.7 *nm* to 10 *nm* to simulate the case where a multi-layer PLH coats on the gold nanorod surface. As Figure 4.3 shows, compared with the 1.7 *nm* counterpart, all types of structure with 10 *nm* PLH have almost six times higher intensity change, and all dips locate at a relatively longer wavelength. The dominating dip in the 10 *nm* case is located at 545 *nm*, and the maximum change can reach 21% if PLH fully covers the nanorod.

Other types of hybrid structure, such as 1/2 bottom (PLH coating the half bottom of gold nanorod), also follow a similar trend of optical properties change (Figure 4.4). Specifically, when PLH coats the half bottom of gold nanorods, there is only a dip at a relatively short wavelength at 535 *nm* and 545 *nm* for 1.7 *nm* and 10 *nm* cases, respectively. Compared with when PLH coats the top of the gold nanorod, the dip at a longer wavelength (570 *nm* and 600 *nm*) is no longer observed when PLH coats at the half bottom of the gold nanorod. Interestingly, the third dip that was observed in the fully-coated PLH-nanorods structure also appears in this half-bottom coating case (at around 635 *nm* for 1.7 *nm* PLH and at 700 *nm* for

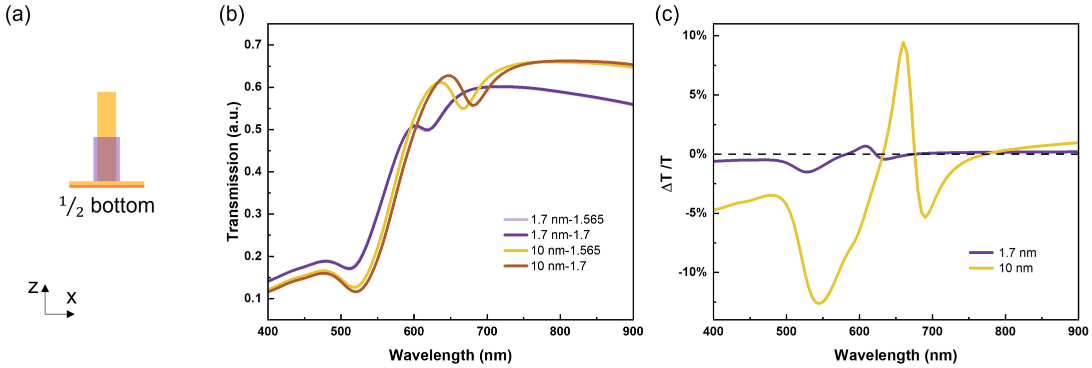

Fig. 4.4 (a) Transmission spectra and (b) the corresponding relative intensity change $\Delta T/T$ of PLH-coated gold nanorod metamaterial when the RI of PLH changes from 1.565 to 1.7. PLH is attached to the half bottom of nanorods and set as 1.7 *nm* and 10 *nm*, respectively.

10 *nm* PLH, respectively), suggesting this transmission dip is associated with the existence of PLH at the quarter bottom of a gold nanorod.

From all the numerical results above, we know that the overall transmission intensity of a PLH-coated nanorod metamaterial would decrease with the increase of PLH RI from 1.565 to 1.7. An increase and a blue shift of the maximum relative change have been observed as increasing the coverage of PLH on gold nanorods. In addition, for all types of PLH-nanorod hybrid structures (e.g., PLH coating $1/4$, $1/2$, $3/4$ and 1 top of rod), when the coating thickness of PLH changes from 1.7 *nm* to 10 *nm*, the mentioned two dominating dips would both redshift from 535 *nm* to ~545 *nm* and from 575 *nm* to ~600 *nm*, respectively, together with an overall increase of relative changes. This phenomenon indicates a possible way to tune the sensitivity of RHs by adjusting the thickness of the PLH layer. What's more, the third dip appears only when PLH coats the quarter bottom part of the gold nanorod (at around 635 *nm* in 1.7 *nm* PLH case and 700 *nm* for 10 *nm* PLH case), suggesting the potential relationship between the relative change and bottom coating structure.

4.3 The Effect of Relative Humidity on Gold Nanorod Metamaterials

4.3.1 Bare Gold Nanorod Metamaterials

The optical response of the bare gold nanorod metamaterials is presented in Figure 4.5a (black curve). The spectrum is dominated by a transmission dip around the wavelength 500 *nm* and

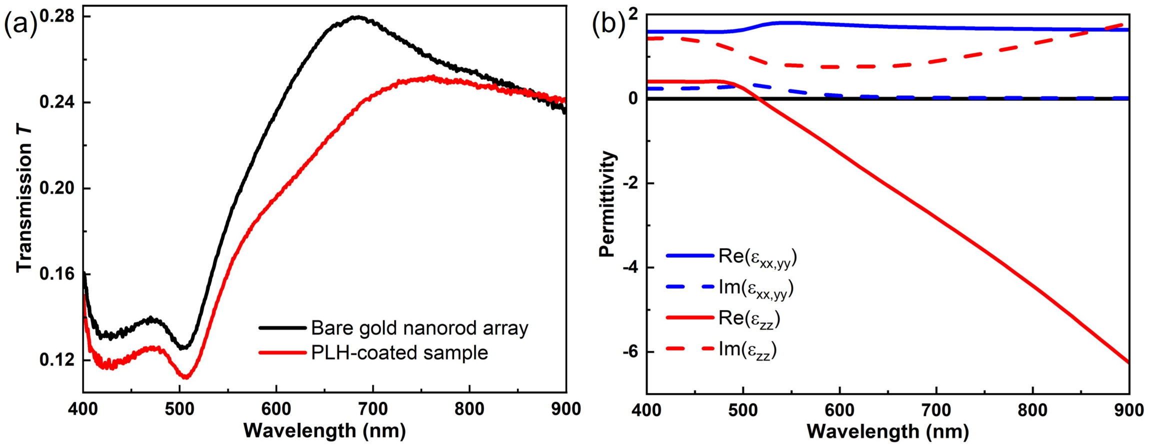

Fig. 4.5 (a) The experimental transmission spectra for bare and PLH-coated metamaterials in a dry nitrogen atmosphere. (b) The spectra of the effective permittivity of the bare metamaterial were calculated using an effective medium theory [166]. The metamaterial parameters are: nanorod diameter 50 *nm*, nanorod length 230 *nm* and inter-rod separation 100 *nm* [134].

a humidity-dependent shoulder at around 650 *nm*. The dip corresponds to the excitation of the transverse plasmonic resonance of the coupled nanorods spectrally overlapping with an ENZ wavelength region [167]. This can be easily understood by looking at the spectral dependence of the effective permittivity of the metamaterial (Figure 4.5b). The transverse resonance corresponds to the peak of the imaginary part of the transverse permittivity components $\mathrm{I_m}(\varepsilon_{xx,yy})$ and, for these nanorod parameters, spectrally overlaps the metamaterial opacity region at the ENZ condition at the wavelength slightly above 500 *nm*. Overall, this produces a combined transmission dip at the spectral position, which is in excellent agreement with the experiments. The shoulder in a $600-650$ *nm* spectral region appearing in humidity measurements (Figure 4.6a) is related to the excitation of a Fabry-Perot (FP) mode supported by the metamaterial slab [166]. The presence of the FP mode was additionally confirmed with a matching dip in the reflection spectrum. After the PLH coating, there is an appreciable difference in the optical transmission compared to the bare nanorod metamaterial due to the high sensitivity of the nanorod metamaterial to the refractive index changes (Figure 4.5a).

The optical response of the bare gold nanorod metamaterial to the environmental humidity was investigated. With the increase of RH, an obvious change in the optical transmission spectra is observed, predominantly in a wavelength range of $600-700$ *nm* (Figure 4.6a). This is highlighted by plotting a relative change $\Delta T/T$ (Figure 4.6b), from where one can see an overall drop across the entire measured spectral range as RH increases, with the maximum drop at around 610 *nm* (5.3% under RH of 75%). This spectral position is close to that of the

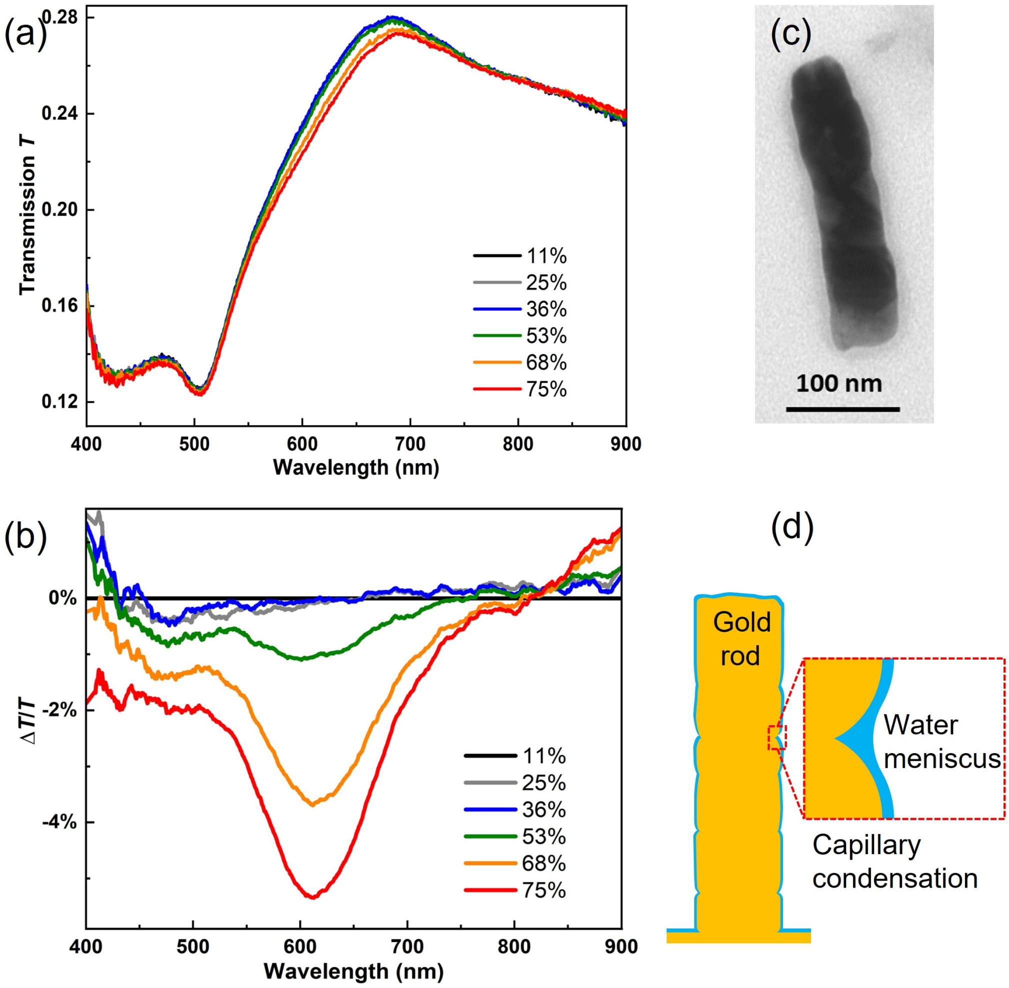

Fig. 4.6 (a) Transmission spectra measured at a 30° angle of incidence and (b) corresponding relative intensity change $\Delta T/T$ when the bare gold nanorod metamaterial is exposed to various levels of RH (11–75%). (c) TEM image of a single gold nanorod (after detachment from the array) showing the rough surface of the nanorods. (d) Schematic diagram of capillary condensation at the rough surface [134].

FP mode of the sample, which has been demonstrated to be extremely sensitive to refractive index changes in the surrounding dielectric environment of the nanorods [73, 28].

Since the change in the refractive index of air with varied RH is very small (4.2×10^{-7} for an RH change from 0 to 50% [168]), the obvious change in the transmission is not likely caused by the change in the refractive index of the surrounding humid nitrogen gas. Also, because the experiment was conducted at room temperature (25°C) and the highest RH was less than 80%, the nanorod metamaterial was operated above the dew point (24°C) and, therefore, there is no macroscopic dew formed on the nanorod array. The obvious change in the transmission of the bare nanorod metamaterial with increasing RH is mainly due to nanoscale water condensation on the rough surface of the polycrystalline gold nanorods. As indicated by a transmission electron microscopy image of a gold nanorod detached from the metamaterial (Figure 4.6c), the surface of the nanorods is rough, and it has a lot of grooves (with dimensions at a nanometer scale) produced by the gold grains. Therefore, with moisture introduced into the chamber, in addition to the condensation of water on the smooth surface of the grains, capillary water condensation (Figure 4.6d) in the grooves forms a water meniscus with an increased nonuniform nanoscale thickness [169, 170]. Continuous water layers can also condense at the top of the nanorods and the bottom gold layer.

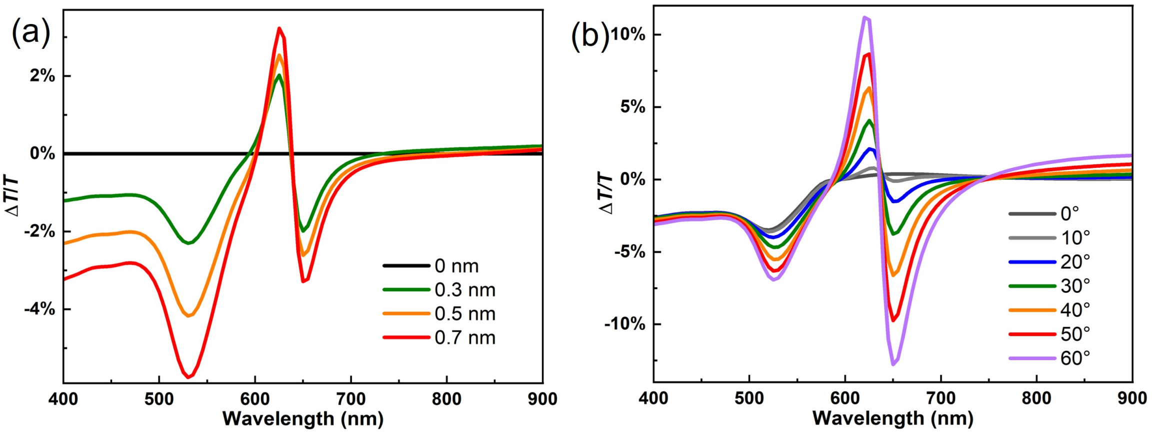

Fig. 4.7 (a) Numerically simulated transmission through the metamaterial with the gold nanorods and bottom gold surface covered with a thin layer of water molecules with a uniform thickness indicated in the legend. (b) Numerically simulated relative transmission change $\Delta T/T$ as a function of the incidence angles (0-60°), when bare gold nanorods are covered with a 0.7 *nm* H_2O layer [134].

To confirm experimental findings, numerical simulations of the system were performed. By using an average water film thickness of 0.3, 0.5, and 0.7 *nm* on each nanorod, two obvious dips around 530 and 650 *nm* can be observed in the spectral dependence of $\Delta T/T$

with the increase of the water film thickness (Figure 4.7a), indicating the high sensitivity of the transmission to the condensation of water molecules. The simulation results show the same general trend in the transmission changes, while the difference with the experimental spectra can be expected due to a much more complex structure of the condensation on the electrodeposited gold nanorods, compared to a uniform layer on the surface of smooth nanorods considered in the numerical simulations. The general trend also shows that the humidity-induced transmission change can increase with the incidence angle (Figure 4.7b).

4.3.2 Polymer-coated Gold Nanorod Metamaterials

For the PLH-coated gold nanorod array, the transmission spectrum shows a similar dependence on the environmental RH changes (Figure 4.8a), but with a larger value of $\Delta T/T$, (9.3% under an RH of 75%; Figure 4.8b). Figure 4.8c further presents the RH-dependent $\Delta T/T$ of the bare and PLH-coated gold nanorod arrays plotted at the wavelength of 613 and 640 *nm*, respectively, with the RH increasing and decreasing from 11 to 75%. For both curves, a little change can be observed in the range of low RH ($11-36\%$) (the slops are 0.002 for the bare and 0.003 for the PLH-coated nanorod metamaterials). For the middle RH region ($36-53\%$), a gradual change (the slops are 0.041 for the bare and 0.086 for the PLH-coated nanorod metamaterials) is present. For the higher humidity values ($53-75\%$), one can see much steeper slopes for all curves: 0.191 for the bare and 0.319 for the PLH-coated nanorod metamaterials, indicating a higher sensitivity response for higher humidity values. Moreover, compared with the bare gold nanorod array (black curve), the PLH-coated counterpart (red curve) shows around a two-fold higher sensitivity, as a steeper slope can be seen across the entire humidity range. This is attributed to the hydrophilic properties of the PLH monolayer deposited onto the nanorod surface, which can absorb more water molecules than the surface of the bare gold nanorods, where water molecules are absorbed only due to condensation. The RH-dependent fractional changes in the transmission, measured under decreasing RHs, agree well with those measured under increasing RHs, indicating the physisorption of water molecules on the metamaterial and good reversibility of the sensor operation.

4.4 Conclusion

This chapter has demonstrated a strong dependence of the optical response of a freestanding gold nanorod metamaterial on the changes in the environmental RH due to the roughness-assisted nanoscale condensation of water on the nanorod surfaces. This reveals the importance of considering the humidity conditions in the optical characterisation of the plasmonic

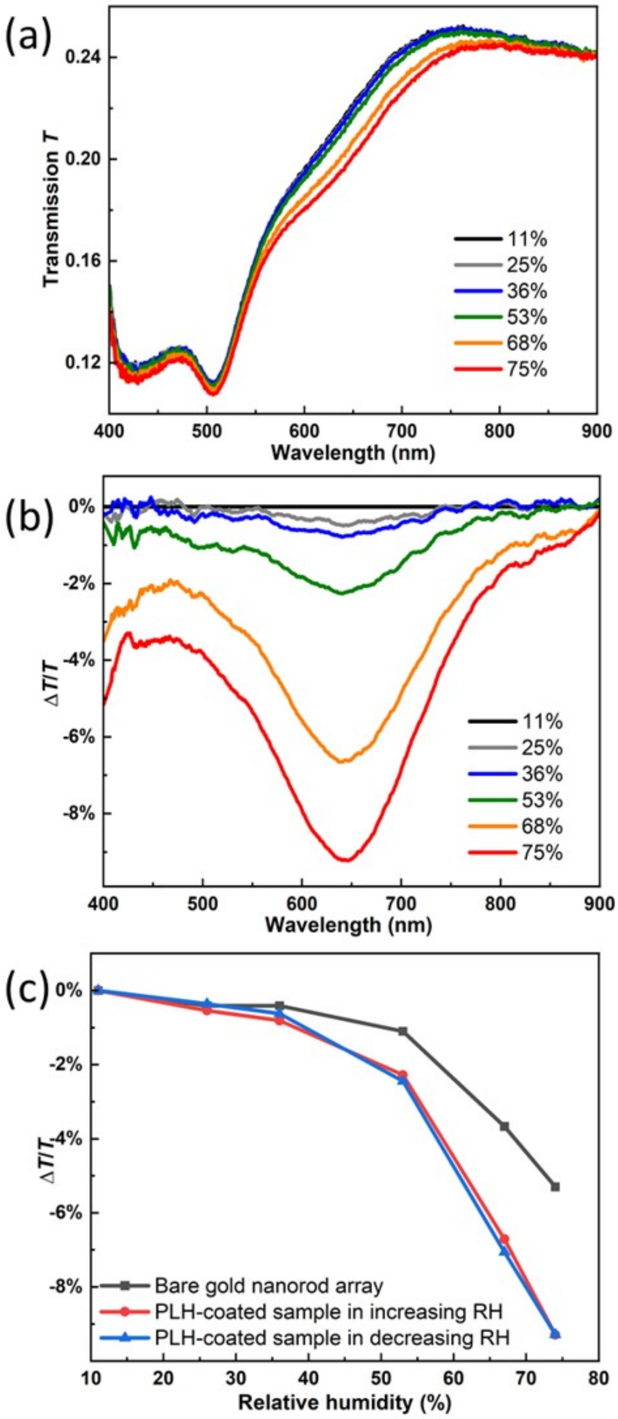

Fig. 4.8 (a) Transmission spectra and (b) the corresponding relative intensity change $\Delta T/T$ when the PLH-coated gold nanorod metamaterial was exposed to nitrogen gas with various RH (11–75%). (c) Comparison of the relative intensity variation $\Delta T/T$ with the change of the environmental humidity measured at 613 and 640 *nm* wavelength for the bare and PLH-coated gold nanorod metamaterials, respectively [134].

nanostructures and, most importantly, their practical applications in sensing. The sensitivity to RH was further improved by functionalising the metamaterial nanorods with a monolayer of hydrophilic PLH polymer promoting the adsorption of water molecules, which provides a perspective for developing such a metamaterial platform for optical humidity sensors. Particularly, the PLH-functionalised nanorod metamaterials have shown almost a 9% change in the transmission with the relative humidity change from 11 to 75%, underlined by the high sensitivity of the excitation of FP modes supported by the metamaterial layer to the changes in the environment.

Chapter 5

Plasmonic Nanorod Metamaterials based Tunnelling Junctions

5.1 Introduction

For SPPs, the sub-wavelength confinement of the electromagnetic field and the rapid decay time (~10 fs) offer exciting possibilities in the realm of optoelectronics by manifesting real promise of reducing the mismatch in length scales of photonic and electronic devices. The benefits of this confinement effect are in a broad spectrum of applications where an enhancement in performance is shown, such as the sensitivity of photodetectors [171], photoluminescence enhancement of quantum emitters [172], refractive index sensing and many others.

However, a limitation for plasmonic-based devices is that they are usually optically driven by a diffraction-limited optical source which inherently limits the device size to be greater than the optical wavelength. In the past, this problem has been attempted to be addressed by using on-chip light emitting diodes (LEDs) to optically excite the SP in the plasmonic device [173]. In essence, electrical excitation is converted to optical emission, which then produces the SP, thus, making this a two-step process and therefore fundamentally slowing it down. A direct electrical excitation based on electron tunnelling effect is therefore very much beneficial [174], with the latter speeds theoretically approaching less than 10 fs, while the former being of the order of 10 ns. Therefore, to achieve true device miniaturization with an ultrafast response, an exciting possibility is the realization of electrically driven plasmonic devices where the SP could be excited, thus removing the need for any bulky light sources. This could be achieved using inelastic electron tunnelling where some tunnelled electrons go towards exciting an SP, which has been shown [175] using a scanning tunnelling microscope

(STM) tip over a gold nanorod where electrons from the tip inelastically tunnel through the gap to enter the gold nanorod and excite surface plasmon polaritons in the nanorod structure as shown in Figure 5.1. The excited SP can further scatter to free space photons, resulting in light emission from the tunnelling junction.

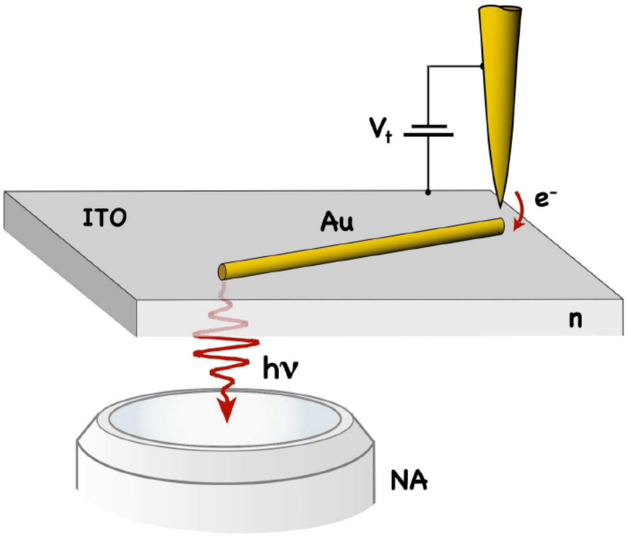

Fig. 5.1 Surface plasmon excitation in gold nanorod by inelastically tunnelled electrons from a scanning tunnelling microscope gold tip [175].

The first direct manifestation of SP excitation by inelastic tunnelled electrons was using a metal-insulator-metal (MIM) junction [176]. As we mentioned, inelastically tunnelled electrons can couple to an SPP mode [177] and therefore eliminate the necessity of a light source for the optical excitation of an SPP. Even though this process is highly inefficient in terms of tunnelling electrons (1 in 10^5 electrons emits a photon, majority of tunnelling electrons follow an elastic route), it is still useful because of its ultrafast response time, which is fundamentally and ideally limited by the tunnelling time for the electron. However, the response time is practically limited by the circuit's RC time constant, which will be further discussed in section 5.4.1.

A very important characteristic of this process is that the tunnelling current density can be highly localized and constrained in nanometer dimensions using metallic nanostructures at the counter electrode and hence can be coupled to SPs. An interesting feature of this plasmonic tunnelling junction is that emission is intrinsically intertwined with surface plasmon excitation. The origin of this emission is the energy transferred from inelastically tunnelled electrons to SPPs which then radiate into photons via an optical antenna. Hence, this process is also called light emission induced by inelastic tunnelling [178, 179].

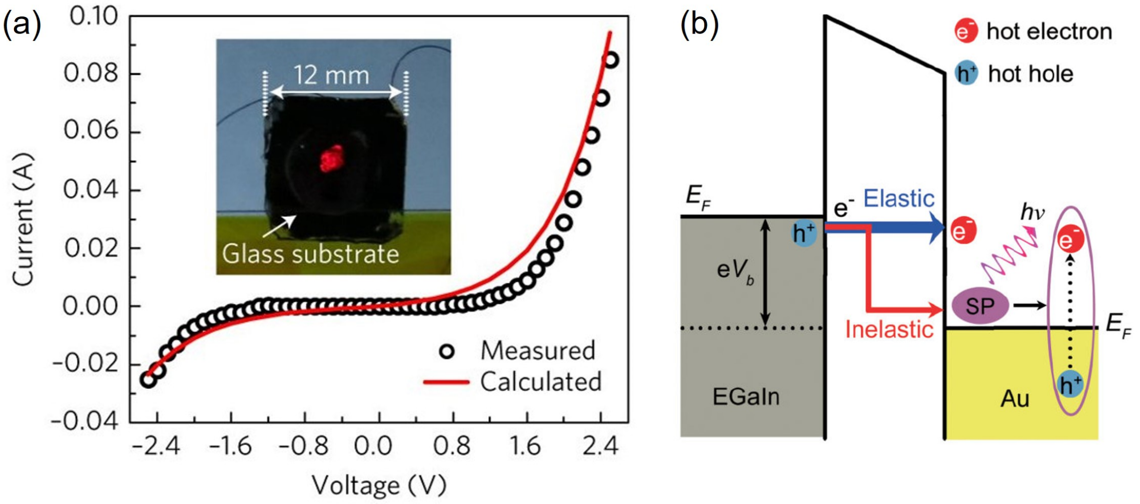

Fig. 5.2 Electrically-driven nanorod metamaterial based on metal-air-metal plasmonic tunnelling junctions [125].

One of the successful implementations of this idea in plasmonic metamaterials employs electrical excitation of SPPs by inelastic tunnelling in the PTJs formed by the nanorods of the hyperbolic metamaterial [125]. The tunnelling process for this device is depicted in Figure 5.2. When a voltage is applied between the liquid metal electrode and gold nanorods, electrons tunnel across the gap from occupied states in liquid metal to unoccupied states in gold nanorods. The majority of electrons tunnel elastically to form hot electrons in the gold nanorod tips; the inelastically tunnelling electrons excite surface plasmons in the metamaterial, which can then decay non-radiatively via the excitation of hot carriers or radiatively into photons from the substrate side of the metamaterial. During the tunnelling process, two plasmonic modes of the metamaterial slab (waveguided and Fabry-Perot modes) are excited by inelastic electrons. Moreover, because the optical spectrum of these metamaterial modes is highly related to the structural parameters of metamaterials which can be engineered during the fabrication process [180], PTJs have the great potential for the design of the emission spectrum in the desired wavelength range by controlling the geometries of metamaterial structures.

In this chapter, nanorods metamaterial-based PTJs are used to obtain an emissive device with a broadband spectral range and tunable emission. The main principle behind this design is integrating a tunnel junction with plasmonic nanostructures, which can generate light emission through the decay of surface plasmons that are excited by inelastic tunnelling electrons. The plasmonic tunnel junction mainly consists of gold nanorods as one conductive electrode, a thin polymer layer as a tunnelling gap and soft liquid metal as another conductive electrode. Moreover, a micro-scale plasmonic tunnel junction is constructed by decreasing the tunnelling junction region using electron beam lithography to achieve more precise control of light emission. These devices' surface topography and structures are characterised by SEM and AFM. Besides, the electrical and optical properties are investigated using current-voltage curves, emission images and spectra and current mapping.

5.2 Plasmonic Tunnelling Junctions

5.2.1 Electrical Characteristics

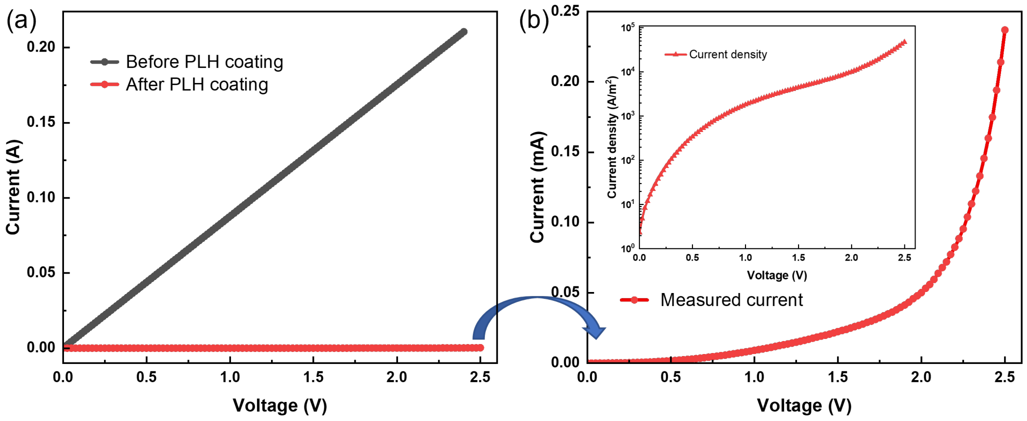

Fig. 5.3 (a) Experimentally measured current-voltage curves for gold nanorod metamaterials before (black curve) and after (red curve) the self-assembly of PLH monolayer. (b) The enlarged current-voltage curve for PTJs showed in (a). Inset: semi-log plot of current density-voltage showing the exponential behaviour.

The current-voltage characteristics are obtained at ambient conditions using the setup mentioned in section 3.4.1. From the two different current-voltage curves in Figure 5.3a, one can observe the electrical properties change after coating a monolayer of PLH. For a freshly etched gold nanorod metamaterial without a PLH monolayer, it shows a linear response of the current-voltage curve when a voltage is applied between EGaIn and Aluminium electrodes, denoting an obvious electrical breakdown (black curve). However, the measured current increases nonlinearly with the increase of voltage bias after coating a monolayer of PLH, as the red curve shows in Figure 5.3b. This typical tunnelling current-voltage curve indicates that electrons tunnel through the PLH barrier between the EGaIn and gold nanorod tips.

The characteristic current density-voltage curve, as the inset shows, also displays the typical exponential dependence, confirming the electron tunnelling characterization of this PTJ.

5.2.2 Optical Characteristics

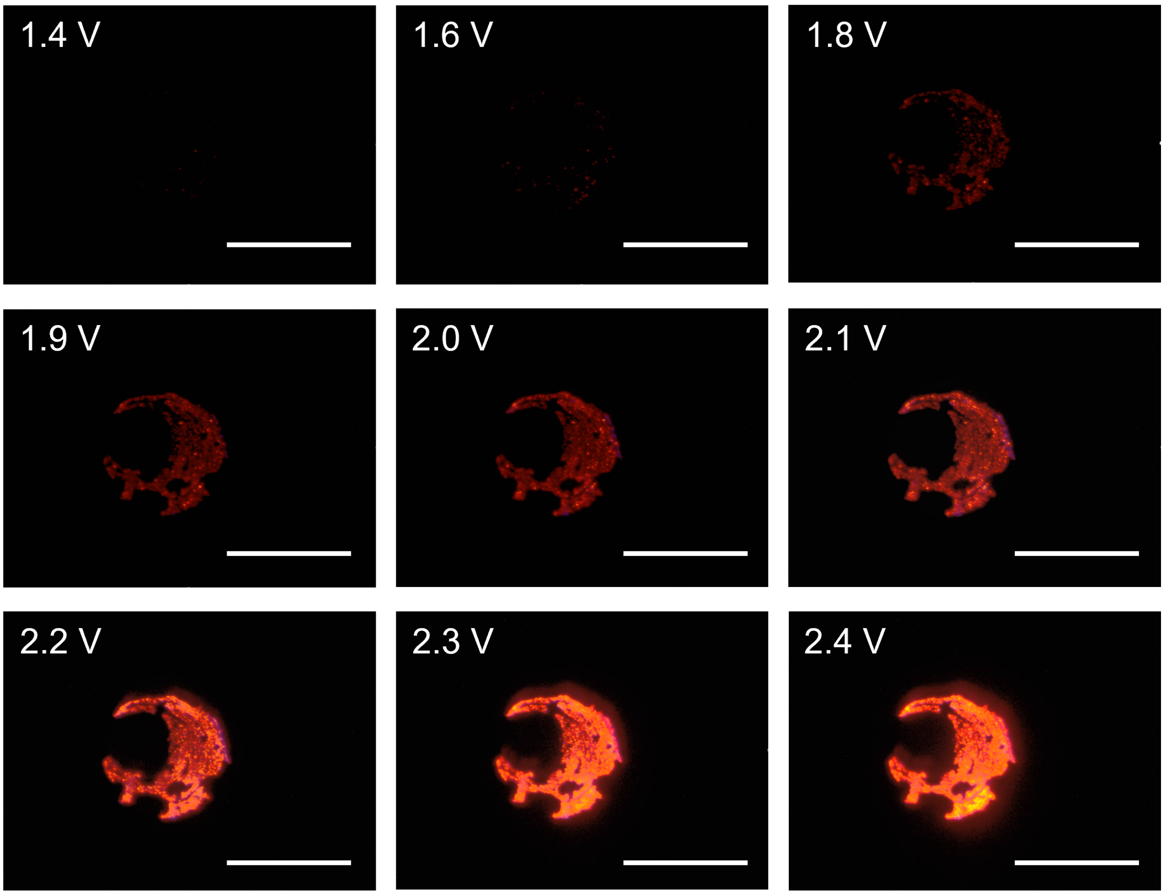

Fig. 5.4 Measured emission of the PTJs under the applied forward voltage bias from 1.4 to 2.4 V. The scale bar of all image is 100 μm and the size of emission area is estimated to 5×10^3 μm^2.

As shown in Figure 5.4, image sequences captured from a video record shows the emitted light of PTJs can be observed via a CCD camera. Under a bias of 1.4 V, the emission intensity is too low to be seen due to the lack of sufficient inelastic tunnelling electrons for excitation. At 1.6 V, some scattering red spots start to be observed as a sign of visible tunnelling-induced light emission. As the applied voltage increases to 1.8 V, more red spots can be seen gradually and a round red emitting area thus forms. As the applied voltage increases, the red-emitting area gets brighter due to the increasing number of electrons tunnelling through the PLH gap and exciting the SPP emission. Finally, when the voltage bias exceeds 2.3 V, the light emission is so strong that the optical image becomes oversaturated. Meanwhile, the colour of the emitting area turns slightly orange, indicating a shift of dominant wavelengths of emission spectra.

It is noted that there are some small round dark areas in the emitting area, which might result from the following two aspects. The first possible reason is related to the metamaterial itself. Surface defects such as contaminants or unfilled gold nanorods in the AAO matrix would hinder the formation of PTJs, and thus, no light emission can be observed from these defective regions. Poor PTJs with big tunnelling gaps may also cause light emission failure. Specifically, when the top EGaIn electrode fails to come into contact close to the PLH monolayer, the dielectric barrier (consisting of both PLH and air) between the two electrodes becomes too big for sufficient electrons to tunnel through and excite photons. This non-uniform emitting problem implies a challenge for the good control of this light switches device with such big-area PTJs.

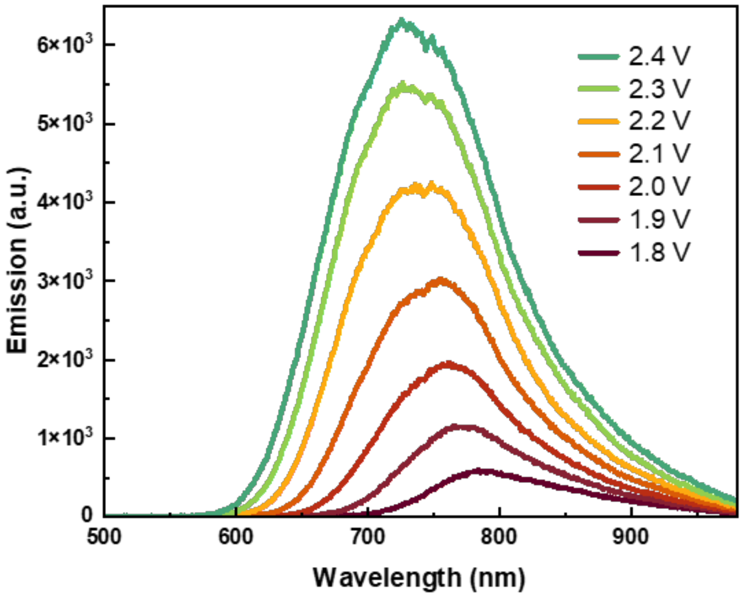

Fig. 5.5 Measured emission spectra of PTJs under the applied forward voltage bias.

To further investigate the optical properties of the PTJs, emission spectra of PTJs measured with increasing voltage bias from 1.8 *V* to 2.4 *V* were obtained, as shown in Figure 5.5. A strong light generation is observed in the visible spectral range of 600 – 900 *nm*. As the applied bias increase gradually, there is a rise in the overall emission intensity together with a blue shift of the emission peak from ~790 *nm* to ~700 *nm*, which is consistent with the emission images shown in Figure 5.4 where the light emission gets brighter and more orange under increasing voltage bias. This voltage-dependence behaviour is associated with the energy transformation within the PTJs, which will be further discussed in the next section.

5.2.3 Voltage Dependence

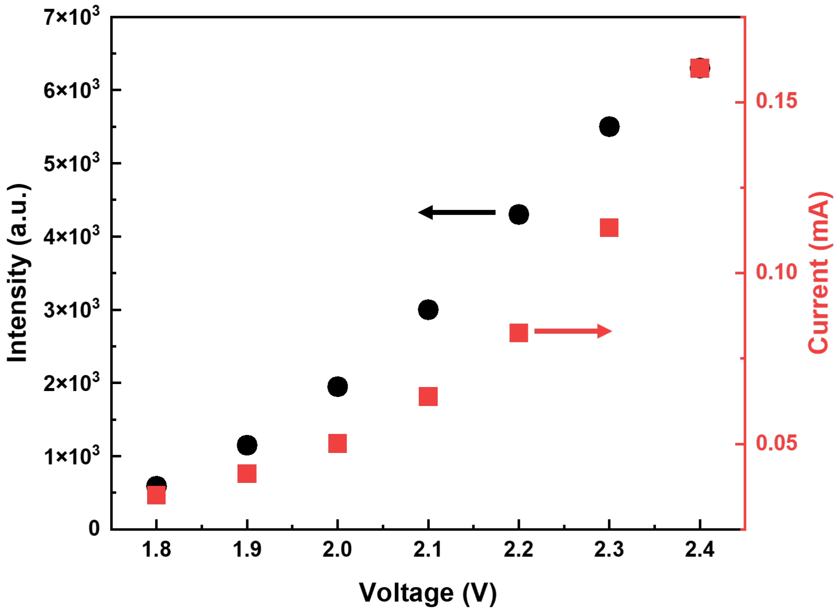

Fig. 5.6 The dependence of emission intensity and tunnelling current on the applied voltage bias.

The light emission resulting from inelastic electron tunnelling can be characterised by a high-frequency cutoff given by

$$\frac{hc}{\lambda_{cutoff}} = |eV_b| \tag{5.1}$$

where hc/λ_{cutoff} is the photon energy, e is the electron charge and V_b the tunnel voltage bias [181]. Figure 5.6 shows that the emission intensity of PTJs (black circles) and the increasing tunnelling current (red squares) both increase non-linearly with the forward applied bias, suggesting a linear relationship between the emission intensity and the tunnelling current.

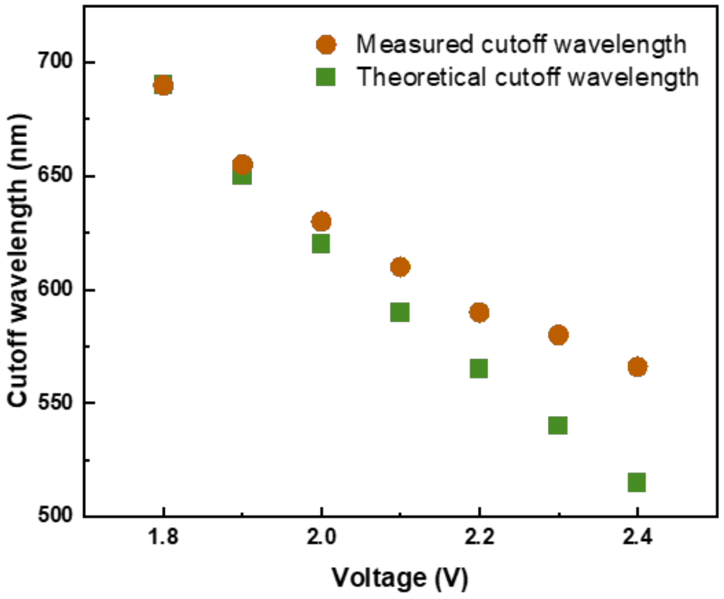

Fig. 5.7 Bias-dependent cutoff wavelength. Comparison of the cutoff wavelength of the spectra in Figure 5.5 (brown circles) and theoretical cutoff wavelength (green squares).

The dependence of the cutoff wavelength on the applied forward bias is presented in Figure 5.7. As we can see, the measured cutoff wavelength is always longer than the theoretically expected value defined by equation 5.1. This is because the energy of the emitted photons is always less than the energy of tunnelling electrons due to energy loss in the electron-photon procedure [181–184]. The emission intensity is relatively low for low biases due to the low photon energy transformed from the tunnelling current near the cutoff. And the emission spectrum shifts to a shorter wavelength as λ_{cutoff} gets smaller under a higher bias. This voltage-dependent characteristic allows tuning emission spectra by varying the applied bias, which also makes PTJ a potential electrically driven light switch in the visible spectral range. In the next section, we will further study the electrical properties of PTJs at a smaller scale using AFM.

5.2.4 Current Mapping

Figure 5.8 presents an electrical current map with the surface topography of nanorods metamaterial simultaneously taken using PeakForce TUNA. A typical topography of nanorods array embedded in AAO matrix can be observed from Figure 5.8a, the average diameter of nanorods is around 55 *nm*. When a +1 *V* bias is applied, nanorods show significantly different

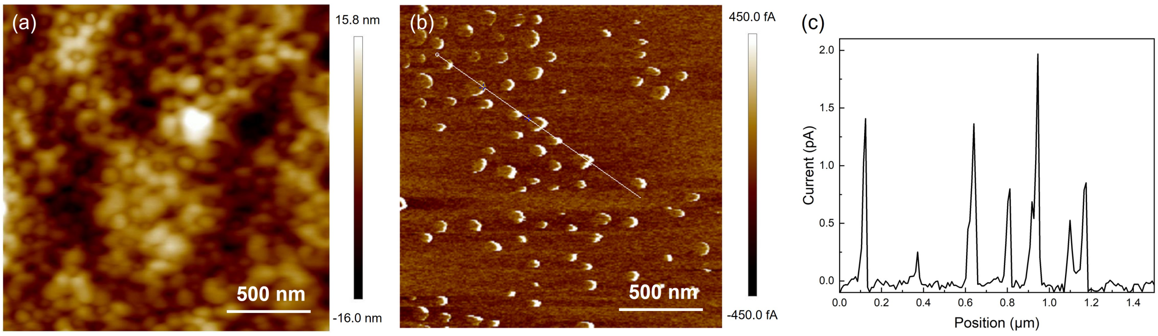

Fig. 5.8 (a) AFM topography image and (b) contact current map of a 2×2 μm^2 nanorods metamaterial sample. The scan was operated at a DC bias of 1 V. (c) Current contour across the line in (b).

current responses from the surrounding alumina. Nanorods presented in the topography image can be clearly distinguished in the current map as obvious current spots. At the same time, the surrounding AAO matrix shows only background current or no current, which can be ignored compared with nanorods current, as shown in Figure 5.8b. Since the PLH layer is inherent insulation, the nanorod current is likely a result of the tunnelling of electrons under applied bias when the soft metallic probe approaches very closely. The current analysis presented in Figure 5.8c shows that the current measured on a single PLH-coated nanorod is within several pA, which is around six orders of magnitude lower than that on the bare gold nanorods [185], and therefore confirms that the current results from the electrons tunnelling. It is worth noting that not all nanorods show current as expected in the current map, which can be interpreted for two possible reasons. One lies in that the force applied on the sample is too small that the probe cannot approach the surface close enough for electrons to tunnel through. This is especially possible when a probe scans over a rough surface, as shown in Figure 5.8a, as no current is shown from nanorods in the "valley" area. The other possibility is related to the poor conduct of nanorods itself to the bottom conductive layer. Defects introduced during fabrication, such as contamination and residual oxide passive particles/layers, could harm the conduction of nanorods during scanning [185].

A similar measurement was conducted at a higher magnification on the same sample using PeakForce TUNA. The result, as shown in Figure 5.9, again presents a clear correlation between the topography and current of individual nanorods, which provides more valuable information for the understanding of local electrical properties of nanorods-based junctions at the nanoscale.

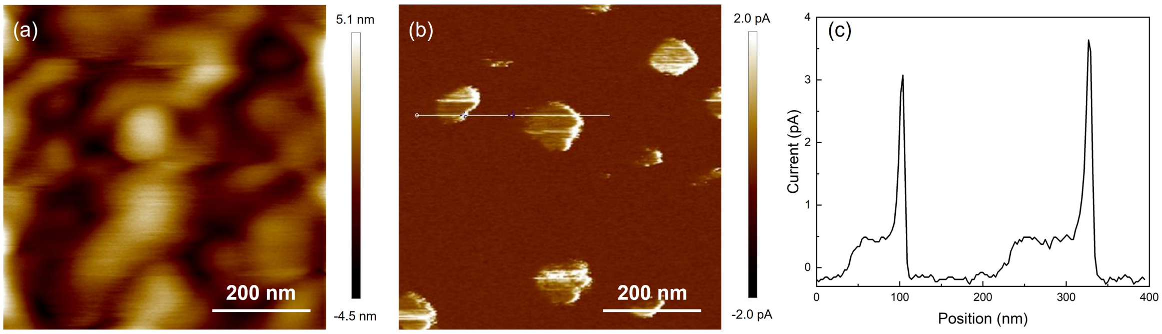

Fig. 5.9 (a) AFM topography image and (b) contact current map of a $0.7 \times 0.7\ \mu m^2$ nanorods metamaterial sample. The scan was operated at a DC bias of $1\ V$. (c) Current contour across the line in (b).

5.3 Metamaterial Modes and tunable Optical Emission

For electrically driven light emission induced by electron tunnelling, the excitation of the metamaterial slab happens when the electrons inelastically tunnel through the dielectric gap and lose their energy to the metamaterial. The excited plasmonic metamaterial mode would then radiate into the substrate, leading to free-space emission. From the principle of light emission excited by tunnelling of electrons, we know that the emission spectrum mainly depends on the inelastic tunnelling rate and the coupling of the metamaterial modes to the free-space radiation. While only the inelastic tunnelling rate is partially determined by the tunnelling current power spectrum, all the other elements highly rely on the metamaterial mode supported by the metamaterial device. Hence, it is important to study the role of metamaterial modes in the overall efficiency of tunnelling-induced light emission devices.

The modal structure of a tunnelling device based on a gold nanorod metamaterial has been investigated both experimentally and numerically. Generally, the plasmonic modes can be told from the emission spectrum and reflectivity, where the emission peaks and reflection dips are in excellent agreement at various angles of incidence. According to the different origins, the excited modes can be classified as either waveguided and Fbry-Perot modes of the metamaterial slab and a localized MIM mode related to the tunnelling gap. As shown in Figure 5.10, the reflection minimum represented with a triangle corresponds to the MIM mode supported by the PLH gap. In contrast, the rest reflection minima denote the different order modes of the metamaterial slab. It is worth mentioning that due to the large spectral widths and the spectral overlap, some modes may have hybrid metamaterial/MIM nature and thus may result in stronger emission intensity at the corresponding spectral ranges. Although the final emission spectra are also affected by their coupling efficiency to the

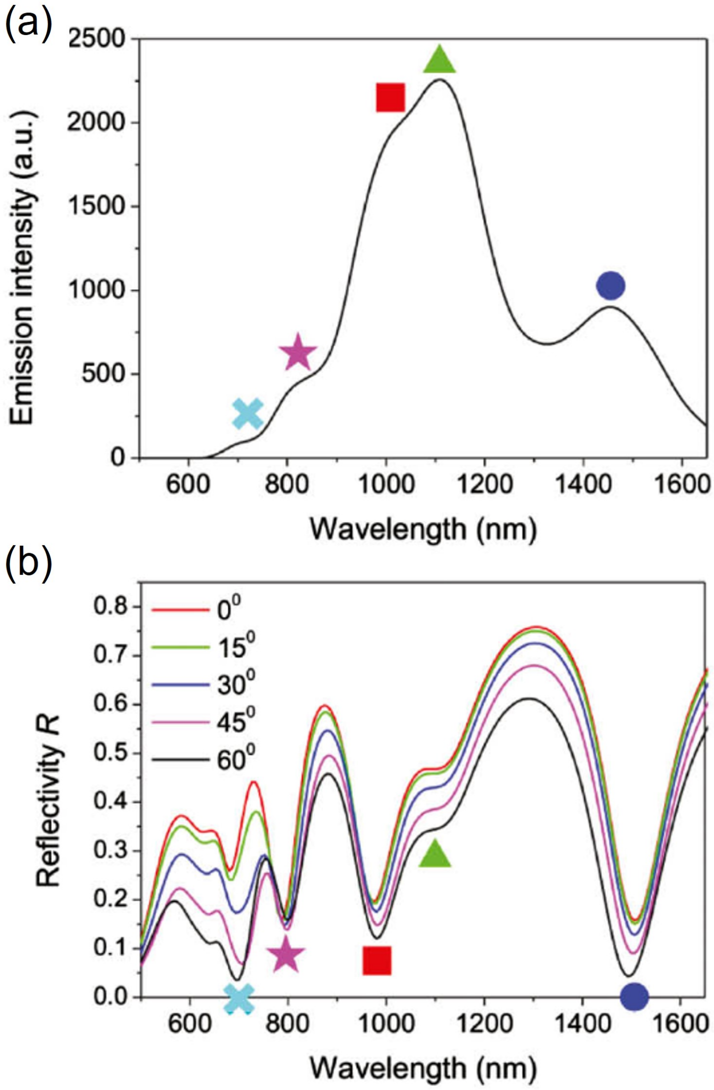

Fig. 5.10 Simulation result for nanorod metamaterial (diameter 71 *nm*, length 500 *nm*, inter-rod separation 96 *nm*): (a) Emission spectrum at a bias of 2.6 V. (b) Attenuated total internal reflection spectra at various angles of incidence of TM-polarized light. The reflection minima correspond to different modes of the device: (circle) second-, (square) third-, (star) fourth-, and (cross) fifth-order modes of the metamaterial slab and (triangle) fundamental MIM mode of the tunnelling gap formed by the nanorod/PLH polymer/EGaIn structure [163].

free-space radiation, there is no doubt that these modes play a crucial part in shaping the tunnelling-induced emission spectrum.

As can be seen from the comparison of the visible light emission spectra in section 5.2.2 and the near-infrared emission spectra obtained with merely different metamaterial geometrical parameters, the gold nanorod metamaterials have presented a flexible platform for the realization of targeted tunnelling emission spectrum by engineering the metamaterial modes via structural parameters. And this is highly feasible in practice since the material component and structural parameters can be controlled in a wide range during the fabrication. In the next section, we will present an attempt to modify the emission spectra of PTJs by varying their structural parameters.

5.4 Micro-scale Plasmonic Tunnelling Junction

5.4.1 Theoretic Foundation

A theoretical prediction is necessary when considering the potential application of PTJs-based switches on fast electro-optical modulation. In our nanorods-array case, each nanorod can be regarded as an individual tunnel junction, an individual RC circuit. The whole PTJ device is thus an ensemble of tunnel junctions in parallel. For each nanorod, its resistance of gold nanorod can be easily calculated with the formula below:

$$R_{rod} = \rho_{Au}\frac{L}{A} \tag{5.2}$$

where R_{rod} is the resistance of individual nanorods, ρ_{Au} is the electrical resistivity of gold material, L and A are the average lengths and cross-sectional area of gold nanorods, respectively. By putting all values into the equation 5.2, $\rho_{Au} = 2.44 \times 10^{-8}\ \Omega \cdot m$ [186], $L = 250\ nm$ and $A = 2 \times 10^{-15}\ m^2$, we then arrive at an estimated value of 3 Ω for R_{rod}.

For a PTJs with size of ~$5 \times 10^3\ \mu m^2$ and nanorod areal density of $1.3 \times 10^{10}\ cm^{-2}$, its total nanorods resistance $\mathrm{R_{allrod}}$ would be then calculated as $R_{allrod} = R_{rod}/N$. N is the number of nanorods involved in the PTJs device whose value can be obtained by multiplying the PTJs area and nanorod areal density, that is 6.5×10^5. We finally get the total nanorods' resistance of $4.6 \times 10^{-6}\ \Omega$. Compared with the resistance of the external circuit (500 Ω), the total resistance of gold nanorods is so small that it can be ignored in the calculation of the total effective resistance of the device.

Generally, a main characteristic of an electro-optical modulator is modulation bandwidth (or the achievable modulation speed) which is determined by the time constant τ (or RC-delay of the component), given by

$$B_{mod} = \frac{1}{\tau} = \frac{1}{R_{eff}C_{eff}} \tag{5.3}$$

where R_{eff} and C_{eff} are this device's effective resistance and capacitance, respectively. According to our previous calculation, the external circuit resistance domains the effective resistance, namely, $R_{\text{eff}} = 500\ \Omega$.

On the other hand, due to the capacitor component of the tunnelling junction, the whole PTJs device could be viewed as a group of capacitors in parallel. Thus the effective capacitance of the device is directly proportional to the number of tunnelling junctions involved in the device, N times the capacitance of the individual gold nanorod C_{rod}. For example, for a PTJs of ~$5 \times 10^3\ \mu m^2$, the effective capacitance is $C_{eff} = NC_{rod} = 6.5 \times 10^5 C_{rod}$.

To increase the electro-optical modulation speed, numerous efforts have been made to improve the tunnel junction structure, such as choosing the electrodes having less electrical resistance and making the tunnelling barrier as small as possible. In nanorods-based PTJ devices, a feasible way to achieve an increased modulation speed is by reducing the size of PTJs. For instance, if the size of PTJs decreases from $5 \times 10^3\ \mu m^2$ to $1 \times 10^2\ \mu m^2$, the number of nanorods involved in the device would decrease 50 times; thus the effective capacitance would increase 50 times correspondingly. The total resistance of gold nanorods would increase 50 times. However, its value is still too low ($2 \times 10^{-4}\ \Omega$) to be taken into consideration, and the effective resistance of the whole device would stay constant. Altogether, the modulation speed would get 50 times higher than its initial value by simply reducing the size of PTJs. Based on this theory, we investigated the properties of micro-scale plasmonic tunnelling junction devices.

5.4.2 Electrical and Optical Characteristics

Once the mPTJs sample is obtained (see the method in section 3.3.4), characterization of its electrical and optical properties is conducted using various techniques.

As shown in Figure 5.11a, a PMMA opening of $10 \times 10\ \mu\text{m}^2$ is observed under a microscope with the help of an external white light source. After removing the external light source and getting EGaIn contact with the PMMA opening, a small red light spot is observed at an applied voltage bias of 2.5 V (Figure 5.11b). Since the red emission spot is at the same

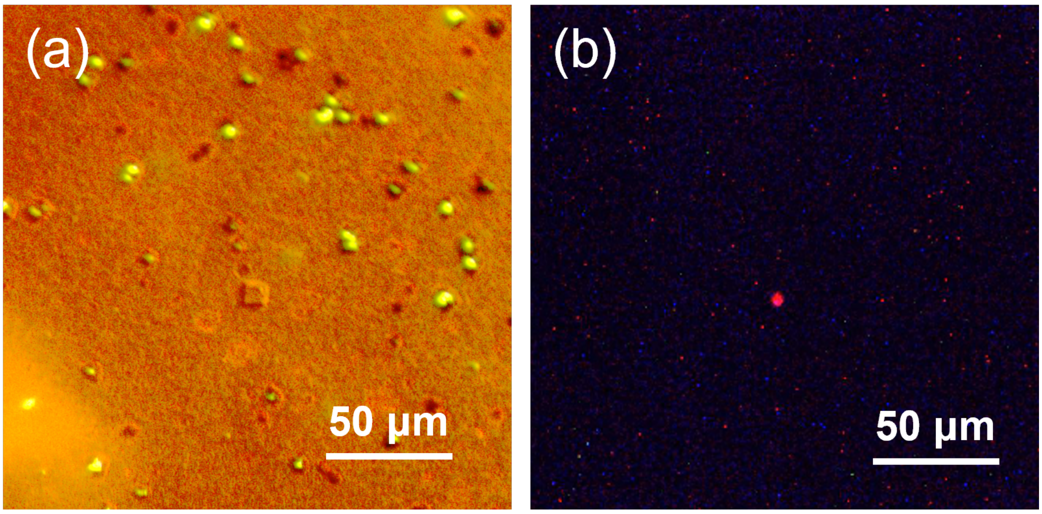

Fig. 5.11 (a) Optical image of a PMMA opening of 10 × 10 μm^2 before EGaIn contact. (b) Measured emission image of the mPTJs in (a) at 2.5 V.

location and size as the PMMA opening, it confirms that the emitting light comes from the mPTJs whose size is restricted by the designed PMMA opening.

Figure 5.12a presents a current-voltage curve of mPTJs obtained at voltage sweep from 0 to 2.5 V, which indicates a typical electron tunnelling behaviour with the nonlinear feature. The spectral characteristic of mPTJs is shown by the emission spectra measured at voltages bias from 2.3 V to 2.5 V with an integration time of 10 s (Figure 5.12b). Since the size of emission area is 100 μm^2, which is about 50 times smaller than that of PTJs sample (~ 5×10^3 μm^2, see section 5.2.2), it is understandable to have much lower tunnelling current and emission intensity on mPTJs. In addition, as shown in Figure 5.12c, due to the energy loss between tunnelling electrons and emitted photons, measured cutoff wavelengths are always longer compared with the theoretical cutoff wavelengths [181, 184], which is in agreement with our previous experimental observations on big-area PTJs (Figure 5.7).

5.4.3 Current Mapping

Similarly to the PeakForce TUNA, conductive Atomic Force Microscopy (CAFM) is also useful to characterise local electrical properties over sample surface [185, 187]. In this measurement, the conductive probe is expected to form mPTJs and measure the corresponding current simultaneously while scanning the PLH-coated nanorods within the PMMA opening. The measurements were performed on a Bruker Dimension Icon atomic force microscope in the air at room temperature. A silicon probe with Pt-Ir coated probe and spring constant

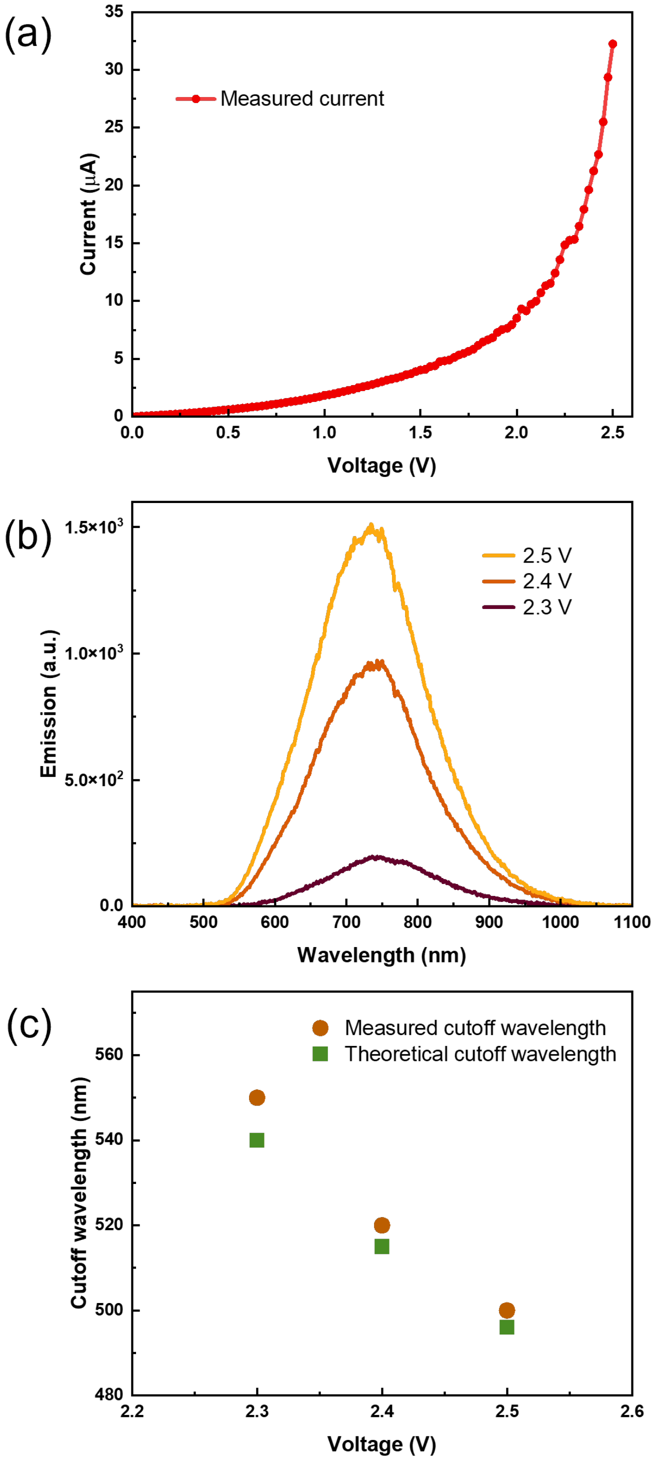

Fig. 5.12 (a) Current-voltage curve of mPTJs under applied voltage bias sweep from 0 to 2.5 V. (b) Measured emission spectra of mPTJs at applied voltages from 2.3 V to 2.5 V. (c) Comparison of cutoff wavelengths in theory and the ones measured from (b).

of ~4 N/m (SCM-PIT) was used. All images were analyzed using the NanoScope Analysis software.

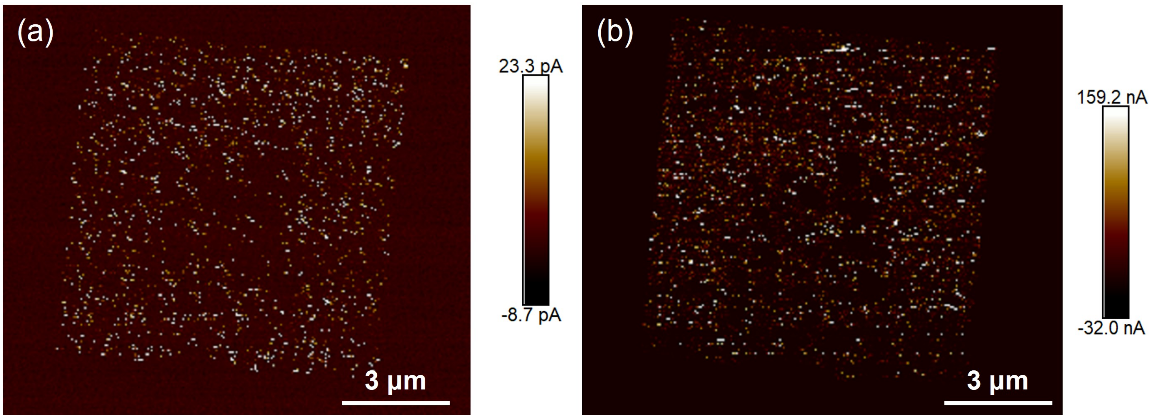

Fig. 5.13 CAFM current maps of a PMMA opening of $10 \times 10\ \mu m^2$. The scanning was operated under applied DC bias of 3 V and 4 V, respectively.

Two current maps of a PMMA opening at DC bias of 3 V and 4 V were obtained and presented in Figure 5.13. Both current maps show that currents are observed only within the opening where no PPMA is coated, while no current appears on the PMMA-coated area. Current spots are well isolated from each other in the current pattern, indicating nanorod distribution within the AAO template. In addition, as the applied bias increases to 4 V, the number of current spots in the opening increases accordingly. At the same time, there is a significant overall increase in current values from picoampere to nanoampere. Altogether, these results exhibit the local electrical characteristics of nanorods in the case where a metal-coated probe works as a conductive electrode of mPTJs. And this measurement can be further improved by performing at a higher magnitude, e.g., on single individual nanorods. And corresponding current-voltage curves would be highly helpful in understanding the underlying principles of electrons moving with this device.

5.5 Conclusion

This chapter has presented plasmonic tunnelling junctions based on nanorod metamaterials. Using EGaIn as a top conduction electrode and a monolayer of PLH as the tunnelling barrier, the PTJs were investigated from the point of view of broadband optical response and tunability. In addition, to reduce the time response of the emission modulation, PTJs with a controlled area to obtain a restricted micro-size EGaIn-contacting area for micro-scale PTJs and single nanorod tunnel junctions were investigated. Such tunnel junction-based light emitting devices may have significant potential for nanoscale light sources in integrated nanophotonics and sensing applications.

Chapter 6

Conclusion & Outlook

6.1 Conclusion

This thesis investigates the potential of gold nanorods arrays hybridised with molecular species as a plasmonic nanorods metamaterial. The underlying motivation is to realize hybrid plasmonic structures by combining nanorod arrays with molecules, aiming to exploit the resulting optical properties for the fields related to sensing and light emission.

Firstly, we have explored both experimentally and theoretically, the sensitivity of plasmonic nanorod metamaterial to the relative humidity in the environment. This is an important topic as plasmonic sensors and devices often operate in the ambient environment and, therefore, are subject to humidity variations. The optical response of a freestanding gold nanorod metamaterial is highly dependent on the changes in the environmental RH, which can be interpreted by the roughness-assisted nanoscale condensation of water on the metal surfaces. With potential humidity sensing applications in mind, we have further improved the sensitivity to RH by functionalising the metamaterial nanorods with a monolayer of hydrophilic PLH polymer, promoting the adsorption of water molecules. Quantitatively, the PLH-functionalised nanorod metamaterials have shown a ~9% change in the transmission when the relative humidity varies from 11 to 75%. This performance is due to the high sensitivity of the excitation of FP modes supported by the metamaterial layer to the permittivity change of the environment. More generally, this experiment reveals the importance of considering the humidity conditions in the optical characterisation of the plasmonic nanostructures and, most importantly, their practical applications in gas sensing. At the same time, it opens a prospect for developing such metamaterial platforms for optical humidity sensors.

A broadband and tuneable electrically-driven plasmonic light source was demonstrated with nanorod metamaterials-based tunnelling junctions. The construction of a plasmonic tunnelling junction was achieved using metal-polymer-metal junctions, in which EGaIn and gold nanorods work as the top and bottom conductive electrodes, respectively, and a monolayer of PLH is used as the tunnelling barrier. The electrical and optical properties of PTJs have been explored with various characterisation techniques, including current-voltage curves, emission spectra, optical imaging and current mapping. These experimental results are of great importance because they have provided valuable information for understanding how to control plasmonic inelastic electron tunnelling and related emission. How fast one can modulate emission by changing an applied bias is important for modern nanophotonic applications. To circumvent the RC time delay accompanying a large-scale emitting area, a concept of mPTJs is proposed. It allows better control of light switching at the nanoscale with fewer tunnelling junctions involved in the emission and, thus, smaller RC values. A simple approach is to intentionally restrict the size of the electric contact area to form mPTJs. This has been realized by designing a PMMA opening of $10 \times 10\ \mu m^2$ on gold nanorods metamaterial via EBL. Preliminary experimental results demonstrated the feasibility of this concept, raising the prospect of a well-controlled localized electrically-driven light source.

6.2 Outlook

The work presented in the current thesis has uncovered many aspects needed to be investigated further and left much space for future work and analysis. The experimental results have demonstrated the capability of plasmonic nanorod metamaterials, with the design of hybrid structures, to be used in many practical applications ranging from sensing platforms to visible and IR light emitters. As an extension to the humidity sensing achieved with the PLH-coated freestanding nanorods metamaterial, the sensitivity to the relative humidity in the environment could be beneficial from optimising the polymer. To name only a few, increasing the thickness of the polymer layer as much as possible and wisely choosing alternative types of hydrophilic polymer. Moreover, with the geometry-dependent optical properties, further nano-structuring of the nanorod metamaterials can be used as a way to optimise further the performance in gas/molecules monitoring and development of freestanding humidity sensors, which can be interrogated remotely by a laser beam.

We have fabricated plasmonic tunnelling junctions based on nanorod metamaterials and uncovered their electric and optical behaviour. More investigations based on our preliminary experimental results will benefit current-voltage characteristics and light emission from single individual gold nanorods to understand further the limits of the nanoscale tunnel junctions in light emission and the potential for their applications. One can optimize the design of a PTJ structure for a wider use of the type of electrically driven light emitter. For instance, a feasible way to realise both-sided light sources is to consider using an alternative transparent top electrical contact, such as ITO and graphene [188, 189]. Lastly, while focusing on the light emission in the visible spectral domain, it also deserves some attention to employ PTJs in the (near-)infrared and terahertz spectral range [189, 163, 190].

On a wider scope of antenna-coupled tunnel junctions, an overall low external device efficiency of photons per electron ($10^{-7}-10^{-3}$) remains a big challenge [184], although tremendous effort has been made. In principle, the overall efficiency depends on two factors. One is the probability of inelastic electron tunnelling that is mainly determined by the local density of optical state enhancement, and the other one is antenna radiative efficiency defined by the ratio of propagating photon radiation to the plasmonic modes excited by inelastic tunnelling electrons. Hence, feasible strategies for these two aspects should be considered to enhance the overall device efficiency. For example, the propagation losses can be minimized by optimizing the geometry of plasmonic tunnelling junctions, including shortening the tunnelling gap and gold nanorods as much as possible. Moreover, one can increase emission efficiency by suppressing elastic tunnelling or promoting inelastic tunnelling. Alternatively, one can instead take advantage of the numerous hot electrons accompanied with elastic tunnelling to explore new potential applications [164, 167], such as integrated optical and electrical sensor, activation of chemical reaction and detector of in situ chemical transformation of molecules, and many other applications in active nanophotonics.

List of Publications

Journal Papers

- **Y. Jiang**, A. V Krasavin, M. E. Nasir, P. Wang, and A. V Zayats, "Humidity-induced direct modification of the optical response of plasmonic nanorod metamaterials," *Opt. Mater. Express* 12(12), 4574–4581 (2022).
- B. Zhou, **Y. Jiang**, Q. Guo, A. Das, A. B. J. Sobrido, K. A. Hing, A. V Zayats, and S. Krause, "Photoelectrochemical detection of calcium ions based on hematite nanorod sensors," *ACS Appl. Nano Mater.* 5(11), 17087–17094 (2022).
- P. Wang, A. V Krasavin, L. Liu, **Y. Jiang**, Z. Li, X. Guo, L. Tong, and A. V Zayats, "Molecular plasmonics with metamaterials," *Chem. Rev.* 122(19), 15031–15081 (2022).
- A. V. Krasavin, P. Wang, M. E. Nasir, **Y. Jiang**, and A. V. Zayats, "Tunneling-induced broadband and tunable optical emission from plasmonic nanorod metamaterials," *Nanophotonics* 9(2), 427–434 (2020).
- P. Wang, M. E. Nasir, A. V. Krasavin, W. Dickson, **Y. Jiang**, and A. V. Zayats, "Plasmonic metamaterials for nanochemistry and sensing," *Acc. Chem. Res.* 52(11), 3018–3028 (2019).

Conference Paper

- A. V. Krasavin, **Y. Jiang**, P. Wang, M. E. Nasir, A. V. Zayats, "Hot-electron effects in electrically-driven plasmonic nanostructures: light, sensing and artificial synapses", *keynote talk at the Materials Research Meeting* (Yokohama, Japan, 2019)

References

[1] David AB Miller. Device requirements for optical interconnects to silicon chips. *Proceedings of the IEEE*, 97(7):1166–1185, 2009.

[2] Ekmel Ozbay. Plasmonics: Merging photonics and electronics at nanoscale dimensions. *Science*, 311(5758):189–193, 2006.

[3] Hans J Queisser. Photovoltaic conversion at reduced dimensions. *Physica E: Low-dimensional Systems and Nanostructures*, 14(1):1–10, 2002.

[4] Lindsay C Botten, M Cadilhac, GH Derrick, D Maystre, RC McPhedran, M Nevière, and P Vincent. *Electromagnetic theory of gratings*. Springer Science & Business Media, 2013.

[5] Martin Dressel and George Grüner. *Electrodynamics of solids: Optical properties of electrons in matter*. Cambridge University Press, 2002.

[6] Neil W Ashcroft and N David Cornell. *Solid state physics*. Thomson Press, 2003.

[7] Mark Fox. *Optical properties of solids*. Cambridge University Press, 2010.

[8] William L Barnes, Alain Dereux, and Thomas W Ebbesen. Surface plasmon subwavelength optics. *Nature*, 424(6950):824–830, 2003.

[9] Stefan A. Maier. *Plasmonics: Fundamentals and applications*. Springer, 2007.

[10] Heinz Raether. *Surface plasmons on smooth and rough surfaces and on gratings*. Springer Berlin Heidelberg, 1988.

[11] Anatoly V Zayats and Igor I Smolyaninov. Near-field photonics: surface plasmon polaritons and localized surface plasmons. *Journal of Optics A: Pure and Applied Optics*, 5(4):S16–S50, 2003.

[12] Jack J Mock, Mladen Barbic, David R Smith, D A Schultz, and Sheldon Schultz. Shape effects in plasmon resonance of individual colloidal silver nanoparticles. *The Journal of Chemical Physics*, 116(15):6755–6759, 2002.

[13] Matthew Rycenga, Claire M Cobley, Jie Zeng, Weiyang Li, Christine H Moran, Qiang Zhang, Dong Qin, and Younan Xia. Controlling the synthesis and assembly of silver nanostructures for plasmonic applications. *Chemical Reviews*, 111(6):3669–3712, 2011.

[14] Emiliano Cortés, Fedja J Wendisch, Luca Sortino, Andrea Mancini, Simone Ezendam, Seryio Saris, Leonardo de S. Menezes, Andreas Tittl, Haoran Ren, and Stefan A Maier. Optical metasurfaces for energy conversion. *Chemical Reviews*, 122(19):15082–15176, 2022.

[15] Carsten Sönnichsen, Björn M Reinhard, Jan Liphardt, and A Paul Alivisatos. A molecular ruler based on plasmon coupling of single gold and silver nanoparticles. *Nature Biotechnology*, 23(6):741–745, 2005.

[16] Xiaohua Huang, Ivan H El-Sayed, Wei Qian, and Mostafa A El-Sayed. Cancer cell imaging and photothermal therapy in the near-infrared region by using gold nanorods. *Journal of the American Chemical Society*, 128(6):2115–2120, 2006.

[17] David R Smith, Willie J Padilla, DC Vier, Syrus C Nemat-Nasser, and Seldon Schultz. Composite medium with simultaneously negative permeability and permittivity. *Physical Review Letters*, 84(18):4184, 2000.

[18] Wenshan Cai and Vladimir M Shalaev. *Optical metamaterials*, volume 10. Springer, 2010.

[19] Aleksandr Vaskin, Radoslaw Kolkowski, A Femius Koenderink, and Isabelle Staude. Light-emitting metasurfaces. *Nanophotonics*, 8(7):1151–1198, 2019.

[20] Nanfang Yu and Federico Capasso. Flat optics with designer metasurfaces. *Nature Materials*, 13(2):139–150, 2014.

[21] Jason Valentine, Shuang Zhang, Thomas Zentgraf, Erick Ulin-Avila, Dentcho A Genov, Guy Bartal, and Xiang Zhang. Three-dimensional optical metamaterial with a negative refractive index. *Nature*, 455(7211):376–379, 2008.

[22] Weisheng Yue, Yang Yang, Zhihong Wang, Longqing Chen, and Xianbin Wang. Gold split-ring resonators (SRRs) as substrates for surface-enhanced Raman scattering. *The Journal of Physical Chemistry C*, 117(42):21908–21915, 2013.

[23] Na Liu, Martin Mesch, Thomas Weiss, Mario Hentschel, and Harald Giessen. Infrared perfect absorber and its application as plasmonic sensor. *Nano Letters*, 10(7):2342–2348, 2010.

[24] Srujan K Dondapati, Tapan K Sau, Calin Hrelescu, Thomas A Klar, Fernando D Stefani, and Jochen Feldmann. Label-free biosensing based on single gold nanostars as plasmonic transducers. *ACS Nano*, 4(11):6318–6322, 2010.

[25] Feng Hao, Colleen L Nehl, Jason H Hafner, and Peter Nordlander. Plasmon resonances of a gold nanostar. *Nano Letters*, 7(3):729–732, 2007.

[26] Enzhou Liu, Lulu Qi, Juanjuan Bian, Yihan Chen, Xiaoyun Hu, Jun Fan, Hanchen Liu, Changjun Zhu, and Qiuping Wang. A facile strategy to fabricate plasmonic Cu modified TiO_2 nano-flower films for photocatalytic reduction of CO_2 to methanol. *Materials Research Bulletin*, 68:203–209, 2015.

[27] Wayne Dickson, Gregory A Wurtz, Paul Evans, Daniel O'Connor, Ron Atkinson, Robert Pollard, and Anatoly V Zayats. Dielectric-loaded plasmonic nanoantenna arrays: a metamaterial with tuneable optical properties. *Physical Review B*, 76(11):115411, 2007.

[28] Andrei V Kabashin, Paul Evans, Santa Pastkovsky, William Hendren, Gregory A Wurtz, Ron Atkinson, Robert Pollard, Viktor A Podolskiy, and Anatoly V Zayats. Plasmonic nanorod metamaterials for biosensing. *Nature Materials*, 8(11):867–871, 2009.

[29] Mazhar E Nasir, Wayne Dickson, Gregory A Wurtz, William P Wardley, and Anatoly V Zayats. Hydrogen detected by the naked eye: optical hydrogen gas sensors based on core/shell plasmonic nanorod metamaterials. *Advanced Materials*, 26(21):3532–3537, 2014.

[30] Hong Zhou, Dongxiao Li, Xindan Hui, and Xiaojing Mu. Infrared metamaterial for surface-enhanced infrared absorption spectroscopy: pushing the frontier of ultrasensitive on-chip sensing. *International Journal of Optomechatronics*, 15(1):97–119, 2021.

[31] Frank Neubrech, Christian Huck, Ksenia Weber, Annemarie Pucci, and Harald Giessen. Surface-enhanced infrared spectroscopy using resonant nanoantennas. *Chemical Reviews*, 117(7):5110–5145, 2017.

[32] Lisa V Brown, Xiao Yang, Ke Zhao, Bob Y Zheng, Peter Nordlander, and Naomi J Halas. Fan-shaped gold nanoantennas above reflective substrates for surface-enhanced infrared absorption (SEIRA). *Nano Letters*, 15(2):1272–1280, 2015.

[33] N I Landy, S Sajuyigbe, Jack J Mock, David R Smith, and Willie J Padilla. Perfect metamaterial absorber. *Physical Review Letters*, 100(20):207402, 2008.

[34] Andreas Tittl, Patrick Mai, Richard Taubert, Daniel Dregely, Na Liu, and Harald Giessen. Palladium-based plasmonic perfect absorber in the visible wavelength range and its application to hydrogen sensing. *Nano Letters*, 11(10):4366–4369, 2011.

[35] Joshua Hendrickson, Junpeng Guo, Boyang Zhang, Walter Buchwald, and Richard Soref. Wideband perfect light absorber at midwave infrared using multiplexed metal structures. *Optics letters*, 37(3):371–373, 2012.

[36] Kai Chen, Ronen Adato, and Hatice Altug. Dual-band perfect absorber for multispectral plasmon-enhanced infrared spectroscopy. *ACS Nano*, 6(9):7998–8006, 2012.

[37] Jianxiong Li, Shuqi Chen, Haifang Yang, Junjie Li, Ping Yu, Hua Cheng, Changzhi Gu, Hou-Tong Chen, and Jianguo Tian. Simultaneous control of light polarization and phase distributions using plasmonic metasurfaces. *Advanced Functional Materials*, 25(5):704–710, 2015.

[38] Nicholas Fang, Hyesog Lee, Cheng Sun, and Xiang Zhang. Sub-diffraction-limited optical imaging with a silver superlens. *Science*, 308(5721):534–537, 2005.

[39] Pan Wang, Alexey V Krasavin, Lufang Liu, Yunlu Jiang, Zhiyong Li, Xin Guo, Limin Tong, and Anatoly V Zayats. Molecular plasmonics with metamaterials. *Chemical Reviews*, 122(19):15031–15081, 2022.

[40] Justin Elser, Robyn Wangberg, Viktor A Podolskiy, and Evgenii E Narimanov. Nanowire metamaterials with extreme optical anisotropy. *Applied physics letters*, 89(26):261102, 2006.

[41] Brian M Wells, Anatoly V Zayats, and Viktor A Podolskiy. Nonlocal optics of plasmonic nanowire metamaterials. *Physical Review B*, 89(3):035111, 2014.

[42] Vladimir M Agranovich and Vladimir E Kravtsov. Notes on crystal optics of superlattices. *Solid State Communications*, 55(1):85–90, 1985.

[43] Sanong Ekgasit, Chuchaat Thammacharoen, and Wolfgang Knoll. Surface plasmon resonance spectroscopy based on evanescent field treatment. *Analytical chemistry*, 76(3):561–568, 2004.

[44] Alexander Poddubny, Ivan Iorsh, Pavel Belov, and Yuri Kivshar. Hyperbolic metamaterials. *Nature Photonics*, 7(12):948–957, 2013.

[45] Robert J Pollard, Antony Murphy, WR Hendren, Paul Evans, Ron Atkinson, Gregory A Wurtz, Anatoly V Zayats, and Viktor A Podolskiy. Optical nonlocalities and additional waves in epsilon-near-zero metamaterials. *Physical Review Letters*, 102(12):127405, 2009.

[46] Pavel Ginzburg, Diane J Roth, Mazhar E Nasir, Paulina Segovia, Alexey V Krasavin, James Levitt, Liisa M Hirvonen, Brian Wells, Klaus Suhling, David Richards, Viktor A Podolskiy, and Anatoly V Zayats. Spontaneous emission in non-local materials. *Light: Science & Applications*, 6(6):e16273–e16273, 2017.

[47] Ling Li, Wei Wang, Ting S Luk, Xiaodong Yang, and Jie Gao. Enhanced quantum dot spontaneous emission with multilayer metamaterial nanostructures. *ACS photonics*, 4(3):501–508, 2017.

[48] Maxim A Gorlach and Mikhail Lapine. Boundary conditions for the effective-medium description of subwavelength multilayered structures. *Physical Review B*, 101(7):075127, 2020.

[49] Alexey V Krasavin. A brief review on optical properties of planar metallic interfaces and films: from classical view to quantum description. *Journal of Physics: Photonics*, 3(4), 2021.

[50] Nanfang Yu, Patrice Genevet, Mikhail A Kats, Francesco Aieta, Jean-Philippe Tetienne, Federico Capasso, and Zeno Gaburro. Light propagation with phase discontinuities: generalized laws of reflection and refraction. *Science*, 334(6054):333–337, 2011.

[51] Na Liu, Hongcang Guo, Liwei Fu, Stefan Kaiser, Heinz Schweizer, and Harald Giessen. Three-dimensional photonic metamaterials at optical frequencies. *Nature Materials*, 7(1):31–37, 2008.

[52] Na Liu, Hui Liu, Shining Zhu, and Harald Giessen. Stereometamaterials. *Nature Photonics*, 3(3):157–162, 2009.

[53] Seungchul Kim, Jonghan Jin, Young-Jin Kim, In-Yong Park, Yunseok Kim, and Seung-Woo Kim. High-harmonic generation by resonant plasmon field enhancement. *Nature*, 453(7196):757–760, 2008.

[54] Byron D Gates, Qiaobing Xu, Michael Stewart, Declan Ryan, C Grant Willson, and George M Whitesides. New approaches to nanofabrication: molding, printing, and other techniques. *Chemical Reviews*, 105(4):1171–1196, 2005.

[55] Simon Dickreuter, Julia Gleixner, Andreas Kolloch, Johannes Boneberg, Elke Scheer, and Paul Leiderer. Mapping of plasmonic resonances in nanotriangles. *Beilstein journal of nanotechnology*, 4(1):588–602, 2013.

[56] Bin Ai, Ye Yu, Helmuth Möhwald, Limin Wang, and Gang Zhang. Resonant optical transmission through topologically continuous films. *ACS Nano*, 8(2):1566–1575, 2014.

[57] Guang Yang and Daniel T Hallinan. Gold nanoparticle monolayers from sequential interfacial ligand exchange and migration in a three-phase system. *Scientific Reports*, 6(1):1–17, 2016.

[58] Matthew J Rozin, David A Rosen, Tyler J Dill, and Andrea R Tao. Colloidal metasurfaces displaying near-ideal and tunable light absorbance in the infrared. *Nature Communications*, 6(1):1–7, 2015.

[59] Andrea Tao, Prasert Sinsermsuksakul, and Peidong Yang. Tunable plasmonic lattices of silver nanocrystals. *Nature Nanotechnology*, 2(7):435–440, 2007.

[60] Bin Ai and Yiping Zhao. Glancing angle deposition meets colloidal lithography: a new evolution in the design of nanostructures. *Nanophotonics*, 8(1):1–26, 2019.

[61] Si Hoon Lee, Kyle C Bantz, Nathan C Lindquist, Sang-Hyun Oh, and Christy L Haynes. Self-assembled plasmonic nanohole arrays. *Langmuir*, 25(23):13685–13693, 2009.

[62] Fedja J Wendisch, Richard Oberreiter, Miralem Salihovic, Michael S Elsaesser, and Gilles R Bourret. Confined Etching within 2D and 3D Colloidal Crystals for Tunable Nanostructured Templates: Local Environment Matters. *ACS Applied Materials & Interfaces*, 9(4):3931–3939, 2017.

[63] Joseph G Gordon and S Ernst. Surface plasmons as a probe of the electrochemical interface. *Surface Science*, 101(1-3):499–506, 1980.

[64] Claes Nylander, Bo Liedberg, and Tommy Lind. Gas detection by means of surface plasmon resonance. *Sensors and Actuators*, 3:79–88, 1982.

[65] Jiří Homola. Surface plasmon resonance sensors for detection of chemical and biological species. *Chemical Reviews*, 108(2):462–493, 2008.

[66] Briliant Adhi Prabowo, Agnes Purwidyantri, and Kou-Chen Liu. Surface plasmon resonance optical sensor: A review on light source technology. *Biosensors*, 8(3):80, 2018.

[67] Jeffrey N Anker, W Paige Hall, Olga Lyandres, Nilam C Shah, Jing Zhao, and Richard P Van Duyne. Biosensing with plasmonic nanosensors. *Nature Materials*, 7(6):442–453, 2008.

[68] Huanjun Chen, Lei Shao, Kat Choi Woo, Tian Ming, Hai-Qing Lin, and Jianfang Wang. Shape-dependent refractive index sensitivities of gold nanocrystals with the same plasmon resonance wavelength. *The Journal of Physical Chemistry C*, 113(41):17691–17697, 2009.

[69] Jinghua Fang, Igor Levchenko, Wei Yan, Igor Aharonovich, Morteza Aramesh, Steven Prawer, and Kostya Ostrikov. Plasmonic metamaterial sensor with ultra-high sensitivity in the visible spectral range. *Advanced Optical Materials*, 3(6):750–755, 2015.

[70] Etsuo Maeda, Sho Mikuriya, Koichi Endo, Ichiro Yamada, Atsushi Suda, and Jean-Jacques Delaunay. Optical hydrogen detection with periodic subwavelength palladium hole arrays. *Applied Physics Letters*, 95(13):133504, 2009.

[71] Pin Chieh Wu, Chun Yen Liao, Jia-Wern Chen, and Din Ping Tsai. Isotropic absorption and sensor of vertical split-ring resonator. *Advanced Optical Materials*, 5(2):1600581, 2017.

[72] Wei Wang, Fengping Yan, Siyu Tan, Hong Zhou, and Yafei Hou. Ultrasensitive terahertz metamaterial sensor based on vertical split ring resonators. *Photonics Research*, 5(6):571–577, 2017.

[73] Nikos Vasilantonakis, Gregory A Wurtz, Viktor A Podolskiy, and Anatoly V Zayats. Refractive index sensing with hyperbolic metamaterials: strategies for biosensing and nonlinearity enhancement. *Optics Express*, 23(11):14329–14343, 2015.

[74] Kandammathe Valiyaveedu Sreekanth, Yunus Alapan, Mohamed ElKabbash, Efe Ilker, Michael Hinczewski, Umut A Gurkan, Antonio De Luca, and Giuseppe Strangi. Extreme sensitivity biosensing platform based on hyperbolic metamaterials. *Nature Materials*, 15(6):621–627, 2016.

[75] Kandammathe Valiyaveedu Sreekanth, Yunus Alapan, Mohamed ElKabbash, Amy M Wen, Efe Ilker, Michael Hinczewski, Umut A Gurkan, Nicole F Steinmetz, and Giuseppe Strangi. Enhancing the angular sensitivity of plasmonic sensors using hyperbolic metamaterials. *Advanced Optical Materials*, 4(11):1767–1772, 2016.

[76] Li Jiang, Shuwen Zeng, Zhengji Xu, Qingling Ouyang, Dao-Hua Zhang, Peter Han Joo Chong, Philippe Coquet, Sailing He, and Ken-Tye Yong. Multifunctional hyperbolic nanogroove metasurface for submolecular detection. *Small*, 13(30):1700600, 2017.

[77] Ruoqin Yan, Tao Wang, Xinzhao Yue, Huimin Wang, Yu-Hui Zhang, Peng Xu, Lu Wang, Yuandong Wang, and Jinyan Zhang. Highly sensitive plasmonic nanorod hyperbolic metamaterial biosensor. *Photonics Research*, 10(1):84–95, 2022.

[78] John McPhillips, Antony Murphy, Magnus P Jonsson, William R Hendren, Ronald Atkinson, Fredrik Hook, Anatoly V Zayats, and Robert J Pollard. High-performance biosensing using arrays of plasmonic nanotubes. *ACS Nano*, 4(4):2210–2216, 2010.

[79] Antony Murphy, Yannick Sonnefraud, Alexey V Krasavin, Pavel Ginzburg, Frances Morgan, John McPhillips, Gregory A Wurtz, Stefan A Maier, Anatoly V Zayats, and Robert Pollard. Fabrication and optical properties of large-scale arrays of gold nanocavities based on rod-in-a-tube coaxials. *Applied Physics Letters*, 102(10):103103, 2013.

[80] Pan Wang, Alexey V Krasavin, Francesco N Viscomi, Ali M Adawi, Jean-Sebastien G Bouillard, Lei Zhang, Diane J Roth, Limin Tong, and Anatoly V Zayats. Metaparticles: Dressing nano-objects with a hyperbolic coating. *Laser & Photonics Reviews*, 12(11):1800179, 2018.

[81] Arif E Cetin and Hatice Altug. Fano resonant ring/disk plasmonic nanocavities on conducting substrates for advanced biosensing. *ACS Nano*, 6(11):9989–9995, 2012.

[82] Marcus Matuschek, Dhruv Pratap Singh, Hyeon-Ho Jeong, Maxim Nesterov, Thomas Weiss, Peer Fischer, Frank Neubrech, and Na Liu. Chiral plasmonic hydrogen sensors. *Small*, 14(7):1702990, 2018.

[83] Andreas Tittl, Harald Giessen, and Na Liu. Plasmonic gas and chemical sensing. *Nanophotonics*, 3(3):157–180, 2014.

[84] Alexander W Powell, David M Coles, Robert A Taylor, Andrew AR Watt, Hazel E Assender, and Jason M Smith. Plasmonic gas sensing using nanocube patch antennas. *Advanced Optical Materials*, 4(4):634–642, 2016.

[85] Ankun Yang, Mark D Huntington, M Fernanda Cardinal, Sicelo S Masango, Richard P Van Duyne, and Teri W Odom. Hetero-oligomer nanoparticle arrays for plasmon-enhanced hydrogen sensing. *ACS Nano*, 8(8):7639–7647, 2014.

[86] Takaaki Beni, Naoki Yamasaku, Takuma Kurotsu, Naoki To, Shinji Okazaki, Taro Arakawa, Armandas Balčytis, Gediminas Seniutinas, Saulius Juodkazis, and Yoshiaki Nishijima. Metamaterial for hydrogen sensing. *ACS Sensors*, 4(9):2389–2394, 2019.

[87] Florian Sterl, Nikolai Strohfeldt, Steffen Both, Ediz Herkert, Thomas Weiss, and Harald Giessen. Design principles for sensitivity optimization in plasmonic hydrogen sensors. *ACS Sensors*, 5(4):917–927, 2020.

[88] Pedro Rocha-Rodrigues, Aurelio Hierro-Rodriguez, Ariel Guerreiro, Pedro Jorge, José Luís Santos, Joao Pedro Araujo, and José Miguel Teixeira. Hydrogen optical metamaterial sensor based on Pd dendritic nanostructures. *ChemistrySelect*, 1(13):3854–3860, 2016.

[89] Hoang Mai Luong, Minh Thien Pham, Tyler Guin, Richa Pokharel Madhogaria, Manh-Huong Phan, George Keefe Larsen, and Tho Duc Nguyen. Sub-second and ppm-level optical sensing of hydrogen using templated control of nano-hydride geometry and composition. *Nature Communications*, 12(1):1–10, 2021.

[90] Ferry Anggoro Ardy Nugroho, Robin Eklund, Sara Nilsson, and Christoph Langhammer. A fiber-optic nanoplasmonic hydrogen sensor via pattern-transfer of nanofabricated PdAu alloy nanostructures. *Nanoscale*, 10(44):20533–20539, 2018.

[91] Ferry A A Nugroho, Iwan Darmadi, Lucy Cusinato, Arturo Susarrey-Arce, Herman Schreuders, Lars J Bannenberg, Alice Bastos da Silva Fanta, Shima Kadkhodazadeh, Jakob B Wagner, Tomasz J Antosiewicz, Anders Hellman, Vladimir P Zhdanov, Bernard Dam, and Christoph Langhammer. Metal–polymer hybrid nanomaterials for plasmonic ultrafast hydrogen detection. *Nature Materials*, 18(5):489–495, 2019.

[92] Chun-Ya Chiu and Michael H Huang. Polyhedral Au-Pd core–shell nanocrystals as highly spectrally responsive and reusable hydrogen sensors in aqueous solution. *Angewandte Chemie*, 125(48):12941–12945, 2013.

[93] Hongxing Xu, Erik J Bjerneld, Mikael Käll, and Lars Börjesson. Spectroscopy of single hemoglobin molecules by surface enhanced Raman scattering. *Physical Review Letters*, 83(21):4357, 1999.

[94] Shuming Nie and Steven R Emory. Probing single molecules and single nanoparticles by surface-enhanced Raman scattering. *Science*, 275(5303):1102–1106, 1997.

[95] Dong-Kwon Lim, Ki-Seok Jeon, Hyung Min Kim, Jwa-Min Nam, and Yung Doug Suh. Nanogap-engineerable Raman-active nanodumbbells for single-molecule detection. *Nature Materials*, 9(1):60–67, 2010.

[96] Kang Yang, Jingyu Wang, Xu Yao, Danya Lyu, Jinfeng Zhu, Zhilin Yang, Bowen Liu, and Bin Ren. Large-area plasmonic metamaterial with thickness-dependent absorption. *Advanced Optical Materials*, 9(1):2001375, 2021.

[97] Yingli Wang, Chen Zhao, Jingjing Wang, Xuan Luo, Lijuan Xie, Shijie Zhan, Jongmin Kim, Xiaozhi Wang, Xiangjiang Liu, and Yibin Ying. Wearable plasmonic-metasurface sensor for noninvasive and universal molecular fingerprint detection on biointerfaces. *Science Advances*, 7(4):eabe4553, 2021.

[98] James V Coe, Kenneth R Rodriguez, Shannon Teeters-Kennedy, Katherine Cilwa, Joseph Heer, Hong Tian, and Shaun M Williams. Metal films with arrays of tiny holes: spectroscopy with infrared plasmonic scaffolding. *The Journal of Physical Chemistry C*, 111(47):17459–17472, 2007.

[99] Inyong Hwang, Jaeyeon Yu, Jihye Lee, Jun-Hyuk Choi, Dae-Geun Choi, Sohee Jeon, Jongwon Lee, and Joo-Yun Jung. Plasmon-enhanced infrared spectroscopy based on metamaterial absorbers with dielectric nanopedestals. *Acs Photonics*, 5(9):3492–3498, 2018.

[100] Ertugrul Cubukcu, Shuang Zhang, Yong-Shik Park, Guy Bartal, and Xiang Zhang. Split ring resonator sensors for infrared detection of single molecular monolayers. *Applied Physics Letters*, 95(4):043113, 2009.

[101] Imogen M Pryce, Yousif A Kelaita, Koray Aydin, and Harry A Atwater. Compliant metamaterials for resonantly enhanced infrared absorption spectroscopy and refractive index sensing. *ACS Nano*, 5(10):8167–8174, 2011.

[102] In-Ho Lee, Daehan Yoo, Phaedon Avouris, Tony Low, and Sang-Hyun Oh. Graphene acoustic plasmon resonator for ultrasensitive infrared spectroscopy. *Nature Nanotechnology*, 14(4):313–319, 2019.

[103] Leonetta Baldassarre, Emilie Sakat, Jacopo Frigerio, Antonio Samarelli, Kevin Gallacher, Eugenio Calandrini, Giovanni Isella, Douglas J Paul, Michele Ortolani, and Paolo Biagioni. Midinfrared plasmon-enhanced spectroscopy with germanium antennas on silicon substrates. *Nano Letters*, 15(11):7225–7231, 2015.

[104] Martina Abb, Yudong Wang, Nikitas Papasimakis, CH De Groot, and Otto L Muskens. Surface-enhanced infrared spectroscopy using metal oxide plasmonic antenna arrays. *Nano Letters*, 14(1):346–352, 2014.

[105] Joseph R Lakowicz. Radiative decay engineering 5: metal-enhanced fluorescence and plasmon emission. *Analytical biochemistry*, 337(2):171–194, 2005.

[106] Daniel Darvill, Anthony Centeno, and Fang Xie. Plasmonic fluorescence enhancement by metal nanostructures: shaping the future of bionanotechnology. *Physical Chemistry Chemical Physics*, 15(38):15709–15726, 2013.

[107] Rizia Bardhan, Nathaniel K Grady, Joseph R Cole, Amit Joshi, and Naomi J Halas. Fluorescence enhancement by Au nanostructures: nanoshells and nanorods. *ACS Nano*, 3(3):744–752, 2009.

[108] Ragip A Pala, Serkan Butun, Koray Aydin, and Harry A Atwater. Omnidirectional and broadband absorption enhancement from trapezoidal Mie resonators in semiconductor metasurfaces. *Scientific Reports*, 6(1):1–7, 2016.

[109] Koray Aydin, Vivian E Ferry, Ryan M Briggs, and Harry A Atwater. Broadband polarization-independent resonant light absorption using ultrathin plasmonic super absorbers. *Nature Communications*, 2(1):1–7, 2011.

[110] Theresa Bartschmid, Fedja J Wendisch, Amin Farhadi, and Gilles R Bourret. Recent advances in structuring and patterning silicon nanowire arrays for engineering light absorption in three dimensions. *ACS Applied Energy Materials*, 2021.

[111] Syed Mubeen, Joun Lee, Nirala Singh, Stephan Krämer, Galen D Stucky, and Martin Moskovits. An autonomous photosynthetic device in which all charge carriers derive from surface plasmons. *Nature Nanotechnology*, 8(4):247–251, 2013.

[112] Jiangtian Li, Scott K Cushing, Peng Zheng, Fanke Meng, Deryn Chu, and Nianqiang Wu. Plasmon-induced photonic and energy-transfer enhancement of solar water splitting by a hematite nanorod array. *Nature Communications*, 4(1):1–8, 2013.

[113] Jiangtian Li, Scott K Cushing, Peng Zheng, Tess Senty, Fanke Meng, Alan D Bristow, Ayyakkannu Manivannan, and Nianqiang Wu. Solar hydrogen generation by a CdS-Au-TiO_2 sandwich nanorod array enhanced with Au nanoparticle as electron relay and plasmonic photosensitizer. *Journal of the American Chemical Society*, 136(23):8438–8449, 2014.

[114] T Gamze Ulusoy Ghobadi, Amir Ghobadi, Oguz Odabasi, Ferdi Karadas, and Ekmel Ozbay. Subwavelength densely packed disordered semiconductor metasurface units for photoelectrochemical hydrogen generation. *ACS Applied Energy Materials*, 5(3):2826–2837, 2022.

[115] Xu Shi, Kosei Ueno, Tomoya Oshikiri, Quan Sun, Keiji Sasaki, and Hiroaki Misawa. Enhanced water splitting under modal strong coupling conditions. *Nature Nanotechnology*, 13(10):953–958, 2018.

[116] Hanwei Gao, Chong Liu, Hoon Eui Jeong, and Peidong Yang. Plasmon-enhanced photocatalytic activity of iron oxide on gold nanopillars. *ACS Nano*, 6(1):234–240, 2012.

[117] Dominic Bosomtwi, Marek Osiński, and Viktoriia E Babicheva. Lattice effect for enhanced hot-electron generation in nanoelectrodes. *Optical Materials Express*, 11(9):3232–3244, 2021.

[118] Qi Xiao, Timothy U Connell, Jasper J Cadusch, Ann Roberts, Anthony SR Chesman, and Daniel E Gomez. Hot-carrier organic synthesis via the near-perfect absorption of light. *ACS Catalysis*, 8(11):10331–10339, 2018.

[119] Jorge U Salmón-Gamboa, Mayela Romero-Gómez, Diane J Roth, Alexey V Krasavin, Pan Wang, Wayne Dickson, and Anatoly V Zayats. Rational design of bimetallic photocatalysts based on plasmonically-derived hot carriers. *Nanoscale Advances*, 3(3):767–780, 2021.

[120] Phillip Christopher, Hongliang Xin, and Suljo Linic. Visible-light-enhanced catalytic oxidation reactions on plasmonic silver nanostructures. *Nature Chemistry*, 3(6):467–472, 2011.

[121] Simone Ezendam, Matias Herran, Lin Nan, Christoph Gruber, Yicui Kang, Franz Gröbmeyer, Rui Lin, Julian Gargiulo, Ana Sousa-Castillo, and Emiliano Cortés. Hybrid plasmonic nanomaterials for hydrogen generation and carbon dioxide reduction. *ACS Energy Letters*, 7(2):778–815, 2022.

[122] Joel YY Loh, Mahdi Safari, Chengliang Mao, Camilo J Viasus, George V Eleftheriades, Geoffrey A Ozin, and Nazir P Kherani. Near-perfect absorbing copper metamaterial for solar fuel generation. *Nano Letters*, 21(21):9124–9130, 2021.

[123] Peng Xu, Weiwei Lu, Jinjin Zhang, and Li Zhang. Efficient hydrolysis of ammonia borane for hydrogen evolution catalyzed by plasmonic Ag@Pd core–shell nanocubes. *ACS Sustainable Chemistry & Engineering*, 8(33):12366–12377, 2020.

[124] Fengxia Tong, Zaizhu Lou, Xizhuang Liang, Fahao Ma, Weijie Chen, Zeyan Wang, Yuanyuan Liu, Peng Wang, Hefeng Cheng, Ying Dai, et al. Plasmon-induced dehydrogenation of formic acid on Pd-dotted Ag@Au hexagonal nanoplates and single-particle study. *Applied Catalysis B: Environmental*, 277:119226, 2020.

[125] Pan Wang, Alexey V. Krasavin, Mazhar E. Nasir, Wayne Dickson, and Anatoly V. Zayats. Reactive tunnel junctions in electrically driven plasmonic nanorod metamaterials. *Nature Nanotechnology*, 13(2):159–164, 2018.

[126] Gregory A Wurtz, Robert Pollard, Willam Hendren, GP Wiederrecht, DJ Gosztola, VA Podolskiy, and Anatoly V Zayats. Designed ultrafast optical nonlinearity in a plasmonic nanorod metamaterial enhanced by nonlocality. *Nature Nanotechnology*, 6(2):107–111, 2011.

[127] Andres D Neira, Nicolas Olivier, Mazhar E Nasir, Wayne Dickson, Gregory A Wurtz, and Anatoly V Zayats. Eliminating material constraints for nonlinearity with plasmonic metamaterials. *Nature Communications*, 6(1):1–8, 2015.

[128] Luke H Nicholls, Francisco J Rodríguez-Fortuño, Mazhar E Nasir, R Margoth Córdova-Castro, Nicolas Olivier, Gregory A Wurtz, and Anatoly V Zayats. Ultrafast synthesis and switching of light polarization in nonlinear anisotropic metamaterials. *Nature Photonics*, 11(10):628–633, 2017.

[129] Gregory A Wurtz, Wayne Dickson, Daniel O'Connor, Ron Atkinson, William Hendren, Paul Evans, Robert Pollard, and Anatoly V Zayats. Guided plasmonic modes in nanorod assemblies: strong electromagnetic coupling regime. *Optics Express*, 16(10):7460–7470, 2008.

[130] Diane J Roth, Alexey V Krasavin, Alexander Wade, Wayne Dickson, Antony Murphy, Stéphane Kéna-Cohen, Robert Pollard, Gregory A Wurtz, David Richards, Stefan A Maier, and Anatoly V Zayats. Spontaneous emission inside a hyperbolic metamaterial waveguide. *ACS Photonics*, 4(10):2513–2521, 2017.

[131] Sabu Thomas, Nandakumar Kalarikkal, and Ann Rose Abraham. *Design, fabrication and characterization of multifunctional nanomaterials*. Elsevier, 2022.

[132] Kirt R Williams, Kishan Gupta, and Matthew L Wasilik. Etch rates for micromachining processing-part II. *Journal of Microelectromechanical Systems*, 12(6):761–778, 2003.

[133] Ron Atkinson, William R. Hendren, Gregory A. Wurtz, Wayne Dickson, Anatoly V. Zayats, Paul Evans, and Robert J. Pollard. Anisotropic optical properties of arrays of gold nanorods embedded in alumina. *Physical Review B*, 73:235402, 2006.

[134] Yunlu Jiang, Alexey V Krasavin, Mazhar E Nasir, Pan Wang, and Anatoly V Zayats. Humidity-induced direct modification of the optical response of plasmonic nanorod metamaterials. *Optical Materials Express*, 12(12):4574–4581, 2022.

[135] Gerd Binnig, Calvin F Quate, and Ch Gerber. Atomic force microscope. *Physical Review Letters*, 56(9):930, 1986.

[136] Chanmin Su, Jian Shi, Yan Hu, Shuqing Hu, and Ji Ma. Method and apparatus of using peak force tapping mode to measure physical properties of a sample, 2018.

[137] Junkal Gutierrez, Iñaki Mondragon, and Agnieszka Tercjak. Quantitative nanoelectrical and nanomechanical properties of nanostructured hybrid composites by peakforce tunneling atomic force microscopy. *The Journal of Physical Chemistry C*, 118(2):1206–1212, 2014.

[138] Bert Voigtländer. *Atomic force microscopy*. Springer, 2019.

[139] Ke Xu, Weihang Sun, Yongjian Shao, Fanan Wei, Xiaoxian Zhang, Wei Wang, and Peng Li. Recent development of peakforce tapping mode atomic force microscopy and its applications on nanoscience. *Nanotechnology Reviews*, 7(6):605–621, 2018.

[140] E. Papis-Polakowska, B. Radkowski, S. Lesko, and J. Kaniewski. Peakforce tapping technique for characterization of thin organic passivating layers. *Acta Physica Polonica A*, 125(4):1056–1060, 2014.

[141] Jeroen Drijkoningen, Jurgen Kesters, Tim Vangerven, Emilie Bourgeois, Laurence Lutsen, Dirk Vanderzande, Wouter Maes, Jan D'Haen, and Jean Manca. Investigating the role of efficiency enhancing interlayers for bulk heterojunction solar cells by scanning probe microscopy. *Organic Electronics*, 15(6):1282–1289, 2014.

[142] P. B. Johnson and R. W. Christy. Optical constants of the noble metals. *Physical Review B*, 6:4370–4379, 1972.

[143] Luis V. Rodríguez de Marcos, Juan I. Larruquert, José A. Méndez, and José A. Aznárez. Self-consistent optical constants of SiO_2 and Ta_2O_5 films. *Optical Materials Express*, 6(11):3622–3637, 2016.

[144] I. H. Malitson. Interspecimen comparison of the refractive index of fused silica. *Journal of the Optical Society of America*, 55(10):1205–1209, 1965.

[145] PH Lissberger and RG Nelson. Optical properties of thin film Au-MgF_2 cermets. *Thin Solid Films*, 21(1):159–172, 1974.

[146] Thu HH Le, Akihiro Morita, and Takuo Tanaka. Refractive index of nanoconfined water reveals its anomalous physical properties. *Nanoscale Horizons*, 5(6):1016–1024, 2020.

[147] Maysoun Douas, Manuel I Marqués, and Pedro A Serena. Identification of water content in nanocavities. *Nanoscale Research Letters*, 8(1):1–4, 2013.

[148] T. J. Yen, W. J. Padilla, N. Fang, D. C. Vier, D. R. Smith, J. B. Pendry, D. N. Basov, and X. Zhang. Terahertz magnetic response from artificial materials. *Science*, 303(5663):1494–1496, 2004.

[149] V. M. Agranovich, Ron Shen, Ray H Baughman, and Anvar A Zakhidov. Linear and nonlinear wave propagation in negative refraction metamaterials. *Physical Review B*, 69:165112, 2004.

[150] Jie Yao, Zhaowei Liu, Yongmin Liu, Yuan Wang, Cheng Sun, Guy Bartal, Angelica M. Stacy, and Xiang Zhang. Optical negative refraction in bulk metamaterials of nanowires. *Science*, 321(5891):930–930, 2008.

[151] Alessandro Salandrino and Nader Engheta. Far-field subdiffraction optical microscopy using metamaterial crystals: Theory and simulations. *Physical Review B*, 74:075103, 2006.

[152] Zubin Jacob, Leonid V. Alekseyev, and Evgenii Narimanov. Optical hyperlens: Far-field imaging beyond the diffraction limit. *Optics Express*, 14(18):8247–8256, 2006.

[153] Yun Lai, Huanyang Chen, Zhao-Qing Zhang, and C. T. Chan. Complementary media invisibility cloak that cloaks objects at a distance outside the cloaking shell. *Physical Review Letters*, 102:093901, 2009.

[154] Wenshan Cai, Uday K Chettiar, Alexander V Kildishev, and Vladimir M Shalaev. Optical cloaking with metamaterials. *Nature Photonics*, 1(4):224–227, 2007.

[155] Zelio Fusco, Mohsen Rahmani, Renheng Bo, Ruggero Verre, Nunzio Motta, Mikael Käll, Dragomir Neshev, and Antonio Tricoli. Nanostructured dielectric fractals on resonant plasmonic metasurfaces for selective and sensitive optical sensing of volatile compounds. *Advanced Materials*, 30(30):1800931, 2018.

[156] Martti Kauranen and Anatoly V Zayats. Nonlinear plasmonics. *Nature Photonics*, 6(11):737–748, 2012.

[157] Paulina Segovia, Giuseppe Marino, Alexey V. Krasavin, Nicolas Olivier, Gregory A. Wurtz, Pavel A. Belov, Pavel Ginzburg, and Anatoly V. Zayats. Hyperbolic metamaterial antenna for second-harmonic generation tomography. *Optics Express*, 23(24):30730–30738, 2015.

[158] Giuseppe Marino, Paulina Segovia, Alexey V. Krasavin, Pavel Ginzburg, Nicolas Olivier, Gregory A. Wurtz, and Anatoly V. Zayats. Second-harmonic generation from hyperbolic plasmonic nanorod metamaterial slab. *Laser & Photonics Reviews*, 12(2):1700189, 2018.

[159] Pavel Ginzburg, Diane J Roth, Mazhar E Nasir, Paulina Segovia, Alexey V Krasavin, James Levitt, Liisa M Hirvonen, Brian Wells, Klaus Suhling, David Richards, Viktor A Podolskiy, and Anatoly V Zayats. Spontaneous emission in non-local materials. *Light: Science & Applications*, 6(6):e16273–e16273, 2017.

[160] Rohith Chandrasekar, Zhuoxian Wang, Xiangeng Meng, Shaimaa I Azzam, Mikhail Y Shalaginov, Alexei Lagutchev, Young L Kim, Alexander Wei, Alexander V Kildishev, Alexandra Boltasseva, and Vladimir M Shalaev. Lasing action with gold nanorod hyperbolic metamaterials. *ACS Photonics*, 4(3):674–680, 2017.

[161] Zelio Fusco, Mohsen Rahmani, Thanh Tran-Phu, Chiara Ricci, Alexander Kiy, Patrick Kluth, Enrico Della Gaspera, Nunzio Motta, Dragomir Neshev, and Antonio Tricoli. Photonic fractal metamaterials: A metal–semiconductor platform with enhanced volatile-compound sensing performance. *Advanced Materials*, 32(50):2002471, 2020.

[162] Pavel Ginzburg, Alexey V. Krasavin, Alexander N. Poddubny, Pavel A. Belov, Yuri S. Kivshar, and Anatoly V. Zayats. Self-induced torque in hyperbolic metamaterials. *Physical Review Letters*, 111:036804, 2013.

[163] Alexey V. Krasavin, Pan Wang, Mazhar E. Nasir, Yunlu Jiang, and Anatoly V. Zayats. Tunneling-induced broadband and tunable optical emission from plasmonic nanorod metamaterials. *Nanophotonics*, 9(2):427–434, 2020.

[164] Pan Wang, Mazhar E Nasir, Alexey V Krasavin, Wayne Dickson, and Anatoly V Zayats. Optoelectronic synapses based on hot-electron-induced chemical processes. *Nano Letters*, 20(3):1536–1541, 2020.

[165] Ruoqin Yan, Tao Wang, Xinzhao Yue, Huimin Wang, Yu-Hui Zhang, Peng Xu, Lu Wang, Yuandong Wang, and Jinyan Zhang. Highly sensitive plasmonic nanorod hyperbolic metamaterial biosensor. *Photonics Research*, 10(1):84–95, 2022.

[166] Nikolaos Vasilantonakis, Mazhar E Nasir, Wayne Dickson, Gregory A Wurtz, and Anatoly V Zayats. Bulk plasmon-polaritons in hyperbolic nanorod metamaterial waveguides. *Laser & Photonics Reviews*, 9(3):345–353, 2015.

[167] Pan Wang, Mazhar E Nasir, Alexey V Krasavin, Wayne Dickson, Yunlu Jiang, and Anatoly V Zayats. Plasmonic metamaterials for nanochemistry and sensing. *Accounts of Chemical Research*, 52(11):3018–3028, 2019.

[168] Philip E Ciddor. Refractive index of air: new equations for the visible and near infrared. *Applied Optics*, 35(9):1566–1573, 1996.

[169] Hamid E Limodehi and François Légaré. Fiber optic humidity sensor using water vapor condensation. *Optics Express*, 25(13):15313–15321, 2017.

[170] Niharika Gupta, Hossain M Fahad, Matin Amani, Xiaohui Song, Mary Scott, and Ali Javey. Elimination of response to relative humidity changes in chemical-sensitive field-effect transistors. *ACS Sensors*, 4(7):1857–1863, 2019.

[171] Yuan Liu, Rui Cheng, Lei Liao, Hailong Zhou, Jingwei Bai, Gang Liu, Lixin Liu, Yu Huang, and Xiangfeng Duan. Plasmon resonance enhanced multicolour photodetection by graphene. *Nature Communications*, 2(1):579, 2011.

[172] K. T. Shimizu, W. K. Woo, B. R. Fisher, H. J. Eisler, and M. G. Bawendi. Surface-enhanced emission from single semiconductor nanocrystals. *Physical Review Letters*, 89:117401, 2002.

[173] D. M. Koller, A. Hohenau, H. Ditlbacher, N. Galler, F. Reil, F. R. Aussenegg, A. Leitner, E. J. W. List, and J. R. Krenn. Organic plasmon-emitting diode. *Nature Photonics*, 2(11):684–687, 2008.

[174] Wei Du, Tao Wang, Hong-Son Chu, and Christian A. Nijhuis. Highly efficient on-chip direct electronic-plasmonic transducers. *Nature Photonics*, 11(10):623–627, 2017.

[175] Palash Bharadwaj, Alexandre Bouhelier, and Lukas Novotny. Electrical excitation of surface plasmons. *Physical Review Letters*, 106:226802, 2011.

[176] John Lambe and S. L. McCarthy. Light emission from inelastic electron tunneling. *Physical Review Letters*, 37:923–925, 1976.

[177] Haoliang Qian, Su-Wen Hsu, Kargal Gurunatha, Conor T. Riley, Jie Zhao, Dylan Lu, Andrea R. Tao, and Zhaowei Liu. Efficient light generation from enhanced inelastic electron tunnelling. *Nature Photonics*, 12(8):485–488, 2018.

[178] Pengyu Fan, Carlo Colombo, Kevin C. Y. Huang, Peter Krogstrup, Jesper Nygård, Anna Fontcuberta i Morral, and Mark L. Brongersma. An electrically-driven GaAs nanowire surface plasmon source. *Nano Letters*, 12(9):4943–4947, 2012.

[179] Cheng Zhang, Jean-Paul Hugonin, Anne-Lise Coutrot, Christophe Sauvan, François Marquier, and Jean-Jacques Greffet. Antenna surface plasmon emission by inelastic tunneling. *Nature Communications*, 10(1):4949, 2019.

[180] Mazhar E Nasir, S. Peruch, Nikos Vasilantonakis, William P Wardley, Wayne Dickson, Gregory A Wurtz, and Anatoly V Zayats. Tuning the effective plasma frequency of nanorod metamaterials from visible to telecom wavelengths. *Applied Physics Letters*, 107(12):121110, 2015.

[181] John Lambe and SL McCarthy. Light emission from inelastic electron tunneling. *Physical Review Letters*, 37(14):923, 1976.

[182] Wei Du, Tao Wang, Hong-Son Chu, Lin Wu, Rongrong Liu, Song Sun, Wee Kee Phua, Lejia Wang, Nikodem Tomczak, and Christian A Nijhuis. On-chip molecular electronic plasmon sources based on self-assembled monolayer tunnel junctions. *Nature Photonics*, 10(4):274–280, 2016.

[183] Johannes Kern, René Kullock, Jord Prangsma, Monika Emmerling, Martin Kamp, and Bert Hecht. Electrically driven optical antennas. *Nature Photonics*, 9(9):582–586, 2015.

[184] Markus Parzefall, Palash Bharadwaj, Achint Jain, Takashi Taniguchi, Kenji Watanabe, and Lukas Novotny. Antenna-coupled photon emission from hexagonal boron nitride tunnel junctions. *Nature Nanotechnology*, 10(12):1058–1063, 2015.

[185] A Mansourian, H Saidpour, and SH Mannan. Conductive pattern, electrical and mechanical characterisation of gold nanorods inside porous alumina template. *Applied Surface Science*, 532:147426, 2020.

[186] John D. Cutnell and Kenneth W. Johnson. *Physics*. Wiley, 1998.

[187] Tomoyuki Morita and Stuart Lindsay. Determination of single molecule conductances of alkanedithiols by conducting-atomic force microscopy with large gold nanoparticles. *Journal of the American Chemical Society*, 129(23):7262–7263, 2007.

[188] Eric Le Moal, Sylvie Marguet, Benoît Rogez, Samik Mukherjee, Philippe Dos Santos, Elizabeth Boer-Duchemin, Geneviève Comtet, and Gérald Dujardin. An Electrically excited nanoscale light source with active angular control of the emitted light. *Nano Letters*, 13(9):4198–4205, 2013.

[189] Kelvin JA Ooi, Hong Son Chu, Chang Yu Hsieh, Dawn TH Tan, and Lay Kee Ang. Highly efficient midinfrared on-chip electrical generation of graphene plasmons by inelastic electron tunneling excitation. *Physical Review Applied*, 3(5):054001, 2015.

[190] Michael G Boyle, J Mitra, and P Dawson. Infrared emission from tunneling electrons: The end of the rainbow in scanning tunneling microscopy. *Applied Physics Letters*, 94(23):233118, 2009.